Towards the Development of an Explosives Detection System Using Neutron Resonance Radiography

by

Whitney Lyke Raas

B.S. Physics (2001)
University of California, Los Angeles

S.M. Political Science (2006)
Massachusetts Institute of Technology

Submitted to the Department of Nuclear Science and Engineering
in Partial Fulfillment of the Requirements for the Degree of
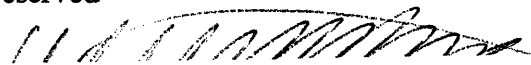Doctor of Philosophy in Nuclear Engineering

at the

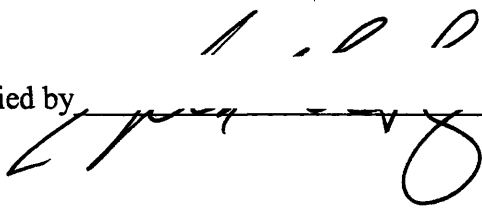Massachusetts Institute of Technology
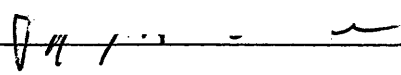October 2006
[February 2007]

Signature of Author_____

Department of Nuclear Science and Engineering
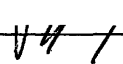October 27, 2006

Certified by_____

Richard Lanza
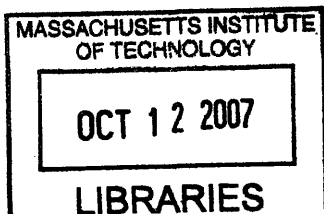Senior Research Scientist
Thesis Advisor

Certified by_____

Jeffrey Coderre
Associate Professor
Thesis Reader

Accepted by_____

Jeffrey Coderre
Chairman, Department Committee on Graduate Students

Towards the Development of an Explosives Detection System
Using Neutron Resonance Radiography
by
Whitney Lyke Raas

Submitted to the Department of Nuclear Science and Engineering
on October 27, 2006 in Partial Fulfillment of the
Requirements for the Degree of Doctor of Philosophy
in Nuclear Engineering

Abstract

Detection of conventional explosives remains a challenge to air security, as indicated by recent reports detailing lapses in security screening and new requirements that mandate screening 100% of checked luggage. Neutron Resonance Radiography (NRR) has been under investigation as a supplement to conventional x-ray systems as a non-invasive, non-destructive means of detecting explosive material in checked luggage. Using fast (1-6 MeV) neutrons produced by an accelerator-based $D(d,n)^3He$ reaction and a scintillator-coupled CCD camera, NRR provides both an imaging capability and the ability to determine the chemical composition of materials in baggage or cargo.

Theoretical studies and simulations have shown the potential of NRR. This thesis takes the first step towards experimental implementation using a deuterium target for multiple-element discrimination. A new neutron source has been developed to provide the high-flux neutron beam required for NRR while simultaneously minimizing gamma ray production. The gas target incorporates a 4 atm D_2 gas chamber, separated from the accelerator beamline with thin, 5 µm tungsten or 7 µm molybdenum foils supported by a honeycomb lattice structure to increase structural integrity and provide a heat removal pathway. An argon gas cooling system is incorporated to cool the target and thus increase the neutron flux. The gas target has been shown to withstand 3.0 MeV deuteron beam currents in excess of 35 µA for extended periods without failure, resulting in a neutron flux of 6.6×10^7 neutrons/sr/µA/s.

A neutron imaging system was designed to detect the fast neutrons and produce a digital image of objects for analysis. Two neutron detectors, Eljen plastic scintillator EJ-200 and a ZnS(Ag) scintillating screen were tested for their suitability to NRR. Although ZnS(Ag) has a lower detection efficiency, its resolution, minimal light dispersion, and insensitivity to gamma rays made it the more favorable material. An Apogee Instruments, Inc., Alta U9 CCD camera was used to record the light from the scintillator to create radiographs. The gas target and neutron detection system were used to evaluate the results of experimental work to determine the feasibility of NRR. These experiments ultimately indicated that although NRR has promise, significant challenges regarding neutron flux and image processing must be overcome before the technique can be implemented as an explosives detection system. Suggestions are made for improvements.

Thesis Supervisor: Richard Lanza
Title: Senior Research Scientist

Thesis Reader: Jeffrey Coderre
Title: Associate Professor

Acknowledgements

Table of Contents

Table of Figures

8

Table of Tables

1 Introduction to Aviation Security and Explosives Detection

Exploitation of commercial air travel as a means for violence is not new: the first fatal hijacking occurred in 1947 and fourteen bombings of aircraft in-flight were made between 1965 and 2000 [1]. As air travel became commonplace, efforts were made to increase aviation security: guns and most knives were banned from planes and metal detectors and x-ray machines were employed to detect weapons concealed on passengers and in carry-on luggage. In spite of these attempts at securing air travel, the US airline industry was caught by surprise at its failure to detect hidden explosives with the in-flight bombing of Pan American Airlines Flight 103 in 1988. Increased funding for the Federal Aviation Administration, a new focus on improving x-ray detection, and investments in new explosives detection systems (EDS) followed the crash of Pan Am flight 103 [2]. However, the rarity of terrorist bombings of US carriers and the relatively small numbers of American citizens killed in aviation bombings since 1988 reduced the attention given to aviation security and many of the proposed security ideas presented in the Gore Commission Report following the crash of Trans World Airlines Flight 800 were delayed or ignored [3].

The terrorist attack on the United States in September of 2001 once again forced the issue of airline security into the public eye and altered the commonly held belief that random x-ray screening for explosives in checked luggage was sufficient to ensure the security of air travel [4]. In response to the attack, the United States initiated an effort to enhance the safety of air travel in many respects, including increased funding for investigation of new technologies for detection of explosives and a requirement mandating the screening of 100% of checked luggage on commercial air flights[i]. The screening methods used can be by machine, portable detectors, animals, by hand, or some combination of the above [5]. Time-consuming, intrusive, and prone to high false

---

[i] Initially, screening requirements adopted after 9/11/01 mandated 100% screening of luggage with x-ray systems. The infeasibility of this plan was quickly realized, and the regulations changed to require any means of screening for explosives such as manual search, x-rays, chemical trace swipes, etc.

positive rates, many of these techniques have been in use for decades and are ready for upgrades. The focus of this thesis is the development of a new explosive detection system based on neutron resonance radiography (NRR).

It is first necessary to explore the properties of explosives, current detection technology, and deployment and use of explosive detection systems. This appreciation for the technical capabilities of current explosive detection systems and those under development will enable a comprehensive understanding of the strengths that neutron resonance radiography can bring to aviation security.

1.1 Characteristics of Explosives

Before beginning a discussion of explosives detection, it is useful to first describe the properties of the explosives in question. Hundreds of different explosive compositions exist, from military explosives to those used in mining and other commercial applications, to powders, liquids, and propellants. The material properties of explosives vary over a wide range of densities, sizes and shapes. Most explosive types, such as powders, liquids, or solids, are made up largely of carbon, nitrogen, oxygen, and hydrogen, with densities spanning a range from ~ 0.8 g/cm^3 for powders to 2.0 g/cm^3 for military explosives [6, 7]. In general, military explosives are denser than other explosives since an increase in density corresponds to an increase in explosive power. Explosives rely on a fuel/oxygen mixture to provide their explosive power; the majority use nitrogen or nitrogenous compounds as the fuel. For this reason, many explosives have characteristically high nitrogen to oxygen ratios. Other elements that are present in explosives are carbon and hydrogen, while some contain chlorine, aluminum, silicon, and other elements designed to improve the performance of, or add effect to, the explosive reaction. Regardless of the exact chemical composition, the majority of the material is elements of low atomic number.

We have not tried to make a comparative assessment of the availability of different types of explosives to terrorist groups or others who would use them for nefarious purposes. For example, commercial explosives such as ammonium nitrate have been used in bombings and the ingredients are readily available, while military

explosives can be found in land mines and abandoned facilities in many countries. We have assumed that any explosive type could be secreted aboard an aircraft and the explosive detection systems in place must be able to reasonably distinguish any explosive material from common items found in luggage.

Most methods for detection of explosives rely on differences in the density of materials. Unfortunately, the density of the explosives discussed above is similar to the most common densities of organic materials and metals, and this shared low density can lead to significant problems in differentiating between harmless items and explosive material. Many common items such as shampoo, cosmetics, paper, clothing, and food are composed of the same four elements as explosives (C, O, N, and H), and therefore have densities that are very similar to those of explosives [8]. Figure 1.1 shows the range of densities and average atomic number of a variety of explosive materials, as well as the density and atomic number of items typically found in luggage on airplanes [9]. While all x-ray-based explosive detection systems are very good at distinguishing metals from organic materials, and more sophisticated x-ray systems can even determine the apparent density of low-Z materials, the overlap of densities between explosives and common items will continue to cause high false alarm rates in x-ray systems regardless of improvements in technology.
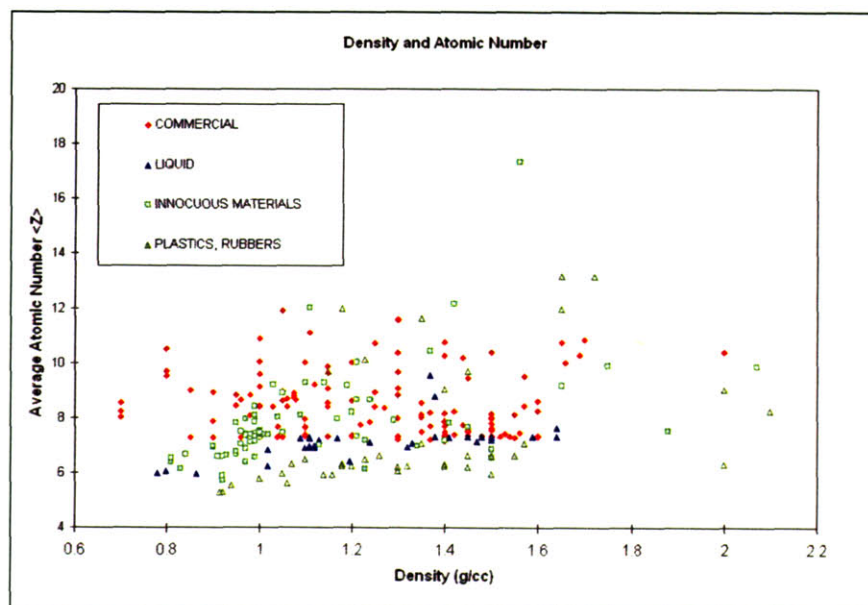
Figure 1.1: Density and atomic number of various materials [9]

13

Depicted in Figure 1.2 and Figure 1.3 are the nitrogen content to density ratio and the nitrogen to oxygen ratio respectively, of the same materials. It is obvious from these three charts that density alone will not reliably distinguish explosives from other items. Figure 1.2 indicates that knowledge of the nitrogenous component of the material in addition to the density can help to separate explosive material from other objects, but the difference is small and many items, such as common toys, are made of plastics that have similar amounts of nitrogen. Figure 1.3, on the other hand, shows that determining the nitrogen and oxygen components of a material will clearly separate innocuous material from most explosive compounds. Similarly, the carbon-to-oxygen ratio can provide a fourth metric, in addition to the density, nitrogen content, and nitrogen-to-oxygen ratio, by which to compare the elemental components of a material.

The carbon-to-oxygen ratio is especially important for explosives that contain no nitrogen. Chemical composition is a necessity for these types of explosives, as the density can vary widely and the lack of nitrogen makes trace detection of nitrogenous compounds difficult with existing equipment. These compounds are becoming more common; shoe bomber Richard Reid used a non-nitrogenous form of explosive in his failed attempt to destroy an airliner [10] and the liquid explosive scare in late summer 2006 was based on the same type of explosive [11].
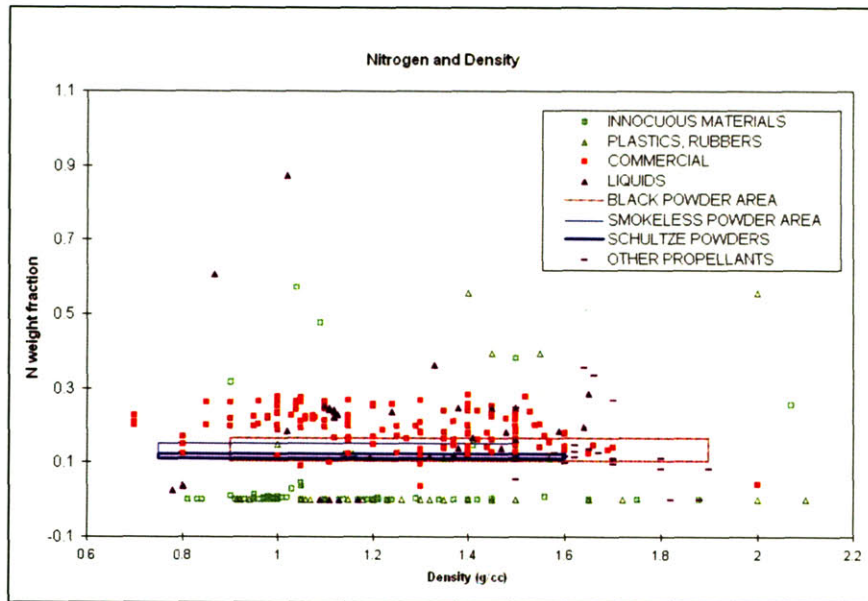
Figure 1.2: Nitrogen content and density of various materials [9]

Figure 1.3: Nitrogen and oxygen content of various materials [9]

Finally, the size, shape, and continuity of any suspicious compounds can provide helpful information when discriminating potential explosives from other materials. Any new explosives detection system should be able to both image the contents of luggage as

well as distinguish elemental composition for more accurate and efficient explosives detection.

1.2   Detection Theory

Detection of explosives in luggage – a situation in which the rate of incidence is extremely low, but the consequences of detection failure extremely high – presents unique challenges. More than 200,000 people per day pass through the larger airports in the United States; all their bags must be screened for explosives before being loaded on a plane. Regrettably, recent studies have shown that operators tend to misidentify threats as harmless due to their infrequency [12]. New detection systems must be able to quickly screen luggage and determine if a threat is present without demanding excessive operator intervention or extended time commitment.

The goal of any detection system is to correctly identify all threats and correctly pass over items that do not present a threat. False alarm rates, while generally unpublished, are known to be in the 10 – 30% range, and each of these false alarms must be checked by a secondary system[ii]. In a large airport, even a 10% false alarm rate means that thousands of bags must be screened in a secondary system, usually by hand. This contributes significantly to airport delays, lost luggage, and high expenses for airlines and airports.

Detection systems in airports can be thought of as a "tiered" system. The first tier is a detection system that every checked bag is subjected to, usually an x-ray inspection system. These "first-tier" systems are usually automated, fast, and relatively inexpensive, but also have high false alarm rates. In practice, the vast majority of luggage is harmless, meaning that almost none of the items identified as a possible threat are actually dangerous. However, each of these bags must be inspected again to ensure no explosive is present. The bags that are flagged as threats from the first tier system are subsequently

---

[ii] False alarm rates are generally not quoted in open literature due to security concerns. However, informal conversation with knowledgeable authorities, review of widely accepted figures, and quotes from carefully administered trials with new explosive detection systems indicate a wide range in false alarm rates. It is no secret that false alarms dominate the security environment in airports, as the incidence of bombs that are actually concealed in luggage is incredibly small.

16

sent for inspection in second-tier systems. Ideally, second-tier systems would be automated with low false-alarm rates and high sensitivity to explosive material, but currently, many airports use manual screening (discussed further in Section 1.3.4) as the second-tier screening system. Hand searches of luggage typically take approximately five minutes per bag (compared with thirty seconds per bag with x-ray scanners) and put the searcher in a situation where they are opening possibly hazardous items. New second-tier explosives detection technology should therefore be faster than hand searches and place operators in less dangerous situations in order to effectively replace manual screening as a second-tier system. To augment or replace x-ray systems as a first-tier system, the new system must be able to screen luggage more effectively than x-ray technology, with fewer false alarms and high confidence of detection, be less expensive, and, most significantly, require less than one minute per bag to perform. NRR is envisioned as a second-tier system, as the time required for inspection will be prohibitive for use as a first-tier system, but can easily replace hand-searches as a secondary system.

1.3 Explosive Detection Methods in Use

Fortunately, there are very few instances of explosives being smuggled aboard airplanes and current technology has performed reasonably well at ensuring the safety of passengers while expediting the boarding process. However, many of the explosive detection methods in use today are outdated, time-consuming, and can potentially miss dangerous items. Among these means of detection which are employed in airports today are x-ray detection, chemical tracing, canine detection, and finally, manual check. These methods will be described in more detail below.

1.3.1 X-Ray Detection

X-ray detectors are commonplace in the vast majority of airports across the world. X-ray scanners irradiate an object with a beam of low energy (50 – 150 keV) x-rays. The attenuated beam is subsequently detected and an image of the item is produced. Materials with high electron density, such as metals, attenuate x-rays by absorption or

scattering much more rapidly than low-Z materials. By scanning an object with x-rays, strong attenuation characteristics make high density materials stand out significantly from low-Z objects. X-rays can easily distinguish between metal and organic objects, but encounter difficulty differentiating between explosives and other items present due to their similar densities.

In recent years, technological advancements have improved x-ray scanners to the point where it is possible, to some degree, to determine the relative density of low-Z objects. These improvements include the addition of computerized tomography, or x-ray CT scanning [13], which enables those who analyze the images to see a computerized 3-dimensional image of the object in question to better determine its spatial form and any metallic components. Additionally, dual-energy x-ray scanners have been developed but not deployed [14]. In these systems, x-rays of two separate energies are used as probes. The same object will attenuate the two energies in different ways, and comparison of the attenuation can assist in a more accurate determination of the density of the object. However, these techniques indicate only a higher or lower density and generally cannot ascertain a value for the atomic number.

X-ray scanners are currently the most widespread explosives detection system due to their ease of use, relatively small size, low radiation shielding requirements, and economic advantage. They provide an essential way to determine the items in carry-on and checked luggage and can alert a screener to the presence of questionable and suspicious items. Unfortunately, the large amount of baggage screened and the similarity in density between explosives and common items makes it very probable that, regardless of the improvements in x-ray technologies, there will continue to be a great number of bags that will be flagged as requiring a manual check.

1.3.2 Canine Detection

Using animals for detection purposes is prevalent in many aspects of society: dogs are used to search for victims of natural disasters and building collapses, for detection of drugs at border crossings, and for detection of explosives. Canine olfactory systems are highly developed, and, in close cooperation with a handler, a dog can be trained to detect

concealed explosives. Dogs are trained to quickly pass over luggage, and any explosive residue present is picked up through the olfactory system. Sniffing exaggerates this effect and results in more residue deposition on the nasal sensors. Through training on real explosive material, the dog reacts to items that contain explosives. Although the exact means of detection is unknown, detection is dependent on the concentration of the explosive, meaning that small amounts of well-concealed material could be missed. The use of canines for explosives detection increased in the months following September 11, 2001, but has since been reduced significantly [15].

Although the use of dogs is a potentially excellent means of explosives detection, serious questions and logistical difficulties remain to be addressed before their use can be widespread. What dogs actually smell and what scents or compounds trigger a positive response is still unknown. Also unknown is the effect of human scents, contamination of explosive material, and the length of time the explosive has been concealed, on detection responses. Logistically, the training of both handler and canine is extensive and must be continued throughout the lifetime of the dog. Handlers are generally required to spend all their time with the animal as part of a team, even bringing the dog home when off-duty to care for it. Acting as a dog handler is a full-time job, and the extensive time and commitment required is unlikely to suit the needs of fast, efficient, and inexpensive explosives detection for luggage. Further, dogs must be trained to recognize all explosives; determining the appropriate training materials and ensuring that all explosives are identifiable is challenging and time-consuming.

1.3.3 Chemical Trace Detection

Chemical trace detection, like canine detection, uses the chemical vapors or residue left by handling explosive material to determine the presence of explosives in a package [16, 17]. Vapor samples are taken by testing some quantity of air around the object, or by blowing air across an object or a person to collect and analyze. When handled, explosive material can remain on hands, clothing, and containers. Particles can be collected by swiping luggage, clothing, or boarding passes, for example, with paper or a vacuum system. Once a sample is collected, it can be analyzed for trace amounts of

known explosives. Common methods of analysis are gas chromatography, ion mobility spectrometry, and mass spectrometry. These systems can positively and quickly determine the presence of explosive provided that enough of the explosive material is present in the sample; most systems require picogram amounts of material. The major drawback to chemical trace detection systems is that some explosive material must be present in the air or on the swiped area in order to determine the existence of explosives, and areas can be cross-contaminated.

1.3.4   Manual Search

Manual search of luggage is the oldest and most reliable means of ensuring that no harmful objects are carried or checked onto an airplane. Hand-searches of luggage are increasingly used now that all bags must be inspected. Once a bag has undergone inspection by x-ray systems, trace detection, or another form of explosives detection system, any bag that contains an item labeled as "suspicious" by detection algorithms must be opened and inspected by a person. Because false alarm rates for many detection systems can be high, luggage screeners must open a large fraction of checked bags. These hand searches are expensive, potentially dangerous, and time-consuming. Some groups have also complained that hand-searches violate the privacy of passengers by allowing screeners to open luggage and remove items deemed to be hazardous to air travel. However, because of the accuracy of manual searches, it is highly likely that the use of hand-searches of suspicious baggage will continue. It is obviously desirable, however, to reduce the number of manual checks, either by increasing the number of detection systems available or by reducing the number of false alarms.

1.4   Nuclear Methods for Explosives Detection

Unlike detection methods that are currently in use today and described above, nuclear methods for detection of explosives are potentially able to determine unique elemental composition, rather than bulk properties such as density. Nuclear techniques exploit the property of various materials to respond to probing radiation such as gamma

20

rays and neutrons. By making use of the distinctive differences in elemental response, nuclear detection methods are able to determine the elements present in an object. In this way, the detection system can positively identify material compositions as similar to known explosives without the uncertainty inherently present in density measurements. Nuclear methods also have the advantage of using highly penetrating radiation, enabling their use for large, densely packed luggage or cargo containers. While these systems have the potential to be a significant improvement over current technology, they are in general more expensive, more technologically advanced, and larger than current systems and many are still in the design and testing stage. The following section will describe the most advanced of the nuclear-based explosive detection systems.

1.4.1   Neutron Activation Methods

Multiple neutron activation methods exist today, all founded on the interactions of neutrons with nuclei that produce gamma rays for detection or imaging. When a thermal neutron is captured by another nucleus, the newly-formed isotope can emit a characteristic gamma-ray. Each element that captures a neutron emits one or more gamma rays with a unique energy; detection of gamma rays and subsequent spectroscopy can lead to determination of the elements present in an irradiated sample. If fast neutrons are used as the probing particle, inelastic scattering with low-Z elements, such as carbon, nitrogen and oxygen, also results in the emission of gamma rays. There are three main neutron activation explosives detection systems currently under investigation: Thermal Neutron Analysis (TNA), Fast Neutron Analysis (FNA), and Pulsed Fast Neutron Analysis (PFNA). Of these three methods, only PFNA has imaging capabilities.

Thermal Neutron Analysis [18, 19] uses thermal neutrons to probe the contents of a piece of luggage. Fast neutrons are produced via a ^{252}Cf source or a small accelerator and then thermalized to produce a collimated beam of thermal neutrons. TNA mainly exploits the thermal absorption cross-section of nitrogen-14, found in the majority of explosives. When a thermal neutron is captured by a ^{14}N nucleus, an easily detectable 10.8 MeV gamma ray is emitted. However, the cross-section of ^{14}N at thermal neutron energies is only 80 mb, requiring many starting neutrons to produce an acceptable signal

from the resulting gamma rays. In addition, only nitrogen is detected, and usually the nitrogen content of the entire bag of luggage instead of a single item. Despite these limitations, TNA systems have been built and are in limited use today.

Fast Neutron Analysis [20, 21, 22] is technically a more robust and reliable system for explosives detection than TNA because inelastic scattering off light elements results in the ability to detect quantities of carbon, nitrogen, and oxygen, which improves identification of material composition. FNA uses a D-T 14 MeV microsecond-pulsed neutron source. Unlike the high-energy nitrogen line characteristic of thermal neutron capture, inelastic scattering off carbon, nitrogen, and oxygen results in gamma rays that are generally of energies between 2 and 6 MeV. These relatively low energy[iii] gamma rays can be difficult to distinguish from background radiation. Similar to TNA, the entire nitrogen, oxygen, and carbon contents of the luggage are determined, rather than any single object. FNA also runs into difficulties in practice as the cross-sections for neutron inelastic scattering and the sensitivity of gamma detectors is low. The most significant challenge for FNA is the loss of signal due to detector solid angles and the $1/r^2$ behavior of radiation. Not only is the neutron beam subjected to a $1/r^2$ loss, but the signal from the gamma rays produced is also reduced by another factor of $1/r^2$, leading to an unavoidable signal loss of $1/r^4$[iv]

Pulsed Fast Neutron Analysis is an improvement on FNA by combining TNA, FNA, and in some cases time-of-flight (TOF) measurements to determine the contents of an object. PFNA uses a nanosecond pulsed beam of 8 MeV fast neutrons produced by a particle accelerator in a D-D reaction. The beam is collimated such that a small cone of the object under investigation is irradiated. Subsequently, the object is moved so that another fraction is irradiated, and so on until the entire object has been scanned. While the beam is on, gamma rays are produced by inelastic scattering in the object. In the

---

[iii] While gamma rays with energies in the 1-5 MeV range are not "low energy", when compared to other naturally occurring gamma rays from elements such as potassium (1.4 MeV) and thallium (2.6 MeV), they are comparable to the background radiation. Only when the energy of the gamma ray is significantly higher than most background radiation, such as the 10.8 MeV gamma emitted from ^{15}N, is it readily detectable *and* distinguishable.

[iv] This assumes the distance between the source and the object and the distance between the object and the detector is a magnitude r. If the two distances are not similar, in other words a distance r between the source and the object and a distance R between the object and detector, the intensity is proportional to $1/(r^2*R^2)$.

lapse time between pulses, time-of-flight (TOF) measurements can be made to determine the time lag between the arrival of the gamma rays and the initial neutron pulse used as a probe. This time-difference-of-arrival method provides a way to separate gamma rays produced by the inelastic scattering from background radiation and can determine where in the object the gamma ray was generated. PFNA thus provides a means of distinguishing elements that are present, and, due to the small cones of illumination, an inherent imaging capability. Drawbacks to this technique include those inherent to FNA and TNA, as well as the requirement of long flight distances for TOF measurements.

1.4.2   Gamma-Ray Detection Methods

These explosive detection techniques use gamma rays and their interactions with nuclei to determine the presence of various elements and provide imaging capability. Gamma rays provide non-intrusive means of inspection that is similar to both x-rays and neutron activation methods, but gamma rays are more penetrating than x-rays but easier to shield than neutrons. Two explosive detection methods using gamma rays are described below; traditional radiography, or direct imaging, is not discussed here, as simple images do not provide elemental information.

1.4.2.1   Gamma Resonance Absorption

Gamma Resonance Absorption [23] uses high-energy gamma rays (9.17 MeV) as the penetrating form of radiation, which is attenuated by resonance absorption in the presence of high levels of nitrogen-14. The resonance in nitrogen-14 is unusually broad, ~135 eV wide, which still places restrictions on the energetic stability of the accelerator. The gamma rays are produced through a (p,γ) reaction with carbon-13 or sulfur-34, where the protons are produced by an accelerator at energies of 1.75 MeV for carbon-13 or 1.89 and 2.79 MeV for sulfur-34. Detectors measure the attenuation of the gamma ray beam due to the nitrogen-14 in the sample and form an image that can be analyzed for spatial resolution of areas of high nitrogen density. Like many other "elemental" detection

23

methods, GRA only provides information on nitrogen content of an object, and requires very high proton currents in the tens of milliamps range [24].

1.4.2.2 Nuclear Resonance Fluorescence

Nuclear Resonance Fluorescence (NRF) is a technique that can potentially be used for detection of high explosives and fissile material, or any material with atomic number greater than two [25]. Except for hydrogen and helium, all nuclei have resonance features between one and eight MeV that have a high photon capture cross-section, on the order of hundreds of barns but with a very narrow width of 1 eV or less. When Doppler broadening and recoil effects are accounted for, the effective width is ~10 eV with a cross-section of 3 or 4 barns. When nuclei are irradiated with a broad-spectrum x-ray source (Bremsstrahlung radiation) the incoming photons of the energy corresponding to the resonance energy are absorbed and the nucleus re-emits a photon of a different energy, typically in the several MeV range. By looking in the backward direction, Compton scatters are below 511 keV and thus below the energy of the emitted fluorescence.. These photons are then detected and imaged. Nuclear resonance fluorescence benefits from having no requirements on the energy of the initial x-ray source other than that it spans a large range of energies. In other words, the x-ray energy does not need to correspond to any specific element in question. This makes the source radiation for NRF easier to develop and deploy with no loss in sensitivity to any elements. NRF relies, however, on a system of multiple expensive detectors. Until the cost of the system is reduced, it is impractical for a luggage situation.

1.4.2.3 Photonuclear Activation

Photo-nuclear activation uses a beam of Bremsstrahlung radiation produced by an electron accelerator to activate nitrogen in objects under irradiation. When x-rays are captured by nitrogen-14, the (γ,n) reaction produces nitrogen-13, which radioactively decays by emitting a positron. The positron quickly slows down and produces a 511 keV gamma ray from positron annihilation. This 511 keV line is subsequently detected; the

strength of the line is an indication of the amount of nitrogen present. Unfortunately, 511 keV gamma rays are easily shielded by the material in which they are produced, and very high electron currents must be used in order to generate the number of x-rays needed for adequate signal-to-noise ratios.

1.4.3   Neutron Transmission Methods

Neutron transmission methods for explosives detection are based on neutrons as the penetrating radiation and as the detection mechanism. The neutron beam irradiates the object in question and the elements present in the object attenuate the beam to some extent based on unique signatures of the neutron cross-section. The neutrons that pass through the object unaffected are detected and analyzed. A few of these methods are described here.

1.4.3.1   Pulsed Fast Neutron Transmission Spectroscopy

Pulsed-Fast Neutron Transmission Spectroscopy (PFNTS) [26] uses the $^9Be(d,n)^{10}Be$ reaction to provide a nanosecond pulsed neutron beam with a broad energy spectrum. Similar to x-ray systems, the attenuation of the beam is measured as the neutrons pass through the object. The resonance features in the neutron cross-section of individual elements present attenuate the neutron beam, and the transmitted neutrons are recorded as a function of time-of-flight and hence of energy. The ratio of transmitted to incident neutrons can be analyzed to determine a two-dimensional elemental density map of the object. In contrast to x-rays, neutrons are more likely to be attenuated by low-Z elements rather than metals, so PFNTS is more sensitive to the composition of explosives than are x-ray systems. Monte Carlo modeling has shown that this technique can determine the carbon, nitrogen, oxygen, and hydrogen content of the object under inspection due to their distinct attenuation of neutrons. While this method is promising, the long distances for time-of-flight measurements result in considerable space requirements and low signal-to-noise ratios.

1.4.3.2   Neutron Resonance Radiography

Neutron Resonance Radiography [27] is the final method of explosives detection discussed in this chapter and will be the focus of the remainder of this thesis. While a detailed review of the theory and use of NRR is presented in Chapter Two, a brief summary is offered here. The fundamental principle of NRR lies in the use of resonance features of the total neutron cross-section to compare images taken at neutron energies on and off resonance peaks in the cross-section, similar to the principles of PFNTS. Each element has a unique total cross-section that determines the probability that an incoming neutron of a particular energy will be scattered or absorbed. By measuring the transmission of neutrons as a function of energy, one can determine the elements present in an object and their spatial distribution.

For use in explosives detection, NRR concentrates on determining the amount of carbon, nitrogen, oxygen, and hydrogen present in an object. Multiple-element resolution capability allows for an accurate analysis of an object's identity by providing more information on all elements in question rather than solely determining the nitrogen composition. As mentioned in Section 1.1, many explosives have typical oxygen to nitrogen ratios that allow for improved identification, and NRR can provide this information in ways that other explosive detection systems cannot.

1.5   Contributions of This Thesis

This thesis is motivated by the need to develop new methods to improve baggage inspection both by speeding up the screening process and by reducing false alarm rates and the necessity of intrusive hand inspections. Previous work [27] has identified fast neutron resonance radiography as a promising means of inspection. This technique has the potential to provide real-time imaging of baggage components, elemental discrimination and mapping, and can be implemented using predominantly off-the-shelf components which will reduce the cost of the system to levels comparable with current explosive detection systems. By determining the elemental composition and density as well as the size and shape of the object in question, the likelihood of positive identification of explosive is enhanced. This thesis builds on that body of theoretical

work and simulations by focusing on the development of a prototype NRR explosive detection system at the Massachusetts Institute of Technology utilizing a particle accelerator, deuterium gas target, and scintillator/CCD camera combination for imaging of small objects.

We have developed an accelerator-based, deuterium gas target system to provide fast neutrons of varying energy and a CCD-based detection system. In the process, we have developed a novel pressurized gas target that can withstand the heat deposition and stresses induced by a high current beam of high-energy deuterons. It is envisioned that this system could be used as a "second-tier" screening system for checked luggage in airports. The use of this system would decrease the number of intrusive manual inspections, reduce the number of false alarms, and increase the security of airline travel. This work also provides the basis for future airport screening systems such as the screening of cargo containers for incendiary devices or, potentially, for the detection of drugs at border crossings.

This thesis is organized into seven chapters. The second chapter is a review of neutron radiography and the use of NRR for baggage screening. This chapter will also discuss the primary components and specifications of an NRR system for explosive detection. Chapters Three, Four and Five will focus on preliminary results used as a starting point for this thesis, the gas target design, and the neutron detection system, respectively. Chapter Six presents the results of the final imaging system and the capabilities of a prototype NRR explosives detection system. The thesis work is summarized in Chapter Seven.

2 Neutron Resonance Radiography

Radiography is the creation of two-dimensional images using a form of radiation; the most common type of radiography uses x-ray radiation. In transmission radiography, the object in question is placed in the line of a radiation beam and the amount of radiation that passes through the object is recorded. The extent to which the initial beam is attenuated results in a two-dimensional image depicting areas where the initial beam of radiation has been attenuated to differing extents. When x-rays are used as the primary form of radiation, the image formed is of electron density. In this case, areas where the initial beam has been attenuated significantly indicate the presence of dense, or high-Z, material such as metal. Analysis of the radiographic images highlights the contrast between areas of high and low density. Among other applications, radiography is commonly used to show broken bones, dental cavities, or the concealed contents of a bag for security purposes.

Radiography using neutrons has been used for a variety of purposes. Because x-rays are highly attenuated by high-density materials, they are ineffective in situations where a significant amount of metal is present. In the presence of low-density or low-Z material, on the other hand, x-rays do not have the capability to distinguish the different densities or identify different materials. Because of their scattering properties and insensitivity to metals, neutrons can take on the role of imaging radiation in situations where low-Z material must be imaged. Neutrons have been used to produce images of corrosion in metals [28], of diamonds in kimberlite (an igneous rock formation) [29], and as previously discussed, as a tool for imaging luggage and cargo.

Using fast neutrons for radiography is more difficult in some ways than x-ray radiography. The ability of fast neutrons to penetrate very thick, dense objects means that they are also very difficult to shield and therefore require isolated areas with extensive shielding for safety considerations. Neutrons are more difficult to produce than x-rays, and also harder to detect. These properties have limited the use of fast neutrons for imaging but recent work has improved both production and detection capabilities. These developments have allowed for new applications involving fast neutron imaging.

This chapter will illustrate the use of fast neutrons for imaging, determination of elemental composition, and their application to explosives detection. The first section will explain the principles behind fast neutron resonance radiography. The following sections will review the necessary components of an explosives detection system using NRR, including neutron production, detection, and imaging. The final section will examine previous research and the results of initial experiments using NRR for explosives detection.

2.1 Fast Neutron Resonance Radiography

Neutron radiography is the use of neutrons for the creation of an image. For the purposes of explosives detection, imaging alone is insufficient and methods to determine elemental composition must supplement the neutron images. Neutron resonance radiography augments the neutron images by incorporating resonance features of the fast neutron cross-section to provide information on an object's chemical components. This technique has been proven for simple geometries and cases where only a single element is of interest, such as large carbon inclusions hidden inside rock. Multiple-element resolution is the subject of this thesis, but the technical aspects of NRR are identical whether one element or several are of concern.

The fundamentals of fast neutron resonance radiography lie in the use of the resonance features in fast neutron cross-sections. As an example, Figure 2.1 shows the total neutron cross-section for carbon-12 over an energy range of 1-10 MeV. Although there are multiple interaction mechanisms that a neutron can undergo when it encounters a nucleus, for light nuclei, scattering is dominant. For the purposes of NRR, the elastic scattering neutron cross-section for all light nuclei is essentially the total neutron cross-section.
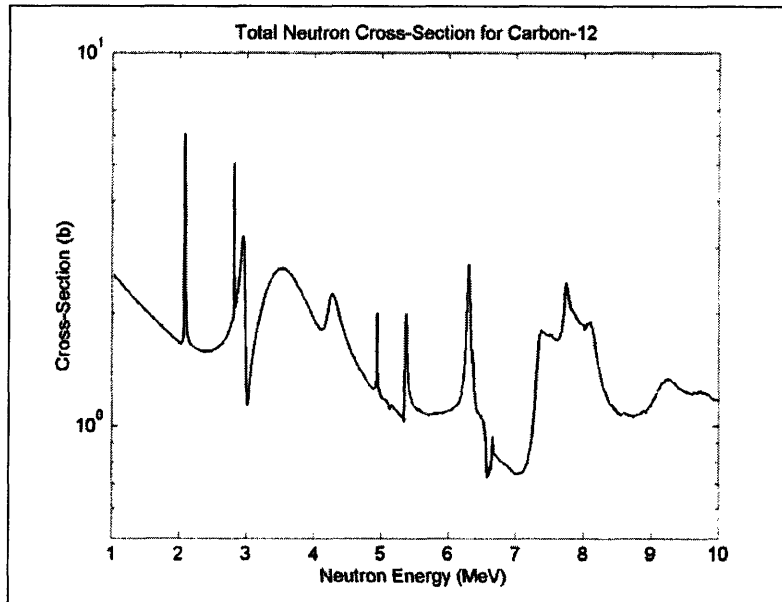
Figure 2.1: Carbon-12 total neutron cross-section. Data are from the
ENDF/ B-6.1 neutron cross-section database.

Apparent in Figure 2.1 are the resonance features of the cross-section for neutrons of high energy (greater than 1 MeV). The resonance features markedly increase (or decrease) the probability that neutrons of certain energies will be scattered by a nucleus. An incoming neutron with energy of 8 MeV, for example, will have a higher probability of being scattered than a neutron with energy 7 MeV. Neutrons that are not scattered continue to pass straight through the material unaffected. In the same way that high-density materials attenuate x-rays, scattering from nuclei attenuates the neutron beam. This attenuation is the basis of neutron resonance radiography. The attenuation of the neutron beam follows the exponential attenuation law:

$$I = I_0 e^{-\frac{\sigma \rho N_{Av}}{A} t}$$

Eq. 2.1

where I is the number of neutrons after attenuation, I_0 is the initial number of neutrons, σ is the microscopic cross-section in cm^2, ρ is the density in g/cm^3, N_{Av} is Avogadro's number, A is the atomic number, and t is the linear thickness of the object. This can be rewritten using the areal density, more useful for NRR, as:

30

$$I = I_0 e^{-\mu x}$$

where μ is the mass attenuation coefficient in cm^2/g, and x is the effective areal density (in dimensions of g/cm^2) of the material.

Single-element NRR has been used in situations where only one element is of interest and is the most straightforward way of performing NRR [29]. Radiographic images are taken at neutron energies corresponding to a peak and a valley in the neutron cross-section. The pixel-by-pixel difference in intensity between these two images corresponds to the amount of the element in question. This difference allows one to construct a two-dimensional map of the elemental concentration. As an example, referring to Figure 2.1, the first "on-resonance" radiographic image can be taken by 8 MeV neutrons, corresponding to the large, broad peak in the cross-section. The contrasting image, or the "off-resonance" image, can be taken using neutrons of 7 MeV. In areas of the object where the carbon content is high, the second, off-resonance image will have a higher intensity in these areas than the first, on-resonance image. The difference in intensity corresponds to the amount of carbon causing the neutron beam attenuation. Mathematically, the contrast can be written by using the neutron attenuation governed by Eq. 2.2 at two different energies:

$$C = 1 - e^{-[(\mu x)_1 - (\mu x)_2]}$$

where the quantity μx is dependent on the neutron energy.

This technique to identify single elements can be expanded to multiple elements using peaks and valleys in the cross-section corresponding to regions where the element of interest has resonance features but the other elements in question do not. For example, if four elements are of interest, a series of eight images would be taken using neutrons with eight different energies. The eight energies would be chosen to create four pairs of images, with one energy in each pair corresponding to a resonance peak for a specific element and the other energy corresponding to a resonance valley for the same element. The four pairs of on- and off-resonance radiographs for the four elements can then be analyzed to determine the areal density of each element in each pixel by calculating the difference in intensity in the image pairs. In practice, however, it is often difficult if not

impossible to find energy pairs where the neutron cross-section is constant for all but one element. Figure 2.2 shows the cross-sections for the four most common elements of interest, hydrogen, carbon, nitrogen, and oxygen. Unfortunately, hydrogen has no resonance features, but the variation in the resonance patterns of the cross-section is obvious for the other three elements. Multiple features in each element correspond to an effective difference in the cross-section between the peaks and valleys of up to several barns. Any of these features can be exploited to create contrasting radiographic images. However, as shown in Figure 2.3, many of these resonance features overlap. The variation in the cross-section for the other elements leads to miscalculations in elemental composition, as the intensity of the neutron beam will be affected by the variation in the cross-section of the other elements. Single-element NRR has been applied to situations where only one element, namely carbon, is of interest, as well as circumstances in which determination of the density of multiple elements is desired [27, 29].
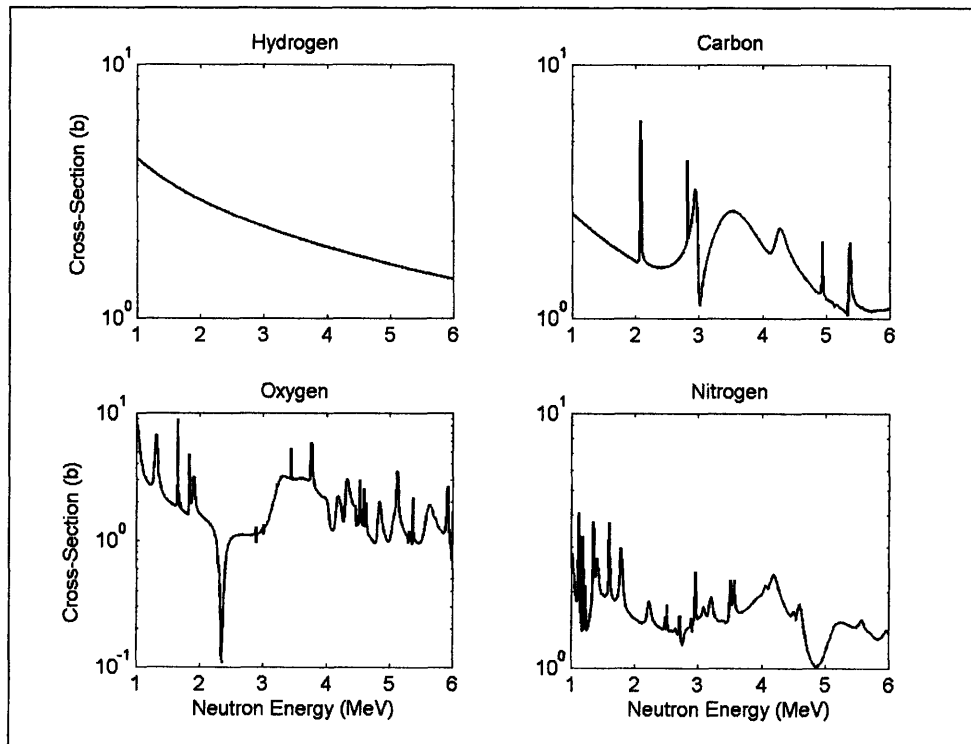
Figure 2.2: Total neutron cross-sections for elemental H, C, N, and O
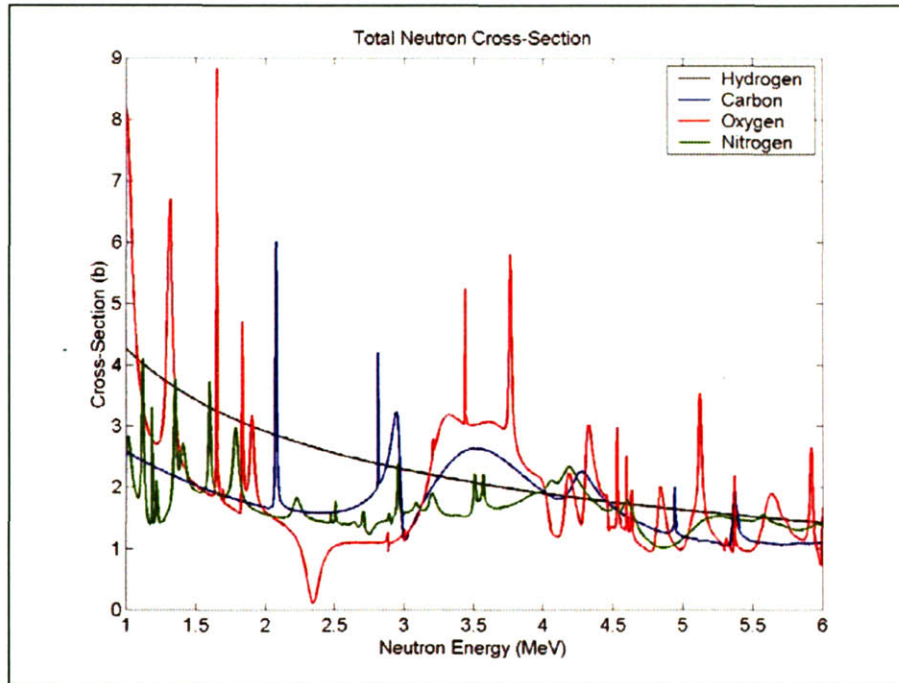
Figure 2.3: Total neutron cross-section for HCNO. This plot shows the cross-section for ^{1}H, ^{12}C, ^{14}N, and ^{16}O for neutrons of high energy. Especially obvious are the resonance features for C, N, and O over this energy range. Hydrogen lacks any resonance features over the entire neutron spectrum.

Single-element NRR is most useful when the elemental density of only one element is of interest and therefore opportunities for choosing neutron energies to create the radiographic images are greater. When more than one element is of interest, it is more effective to use multiple-element NRR. Multiple-element NRR still relies on the resonance features of the neutron cross-section, but does not require that the cross-section for all other elements be constant in areas where an element of interest has resonance features. In this way, the number of neutron energies and corresponding resonance features available for exploitation is increased [30].

For multiple-element NRR, neutron energies are chosen to ensure that there is a radiographic image taken where a significant difference in the cross-section for a single element exists. Each pixel in the resulting image can be represented by an equation:

$$\sum_i A_{E_1,i} X_i = B_{E_1}$$

Eq. 2.4

33

where X_i is the density fraction of the ith element, $A_{E1,i}$ is the attenuation coefficient for the ith at the first energy, and B_{E1} is the intensity of the pixel at the first energy. The attenuation coefficients are determined performing calibration experiments with known objects (the procedure will be discussed further in subsequent chapters). For purposes of the illustration of NRR here, it is sufficient to state that the attenuation coefficients are known quantities. Using this equation, unlimited numbers of elements could be determined so long as there are resonance features in the cross-section allowing radiographic images to display differing amounts of neutron attenuation.

For purposes of explosives detection, the four elements of interest are hydrogen, carbon, nitrogen, and oxygen. As explained in detail in Section 1.1, knowledge of the nitrogen, oxygen, and carbon densities can distinguish explosive material from other material found in luggage. A fifth "element" representing all elements other than hydrogen, carbon, nitrogen, and oxygen is added to account for the other elements common to luggage, such as aluminum. Referring to Eq. 2.4, we can construct a series of equations representing the elements in question, the attenuation expected at each neutron energy, and the resulting intensity for each pixel:

$$A_{E_1,H}X_H + A_{E_1,C}X_C + A_{E_1,N}X_N + A_{E_1,O}X_O + A_{E_1,Other}X_{Other} = B_{E_1}$$

$$A_{E_2,H}X_H + A_{E_2,C}X_C + A_{E_2,N}X_N + A_{E_2,O}X_O + A_{E_2,Other}X_{Other} = B_{E_2}$$

$$A_{E_3,H}X_H + A_{E_3,C}X_C + A_{E_3,N}X_N + A_{E_3,O}X_O + A_{E_3,Other}X_{Other} = B_{E_3}$$

$$\vdots$$

$$A_{E_n,H}X_H + A_{E_n,C}X_C + A_{E_n,N}X_N + A_{E_n,O}X_O + A_{E_n,Other}X_{Other} = B_{E_n}$$

Eq. 2.5

In this series of equations, B_{En} is the intensity of the pixel at the nth neutron energy. The attenuation coefficients, A, are unique to element and energy and depend on the neutron cross-section at the specific neutron energy at which the image is taken. The elemental fraction, $X_{element}$ is the quantity of interest that must be solved for analytically. Once the intensity is known for each radiographic image, solving for the elemental content is simply a matter of solving a system of equations. This allows a pixel-by-pixel elemental map to be created, highlighting the elemental content of each object in the bag as well as providing an image of the contents of the luggage.

In principle, the amount of any number of elements can be determined using Eq. 2.5, so long as the cross section of each individual element varies over the energy range in question. However, additional elements will make solving for the individual components more complicated. As most objects of interest in neutron radiography are made of carbon, nitrogen, oxygen, and hydrogen, these elements are of primary interest. For certain applications, adding one or more elements tailored to items of interest can be helpful. For example, for the detection of illegal drugs, chlorine can be added as a fifth element.

2.2 NRR System Configuration

A complete NRR system itself is fairly straightforward, shown below in Figure 2.4, even if the individual components are complex.
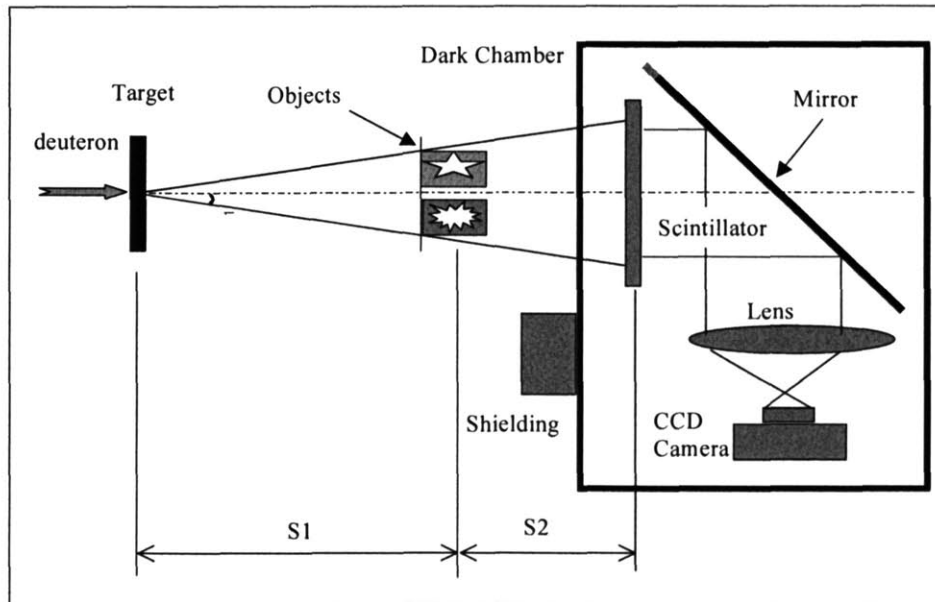
Figure 2.4: NRR system configuration [27]

The NRR system envisioned relies on an accelerator-based neutron source (Section 2.3). The object in question is placed some distance away from the neutron source, while the scintillator is placed directly behind the object. The two distances are

chosen to optimize the magnification and focus of the object of interest. The scintillator and CCD camera are placed in a shielded, dark chamber to isolate the camera from external sources of light, as well as shield it from extraneous neutrons and gamma rays. A mirror is placed at a 45° angle to both the scintillator and the camera, allowing light from neutron interactions in the scintillator to be redirected to the camera but shielding the camera from the direct neutron beam (Sections 2.4 and 2.5). The individual components of this system are the subjects of the following sections.

2.3 Neutron Production

Fast neutrons can be produced in a variety of ways [31]. Nuclear reactors provide a steady flow of neutrons with average energies of 2 MeV and some higher energies from fission reactions. Some radioactive elements, such as californium-252, have a spontaneous fission branch which produces neutrons. Finally, accelerators can produce neutrons via nuclear reactions between the accelerated particle and gas targets, solid targets, and spallation targets. All of these systems have been used, with varying degrees of success. Nuclear reactors are obviously unsuited for neutron production in an airport screening environment. Radioactive elements cannot be turned off, often emit other forms of undesired radiation, and do not provide the variation in neutron energy required for NRR. Accelerators, due to their relatively small size and ease of use, are considered the neutron production system of choice for NRR. Neutrons are produced using an accelerator by colliding the accelerated particle (usually a proton or deuteron) with a target system. The target is made of a material that undergoes a nuclear reaction, usually an A(p,n)B or A(d,n)B reaction, to produce sufficient neutrons for radiography. Neutron production reactions that have been studied in detail include $^7\text{Li(p,n)}^7\text{Be}$, D(d,n)T, $\text{D(d,n)}^3\text{He}$, and $^9\text{Be(d,n)}^{10}\text{Be}$ reactions. Candidate accelerator systems, nuclear reactions, and targets for neutron production are discussed in the following sections.

2.3.1 Particle Accelerators

Accelerators were developed to provide a reliable beam of charged particles for investigating nuclear interactions. Various accelerators have been designed to serve a variety of purposes, including long linear accelerators, cyclotrons, radiofrequency-driven accelerators, and electrostatic machines [32]. An accelerator system for NRR, if deployed in high-throughput environments such as airports, must meet the following requirements: It must be highly reliable; should be simple to operate by those who have minimal training; maintenance requirements should be minimal and performed on-site; must have a small footprint; and the accelerator must be comparably priced to current x-ray systems already installed at many airports. Of these requirements, the most important is that the accelerator is reliable and stable. The accelerator must operate for long stretches, typically on the order of more than 12 hours, without significant difficulty, and the beam characteristics must be reproducible over extended periods. Two types of accelerators meet these requirements and have the capability to produce neutrons of the energy essential for NRR: electrostatic accelerators and radiofrequency quadrupole (RFQ) accelerators. These types of accelerators are equally capable of accelerating either protons or deuterons, the primary particles used in neutron reactions to produce neutrons.

2.3.1.1 *Electrostatic Accelerators*

Electrostatic accelerators are based on a relatively simple design: an ion source creates charged particles, which are then accelerated through a potential drop by a series of electrodes. For positively charged particles, such as NRR, a positively charged electrode would be placed at the ion source and a negatively charged electrode at the beamline exit; the positively charged particles would be subjected to the voltage difference between the two electrodes. Magnetic fields are often used to focus the beam of particles at the entrance and exit of the accelerating column. Electrostatic accelerators provide a constant beam of charged particles of desired energy, and can be designed to tune the particle energy over a wide range of energies for various applications.

Tandem accelerators improve upon this design by incorporating a second acceleration stage. The terminal voltage, or highest voltage that the machine can achieve,

is located in the middle of the acceleration column. A negatively charged ion is produced and accelerated towards the high voltage electrode, where it is stripped of its electrons. This now positively charged particle is then accelerated away from the electrode and back to ground, attaining an energy twice that of the electrode voltage.

2.3.1.2   RFQ Accelerators

Radiofrequency Quadrupole ion accelerators have been used for a variety of applications. As compared to electrostatic machines, they are considerably more compact and generally can produce higher average currents, although they operate at a fixed energy with a particular ion. They have been shown to be a reliable source of deuterons in the 1-5 MeV range [33]. Instead of a static electric field for acceleration of charged particles, radio frequency energy is used to accelerate the particles to the desired energy. Positively charged ions are injected into the accelerating cavity where four electrodes accelerate the particle. An oscillating electric field is employed to simultaneously accelerate, bunch, and focus the charged particles, resulting in a high-current pulsed ion beam. High voltages are not required for acceleration up to a few MeV as in static machines.

RFQ accelerators are generally much simpler to use than most electrostatic accelerators as the primary operational parameter is the RF input power and easily turn the beam on and off. These are very positive attributes in a commercial setting, where ease of use and the minimization of stray radiation fields are highly important. However, RFQ accelerators are configured to accelerate only a single type of particle to a predetermined energy; very limited changes to the final particle energy can be made once the accelerator is constructed. Thus, a single machine cannot be used for other applications and must be built to specific, predetermined parameters.

2.3.2   Nuclear Reactions

Neutrons produced for NRR must have certain qualities if the system is to work as designed. First, the neutrons must be monoenergetic, or very close to it, over an angular span of approximately ten degrees. As discussed further in Section 2.2, the object to be

imaged spans an approximately 10° cone extending from the neutron source at a distance of one meter. In order to take advantage of the sharp peaks and valleys of the cross section and to compare and contrast images, the neutrons within the cone subtended by the object must all be the same energy. This requires the use of a "thin" target, or one in which the energy of the incoming particle does not decrease by more then 500 keV across the target material. Additionally, the energy spectrum of the neutrons must span a range of energies from 2 MeV to 5.5 MeV to take advantage of the many features in the cross-sections of carbon, nitrogen, and oxygen over these energies (see Figure 2.2). This can be accomplished in two ways: by varying the energy of the incoming particle to affect the energy of the outgoing neutrons, or by using a nuclear reaction that produces a range of neutron energies. Finally, the neutron beam should not be contaminated by gamma rays. Gamma rays can be produced by deuteron or proton impingement on beam tubes, the beam stop, or other accelerator components as well as through some nuclear reactions. They can create an added background that deteriorates the final neutron images by degrading the contrast imparted by neutrons of differing energy. The choice of a neutron production reaction should aim to minimize the gamma ray yield.

Many elements have the potential to be used as the target material in an accelerator-based neutron radiography system. The most commonly used elements for neutron reactions are beryllium, lithium, and deuterium as target materials; the corresponding nuclear reactions are $^9Be(d,n)^{10}Be$, $^7Li(p,n)^7Be$, and $D(d,n)^3He$. The beryllium reaction is unsuitable for NRR, however, due to its broad neutron spectrum and high gamma ray yield and will not be discussed here [34].

2.3.2.1 The $^7Li(p,n)^7Be$ Reaction

The $^7Li(p,n)^7Be$ reaction has been used in previous studies of NRR applications [28, 29]. The lithium reaction is endothermic, and results in a neutron and a beryllium atom that can be in either the ground state or an excited state:

$$^7Li + p \rightarrow {}^7Be + n - 1.646 MeV$$
$$^7Li + p \rightarrow {}^7Be^* + n - 2.076 MeV$$

Eq. 2.6

39
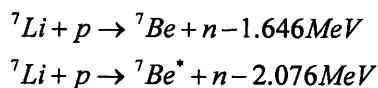
The excited beryllium atom subsequently emits a 428 keV gamma ray when de-exciting. The endothermic nature of the reaction requires threshold proton energies of 1.88 MeV for the ground state reaction and 2.37 MeV for the reaction resulting in an excited beryllium atom. The ratio of the cross-section of these two reactions is shown in Figure 2.5.
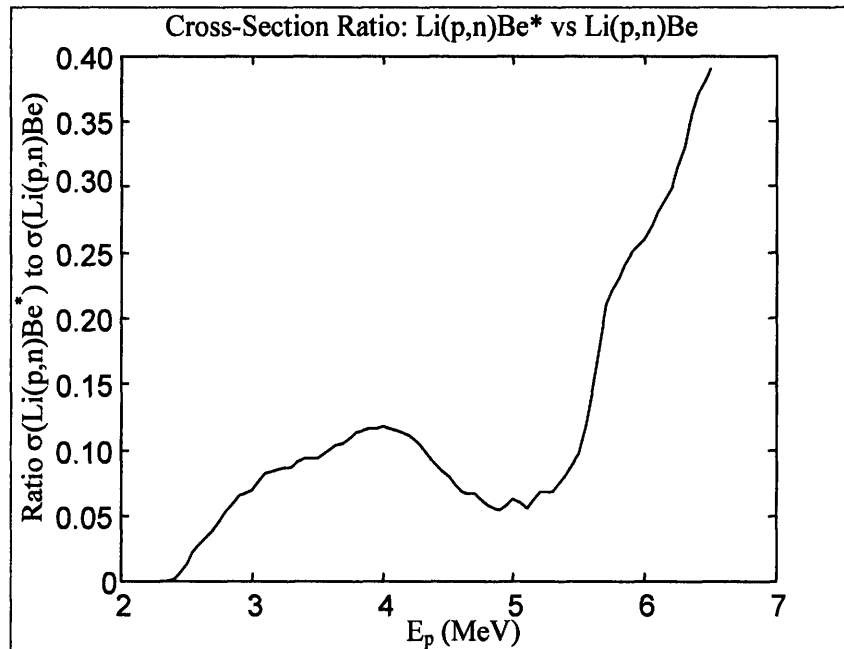
Figure 2.5: Cross-section ratio of ^{7}Li(p,n)^{7}Be reactions

The ratio of the cross-section of the two ^{7}Li(p,n)^{7}Be reactions shows that the dominant reaction results in a neutron and a ground-state beryllium atom if the proton energy is below 5 MeV. At these proton energies, the neutron yield from the ^{7}Li(p,n)^{7}Be reaction can be characterized as mostly monoenergetic, contaminated by low energy neutrons from the excited state reaction.

The neutrons resulting from the p-Li reaction are forward collimated and the energy is dependent on the angle at which they are produced. In order to produce neutrons of sufficient energy to take advantage of the cross-section features in the 5 – 6 MeV range, protons of at least 7 MeV must be used. Figure 2.6 below shows the

entire neutron spectrum as a function of angle, using 7.5 MeV protons, based on standard, non-relativistic kinematics [35].
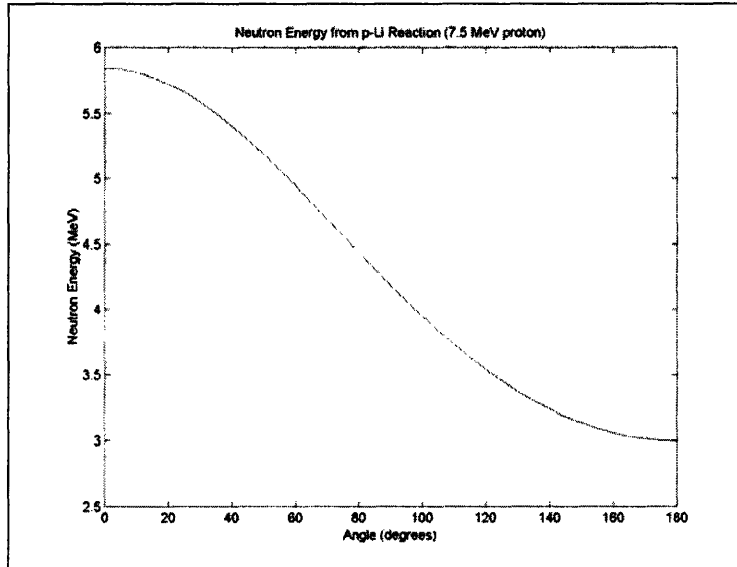
Figure 2.6: Neutron energy as a function of angle from the p-Li reaction

As shown in more detail in Figure 2.7, the energy of the neutrons decreases slowly with angle, allowing for an entire object to be irradiated by a beam of essentially monoenergetic neutrons as long as the object is within a 10° cone.
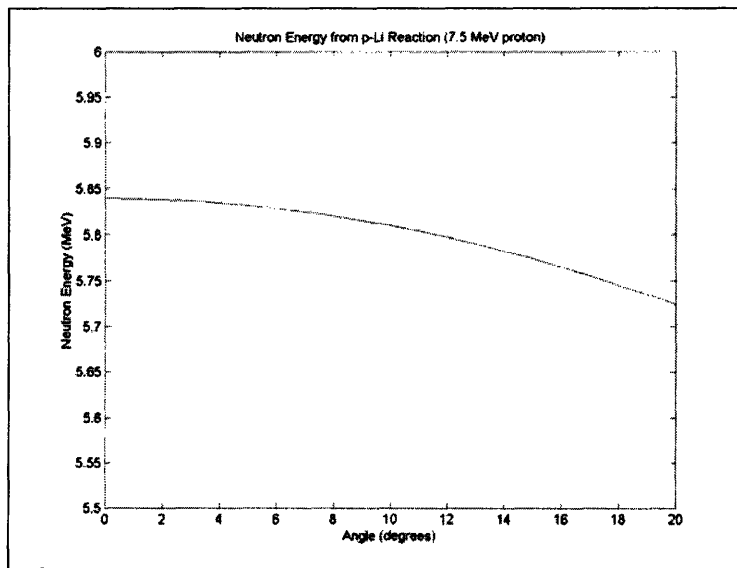
Figure 2.7: Neutron energy from p-Li reaction at small angles

The p-Li reaction generally has a high gamma-ray yield, due to both the decay of the excited state beryllium and, to a larger extent, to proton inelastic scattering within the lithium and other material in the target. Thin lithium targets (~50 keV) cause proton scattering off the backing of the target, while thick lithium targets increase the number of protons scattered in the lithium itself. Proton scattering off lithium results in a 479 keV gamma ray. The number of gamma rays produced by inelastic scattering reactions increases with proton energy, and has been shown to reach ratios of almost two gamma rays produced for every one neutron.

Lithium targets are usually made of solid lithium with a metallic backing. Lithium is a difficult material to work with, especially for NRR. The melting point is low at 180.5 °C, limiting the amount of current and heat that can be applied to the target. Lithium is very quickly oxidized in air, and chemically reacts with many gases and with water, making it difficult to handle. While the neutron yield is useful for NRR, both in terms of flux at all angles and the favorable properties of the neutron energy spectrum, the gamma yield and difficult handling make lithium a poor choice as a neutron production target in a commercial NRR system. More focus has been placed on the D-D reaction for this study.

2.3.2.2   The D(d,n)^{3}He Reaction

The D(d,n)^{3}He reaction is advantageous for NRR in a number of ways. The D-D reaction produces a neutron through the capture of a deuteron but produces no photons in the reaction:

$$d + {}^2H \rightarrow n + {}^3He + 3.27 MeV$$
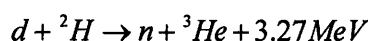
Eq. 2.7

This reaction is exothermic, which allows a lower energy deuteron to be used to produce neutrons in the required energy range, as there is no minimum energy threshold needed to drive the reaction. In addition to the lack of gamma rays, the D-D reaction produces neutrons with energies that vary based on the angle at which they are produced, similar to the p-Li reaction. Figure 2.8 shows the angular dependence of the D-D reaction. The

decrease in energy with angle is more rapid than the marginal decrement of energy with respect to angle for the p-Li reaction, as shown in Figure 2.9.
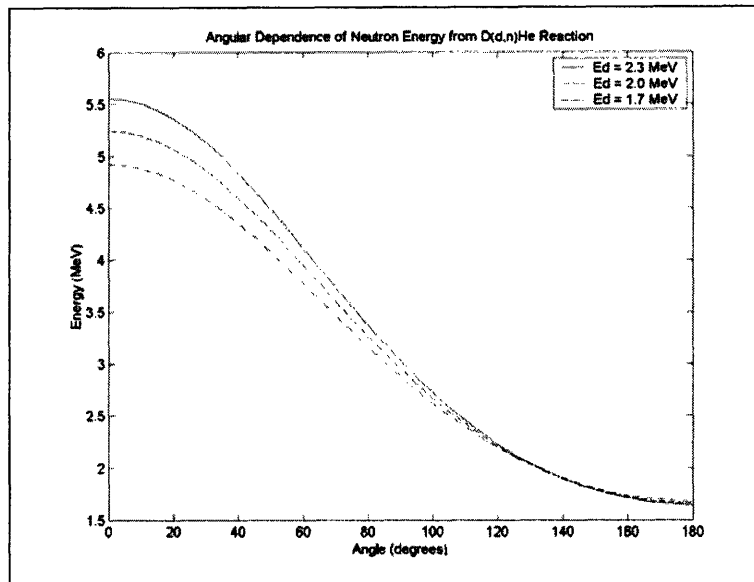
Figure 2.8: Neutron energy as a function of angle for the D-D reaction
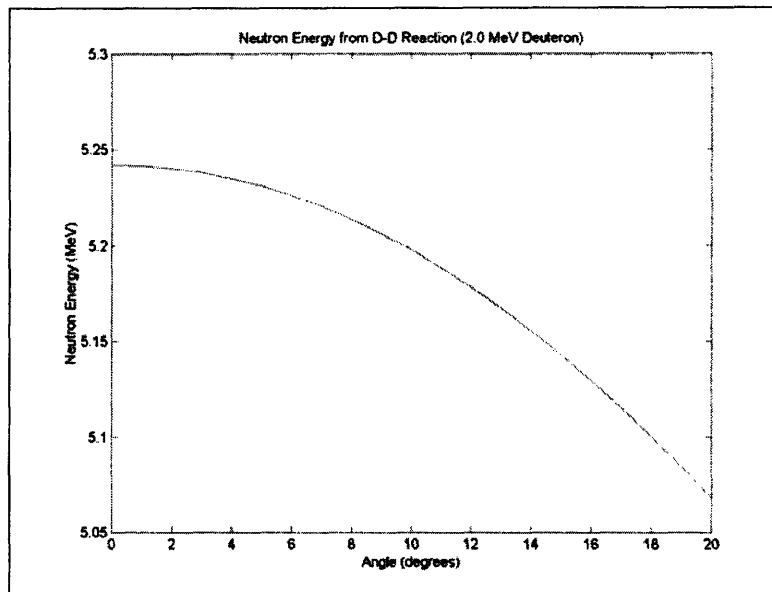
Figure 2.9: Neutron energy from D-D reaction at small angles

While a less steep decline in energy is desirable, the neutron energy over a 10° cone can still be considered monoenergetic for the purposes of NRR. The differential

cross-section also varies more with angle than is the case for the p-Li reaction (see Figure 2.10). The differential cross-section is forward peaked, producing a larger neutron flux in the forward direction than at other angles. This can complicate imaging requirements, as longer imaging times will be required to ensure adequate signal-to-noise at areas of low neutron flux.
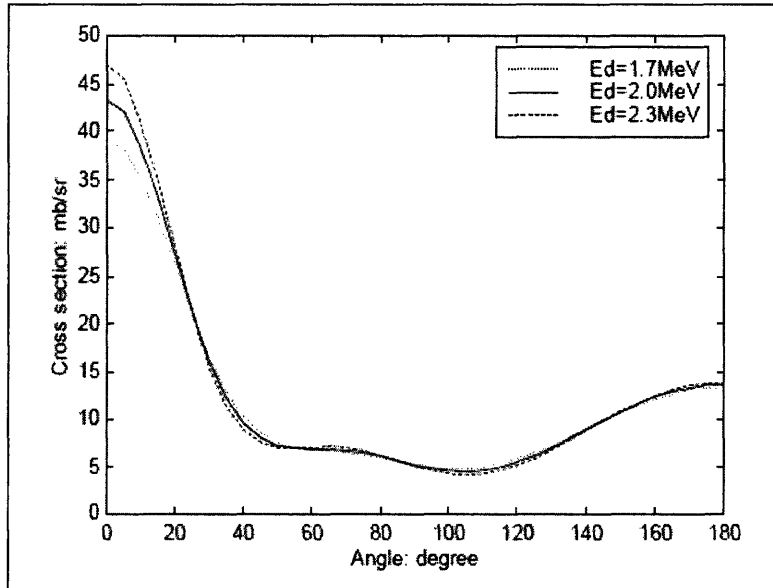
Figure 2.10: Differential cross-section for D-D reaction

Despite these few drawbacks, however, the deuterium reaction is convenient for use as a neutron production source for NRR. The neutrons produced by a relatively low energy deuteron (less than 3 MeV) span the entire range of desired neutron energies. Deuterium gas is readily available for use in a gas target, as it is much more easily handled than lithium. While the neutron energy decreases more rapidly with angle than is ideal, the energy spread is still adequate for NRR. There are no contaminating gamma rays inherent to the D-D reaction, and most importantly, the neutron flux obtainable from reasonable deuteron beam currents (on the order of tens of microamps) is large enough for the purposes of this study.

2.3.3 Target Designs

A great deal of time has been spent on the design of high-intensity, high-energy neutron sources that are compatible with accelerator systems. Accelerators produce high-energy charged particles such as protons and deuterons in a vacuum; these particles are then passed through a target material to create neutrons through nuclear reactions (see Section 2.3.2 for candidate nuclear reactions). The target designs used for neutron production have significant constraints placed on them by the interactions with the accelerated charged particle and with the accelerator vacuum system. For example, any charged particle loses energy as it passes through a material. The energy loss, and the resulting spread in particle energy, has a significant effect on the resulting neutron energy. Additionally, interaction of the charged particle with various materials can produce a significant amount of gamma rays, which negatively affects the images required for NRR. With regard to the accelerator vacuum, high intensity beams can cause heating in the target material which degrades the vacuum. These factors, as well as the neutron flux provided by the target and the ease of use and longevity of the target itself, must all be taken into account when choosing a neutron source target.

As discussed in the previous section, the $D(d,n)^3He$ reaction is the optimal source of neutrons for NRR and the majority of this section will focus on deuterium targets for neutron production. Deuterium targets for accelerator production of neutrons can be made either of solid metal-hydride or gaseous deuterium. Typical target designs for both these forms of deuterium are described in this section.

2.3.3.1 Solid Targets

Solid targets are generally easier to handle and less complex than gas targets, but their use is complicated by the fact that the neutron source is usually accompanied by a strong gamma field and contaminating, low-energy neutrons created from the slowing down of the charged particles in the solid target. Most solid targets based on the $D(d,n)^3He$ reaction are made of a metal-deuteride deposit. The deuterium is implanted into a thin layer of metal, usually titanium or zirconium, with a thick metal backing. The

backing is typically a metal with high conductivity that can be water or air cooled to dissipate heat from the energy loss in the solid target.

Neutron production from solid targets degrades over time in a number of ways, including offgassing of deuterium at high temperatures, deuterium depletion, target oxidation, and target carbonization. Offgassing of deuterium occurs when the target reaches temperatures of more than 250 °C for zirconium- and titanium-based targets and 450 °C for scandium, erbium, and other rare earth-based targets. With adequate external cooling, this effect constrains the maximum beam power to approximately 0.15 kW and 4 kW, respectively. However, even with this constraint, high neutron fluxes have been achieved [36, 37].

Previous experimental work on NRR has incorporated a solid lithium target to utilize the ^{7}Li(p,n)^{7}Be reaction for neutron production [27]. The advantages of the D(d,n)^{3}He reaction have already been enumerated, but it is worth noting that although solid targets are generally easier to handle than other types of targets (notably gas targets), the solid lithium target presents distinct disadvantages. Lithium oxidizes rapidly in air, and violently with water, limiting its use in a commercial setting where chilled water is used to cool the target and targets are changed often due to use.

2.3.3.2 "Windowed" Gas Targets

Windowed gas targets enclose some amount of target gas (for our purposes, deuterium) inside a small container through which charged particles are transmitted to produce neutrons. The "window" is generally a thin piece of metal no more than a few microns thick that separates the gas of the target from the vacuum of the accelerator beamline. The end of the gas cylinder is usually closed by a thick piece of metal as a beam stop or by a similar thin window to allow the remaining beam to pass through. Gas targets have the disadvantage of being more complicated than solid targets, especially when the fragility of the thin window is considered. However, gas targets have some advantages over solid targets, including a lower gamma background and ease of refilling and reuse.

The primary concern with the use of gas targets is the vulnerability of the thin window. All charged particles deposit energy in material that they pass through; more energy in material with a high atomic number. A trade-off exists in that refractory materials with good high temperature strength tend to also have high atomic numbers. The window must be able to withstand the energy deposited by the passage of charged particles; consequently, thin-windowed targets function best when used in applications where the beam intensity is low and the energy of the particles is high. The thermal and mechanical properties of material composing the thin window limit the amount of energy that can be deposited by the beam. Beam currents are thus limited for particles of a given energy, and the beams are usually expanded before contact with the window to reduce the power density. Common materials used for thin windows include tungsten, molybdenum, stainless steel, nickel, titanium, and Havar.

Window failure modes are typically through diffusion of the target gas at high temperatures and pinhole leaks, although catastrophic rupture of the foil can occur. Tests have shown that the failure point of thin windows of a given material depends on a number of factors, including beam current and energy, diameter of the beam spot (and hence the power density), thickness of the foil, power dissipation, and pressure of the gas cell. In addition to these factors, any nuclear interactions in the foil material that can create "off-energy" neutrons or gamma rays must also be taken into account when considering materials for thin windows. Strengthening of the thin window can be provided by the use of a supporting grid. Meadows et al, used a gold grid to support and cool a thin nickel window, allowing the window to sustain high beam currents and greater pressure in the gas cell than unsupported windows [38].

A second factor to consider when using gas targets is the slowing down properties of the window and the gas itself. A thicker window is generally stronger than a thinner window of the same material but will slow the beam particles down a significant amount. The particle beam loses in energy in the target gas as well as the window, leading to a corresponding spread in neutron energies. The lower the energy of the particle as it enters the gas, the more energy will be lost in the gas cell and the broader the neutron energy spread. Thus, for most applications using monoenergetic fast neutrons, including

this one, it is desirable to find a trade-off between window thickness and the resultant energy loss and the strength provided by a thicker window.

2.3.3.3   Windowless Gas Targets

Windowless gas targets are the most complex and difficult to use of the three types of targets described here. In an attempt to remedy the problems inherent to the windows of gas targets (particle energy loss, rupture of the foil, broad beam spots, and gamma and neutron background radiation), gas targets were developed in which the target gas is confined and separated from the accelerator beamline without the use of a solid target window [39, 40, 41]. By using vacuum pumping systems, the target gas can be confined to a small region at the end of the accelerator beamline. Alternatively, a plasma arc can be used to separate the target gas from the accelerator beamline vacuum. The use of multiple pumps to maintain vacuum in the beamline and pressure in the target means that the accelerated particle is not degraded in energy by passing through a window, and the beam spot can be small as there is no concern regarding energy deposition. Similarly, plasma arcs confine a small amount of gas but do not degrade the incoming particle beam in any way. Plasma arcs are generally used when high-yield targets are desired.

Both of these methods of creating windowless targets are difficult to use in practice, especially in a public setting such as an airport. They require a number of pumping systems and, for plasma arcs in particular, significant energy requirements. The systems themselves are often complicated and difficult to use over extended time periods.

In this work, the D-D reaction has been used exclusively for experiments involving NRR. Due to the high neutron flux required, the eventual high throughput and need for interchangeable targets, a deuterium gas target was identified as the most favorable target system. The design of a high intensity, high pressure deuterium gas target that can be easily and economically fabricated is discussed in Chapter 4.

Figure 2.11 shows the entire object-detector system and its orientation with regard to the neutron source. The object-detector distance and orientation is fixed, and this

system is rotated around the neutron source in order to take advantage of the neutron energy at each angle for radiographic imaging.
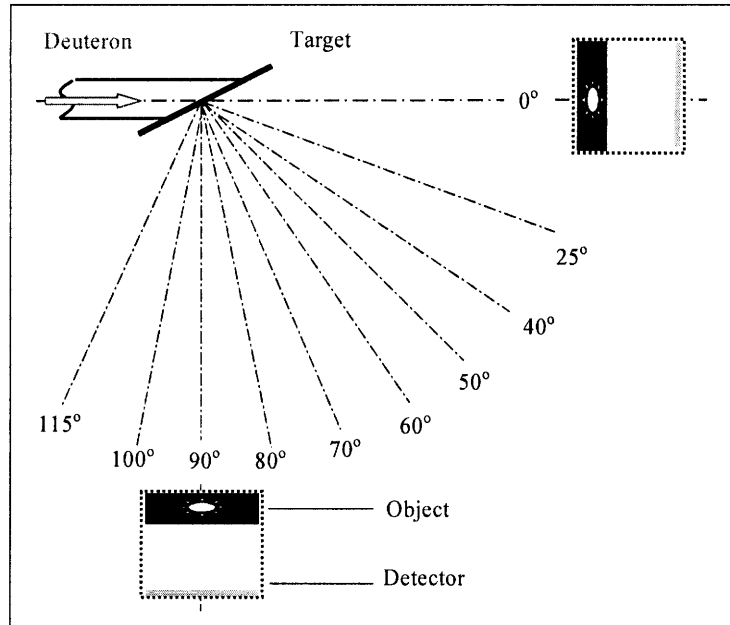
Figure 2.11: Rotational geometry of the object-detector pair [27]

2.4 Neutron Detection

One of the primary advantages of NRR for explosives detection is the ability to create an image of the object in question. This image provides a visual means of establishing the size and shape of a suspicious object, which is quite helpful in determining whether or not that object poses a threat. The means to quickly create images that are helpful to human screeners and to computerized detection algorithms is a significant concern in NRR. Images are produced by detecting the neutrons that pass through the object being scanned.

Neutrons are particularly difficult to detect, as they have long mean free paths in most materials, are uncharged, and all detection systems rely on the detection of radiation produced in secondary reactions rather than detection of the neutrons themselves. Common neutron detectors such as BF_3 counters are not applicable to NRR as they are not position sensitive and have relatively low efficiency for fast neutrons. Fast neutrons

are commonly detected using scintillating material, which is the means of detection utilized in this thesis. The light emitted from neutron interactions in the scintillating material is detected by a cooled CCD camera. The images formed by the CCD camera are subsequently analyzed to determine the elemental content of each item on a pixel-by-pixel basis.

2.4.1 Neutron Detection through Proton Interactions

Unlike charged particles, which are easily attenuated by heavy material, the unique properties of neutrons require low-Z material for moderation and detection. Neutrons interact most readily with hydrogen nuclei, although other light materials such as deuterium and helium can be used [42]. In this work, however, only hydrogen is considered, as materials containing significant amounts of hydrogen (such as plastics) are readily available and affordable as neutron detectors.

When a neutron elastically scatters off a hydrogen nucleus, a portion of its energy is transferred to the proton. The energy of the recoil proton is dependent on the scattering angle and is governed by simple, non-relativistic kinematics [43]:

$$E_p = E_n \cdot \cos^2 \theta$$

Eq. 2.8

where E_p is the energy of the recoil proton, E_n is the energy of the incoming neutron, and θ is the scattering angle; all quantities are measured in the laboratory coordinate system. For neutrons less than 10 MeV, the scattering process is isotropic in the center-of-mass frame. This property greatly simplifies the proton energy distribution to a simple rectangle over all scattering angles. The recoil proton can take on all energies between zero and the full energy of the neutron with an equal probability, meaning that on average, the neutron loses half of its energy to the recoil proton. If the neutron does not impart all its energy to the recoil proton, the neutron can undergo subsequent interactions with the scintillating material, losing more of its energy in the process. These additional interactions can degrade the image quality by causing increased light scattering and double counting of neutrons.

The energetic recoil proton excites the surrounding molecules in the scintillator; these molecules subsequently de-excite by emitting light. The distance that the recoil proton travels is short, much less than the dimensions of the scintillator, ensuring that all the proton energy is deposited in the scintillator. The amount of light emitted is proportional to the energy of the recoil proton rather than the initial incoming neutron [27]:

$$dL = \frac{3}{2} k \cdot E_p^{1/2} \cdot dE_p$$

Eq. 2.9

In this equation, dL is the amount of light emitted per fraction of energy lost, dE_p, k is a constant for any given material, and E_p is the energy of the recoil proton. According to Eq. 2.9, the maximum amount of light is emitted when the loss of energy is greatest. Therefore, most light is emitted from protons that absorb all the energy of the neutron and subsequently lose all that energy at once, while less light is emitted overall from neutrons that scatter multiple times. As the neutron can interact anywhere within the scintillator, it is important that the scintillator be transparent to its own light (or thin enough to allow light to be released) to allow for maximum light collection. It is also desirable that the scintillator material should translate most of the incoming energy into prompt fluorescence, or light emission within nanoseconds of excitation. Phosphorescence and delayed fluorescence, which have much longer response times, increase the random noise level in the detection system and degrade the quality of the image.

2.4.2 Types of Scintillating Material

Scintillating neutron detectors can be made out of organic material that contains significant amounts of hydrogen for neutron interactions. Scintillators that can be used for neutron detection for NRR applications would ideally have high interaction efficiencies, be transparent to their own light, and be inexpensive and easy to machine in large sizes. Preferably, they would be radiation-resistant, easy to handle, and have reasonable gamma-rejection characteristics. The scintillators that are of use for NRR can be made as solid plastic and liquid organic scintillators. Properties of a few common scintillators are shown in Table 2.1.

Table 2.1: Properties of common scintillators [43]

Scintillator Type*	H/C Ratio	Wavelength of emission (nm)	Refractive Index	Special Properties
BC-400/ EJ-212	1.103	423	1.58	General purpose solid plastic
BC-408/ EJ-200	1.104	425	1.58	General purpose solid plastic
EJ-209	1.25	424	1.57	Liquid scintillator for n/γ discrimination
ZnS(Ag)	n/a	450	2.36	Ag-doped ZnS in polycrystalline matrix for γ-blind n-detection

* Bicron (BC) and Eljen (EJ) are the two most common commercial distributors of scintillating material.

Solid plastic scintillators are extremely useful, as they are easy to shape into various forms, are easy to handle, and are inexpensive and robust. Solid plastic scintillators are made by dissolving organic scintillator in a solvent that can then be polymerized. Because they are easy to form, solid plastic scintillators are available in a wide range of sizes and shapes and have become the scintillator of choice for many particle detection situations, especially neutrons. Solid plastic scintillators can be shaped into flat sheets, rods, or fibers, depending on the application. The solute and solvent can be chosen to optimize the plastic scintillator for various applications. In addition to their usefulness as neutron detectors based on their physical properties, plastic scintillators are also very resistant to radiation damage and to heat, which leads to longer lifetimes of the material when used in high radiation fields.

Liquid organic scintillator is slightly more difficult to use as a detector than solid plastic, as the liquid itself is hazardous and care must be taken to ensure that it remains confined. Liquid scintillators are made by dissolving organic scintillator in a solvent material. The most common use of liquid scintillator is to count radioactive material that has been dissolved in the scintillator itself. However, liquid scintillator can be sealed into glass or plastic containers and used in the same way as solid scintillators. The light response of the scintillator to neutrons and gamma rays differs somewhat; liquid

scintillating material may be more useful in discriminating between the excitations of the two forms of radiation.

One type of solid scintillating material, ZnS, is especially useful for the discrimination of gamma rays from neutrons. This type of scintillator is made by dissolving equal parts ZnS in a polypropylene matrix. Neutrons interact with the large amount of hydrogen in the polypropylene, transferring energy to the protons in the matrix. These protons then transfer energy to the electrons in the zinc sulfide. The subsequent de-excitation of the electrons produces light. ZnS scintillators are generally doped with impurities, usually copper or silver, to shift the wavelength of the emitted light to visible wavelengths that can be detected by CCD cameras. ZnS scintillator doped with silver, ZnS(Ag), has been used in our study to shift the wavelength of the emitted light to 450 nm.

ZnS(Ag) scintillators have a variety of positive and negative attributes that make them simultaneously attractive and difficult for the use of NRR. The major difficulty when using ZnS(Ag) scintillator is that they are opaque to their own light. This opacity limits the thickness of the scintillator to no more than about 2-3 mm. This restriction reduces the overall number of neutrons that are detected to less than 5% of incident particles (depending on neutron energy). As an advantage, though, the thinness of the scintillator greatly reduces the detection of gamma rays. While detection rates for neutrons are in the low single-digits percentages, the detection of gamma rays in ZnS(Ag) is less than 10^{-4}%, which means that ZnS(Ag) scintillators can be considered gamma-blind. A second major advantage of ZnS(Ag) scintillators is that, unlike the isotropic light distribution of simple organic scintillators, ZnS(Ag) has been shown to be a Lambertian light source [28]. Consequently, a greater percentage of the emitted light is emitted in the forward direction to be detected by the CCD camera. ZnS(Ag) has also been shown to produce more highly resolved images with sharper edges than other solid scintillators. However, residual delayed-fluorescence effects remain on the ZnS screen which can be resolved up to 30 hours after irradiation, which could complicate imaging in extended-time scenarios.

2.4.3 Efficiency

The efficiency of proton recoil detectors is defined as the fraction of initial particle energy that is converted to usable visible light through interaction with the scintillator. Factors that negatively affect the efficiency of scintillation detectors include unwanted oxygen contamination, low neutron cross-sections in the energy range of interest, thin detectors, and the conversion of neutron energy to heat or another undetectable form of energy rather than to visible light. For plastic scintillators containing only hydrogen and carbon, the efficiency is given by:

$$\varepsilon = \frac{N_H \sigma_H}{N_H \sigma_H + N_C \sigma_C} \left\{ 1 - \exp\left[-\left(N_H \sigma_H + N_C \sigma_C \right) \cdot d \right] \right\}$$

Eq. 2.10

where N is the number density, σ is the neutron scattering cross-section, and d is the path length through the detector, and the subscripts H and C denote hydrogen and carbon, respectively. Eq. 2.10 does not take into account multiple neutron scatterings. The efficiency of typical plastic scintillator as a function of neutron energy is shown in Figure 2.12.
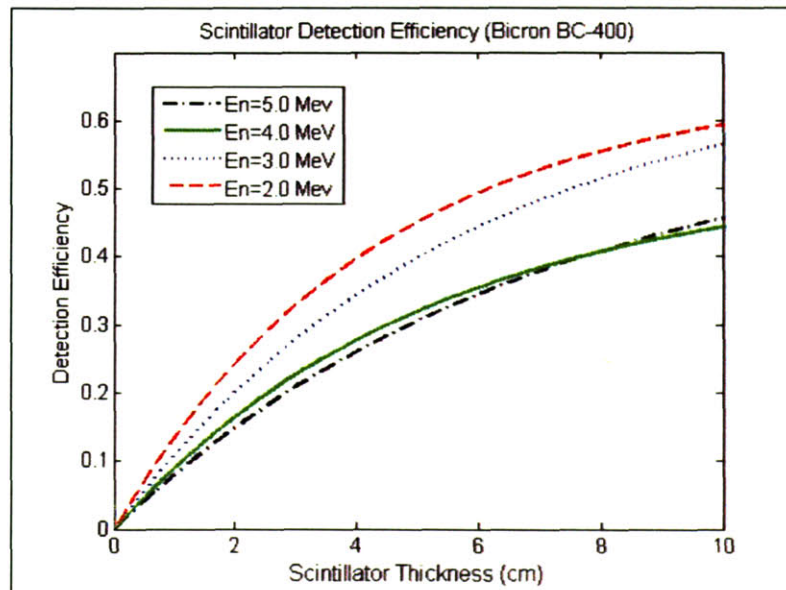
Figure 2.12: Efficiency of plastic scintillator (BC-400)

As Figure 2.12 demonstrates, the efficiency of plastic scintillator is fairly low, not more than 30% for reasonably thick detectors, and approaches an asymptotic limit with thickness of the scintillator. As discussed in the following section, the resolution of the detector depends on the thickness – as the scintillator becomes thicker, the light spread increases and the resolution decreases. For the purposes of NRR, the scintillation detector thickness should not exceed 4 cm.

2.4.4 Resolution

The spatial resolution of the scintillator determines the degree of detail that can be obtained by the neutron detection system. For some situations, extremely fine resolution is necessary; NRR, however, is capable of providing satisfactory images with resolution on the order of millimeters as explosives are larger than a few millimeters. The resolution of the scintillation detector depends on a variety of factors, among them the range of the recoil protons, multiple scattering of neutrons within the scintillator, the detector thickness, and the spread of light within the scintillator. The resolution of the overall system depends still further on the size of the neutron source, the optical system, and the resolution of the CCD camera, discussed in the following section. The resolution is measured using a point spread or line spread function, where the sharp edge of an object is shown as a gradual transition. The full width at half maximum (FWHM) of the line spread function is quoted as the resolution of the detection system.

The resolution intrinsic to the scintillator is a function of the amount of light that is created in and subsequently exits the scintillator. Neutrons interacting with the hydrogen in the scintillator to produce light are scattered in the process, often scattering at an angle to the initial direction. If these scattered neutrons subsequently interact with the scintillator a second (or multiple) times, light is also produced in these interactions. The light from these secondary interactions is indistinguishable from primary interactions and results in blurring of the image. Recoil protons also negatively affect image resolution. Recoil protons have a finite range in the scintillator, determined by the energy of the proton. The protons emit light as they travel along their path, causing transverse spreading of light. According to Eq. 2.9, more light is emitted from high-energy protons,

so as the proton slows down along its path, less light is emitted. This results in the light spread being much less than the actual range of the recoil protons, generally less than one millimeter for protons with energy less than 10 MeV.

The intrinsic spatial resolution of various scintillators was measured and recorded in previous work on NRR [27]. Resolution was measured using a 12 MeV neutron source placed four meters from the object with an image magnification of one. The resolution of the detector was measured at the center of the scintillator, directly in line with neutron source. The results are listed in Table 2.2.

Table 2.2: Spatial resolution of scintillators

Scintillator Type	FWHM (mm)
2 cm BC430	2.15
2 cm BC400	0.79
4 cm BC400	1.10
2.4 mm ZnS(Ag)	1.36

From this table, we can see that the resolution of the scintillator is reduced with thickness, due to the light spreading within the scintillator. Therefore, there is a trade-off between detector efficiency and resolution that must be optimized for specific applications. For NRR, the efficiency of the scintillator is paramount, as resolution on the order of a few millimeters is all that is required for adequate imaging of luggage. However, the low neutron flux and need for high signal to noise ratios requires high efficiency detectors.

2.5 Optics and Image Formation

The optical system for NRR consists of a scintillating material described in Section 2.4 to provide the visible light for detection, a mirror to deflect the light, a CCD camera to collect the light, and a lens to focus the light onto the camera. The image formed by the CCD camera is then analyzed to remove "dead" or defective pixels and saturated pixels caused by the unavoidable detection of cosmic rays. The final resolution

of the image, magnification, and quality of the image are due to the geometry of the entire system, including the neutron source, and the characteristics of the CCD camera. These systems and the image processing are described in this section.

2.5.1 Optical Geometry

Simple ray optics govern the optical characteristics of an NRR system. The main factors contributing to the final image are image magnification (M), and the source-to-object and source-to-detector distances, s_1 and s_2, respectively. These three interrelated quantities dictate the size of the image, the resolution requirements of the detector plane, and the number of unwanted scattered neutrons which are detected.

The magnification of the object is given by:

$$M = \frac{1 + s_2}{s_1}$$

<div align="right">Eq. 2.11</div>

Since the object is smaller than the image by a factor of $1/M$, it can sometimes be useful to maximize the object magnification in order to resolve small objects. For NRR, however, resolution is not the primary concern, and lower magnification factors are necessary in order to scan large objects.

The magnification, in conjunction with the size of the neutron source, also affects the resolution requirements of the detector. The resolution of the detector for a point source is given by:

$$R_d = R_0 * M$$

<div align="right">Eq. 2.12</div>

where R_d is the resolution in the detector if the size of the object is R_0. In this way, small objects can be seen even in detectors without excellent resolution. However, the physical size of the neutron source has a detrimental effect on resolution. In any practical application, the source is not a point source but has some finite size. The result is a shadow of the source on the detector that is $M-1$ times as large as the source. Eq. 2.12 can be modified to include this effect:

$$R_d = R_s(M-1) = R_s \cdot \frac{s2}{s1+s2}$$

<div align="right">Eq. 2.13</div>

Thus, the absolute maximum resolution of the detector is fixed by the size of the source and the distances from the source to the object and the object to the detector.

A primary concern in NRR is the number of neutrons that arrive at the detector but have actually been forward-scattered by the object. Since NRR is only concerned with detected neutrons that have been transmitted through the object, these neutrons which have been scattered actually degrade the contrast of the image and affect the calculated attenuation coefficients. To avoid this problem, the distance from the object to the detector can be fixed such that few scattered neutrons reach the detector.

Neutron intensity obeys the $1/r^2$ radiation law. Neutrons which are scattered by the object are affected by this law differently than those which are transmitted as the distance, or r, is different for each of these classes of neutrons. For the former, the intensity is

$$I_{transmitted} \sim \frac{1}{(s_1 + s_2)^2}$$

<div align="right">Eq. 2.14</div>

whereas those which are scattered decrease in intensity by

$$I_{scattered} \sim \frac{1}{s_2^2}$$

<div align="right">Eq. 2.15</div>

A plot of these two intensities as a function of s_2, keeping the total distance s_1+s_2 constant, shows that the number of scattered neutrons reaching the detector is minimized beyond a distance of half a meter between the object and the detector.

For this study, the detector screen was small – 25.4 cm x 21.4 cm. In order to view complete objects, the magnification was kept to 1, the source-to-object distance was kept at 1.5 m, and the object-to-detector distance was 0.5 m.

2.5.2 CCD Camera

CCD (charge-coupled device) cameras contain a silicon chip to record light that reaches the camera from the scintillator. The CCD silicon chips are divided into pixels, usually hundreds to thousands of pixels on each side of the chip, with the pixels themselves a few to tens of microns on each side. The light emitted from the proton interactions within the scintillator is detected by the CCD camera and converted to an electrical signal proportional to the number of photons received. The charge is created when a photon interacts with the silicon, exciting an electron. The excited electron moves from the valence band into the conduction band and is trapped, creating a charge. After a specified imaging time, the charge is read out and converted to a digital image. The charge capacity is dependent on the parameters of the individual CCD camera, but is usually around 100,000 electrons.

CCD cameras are sensitive to external light and to heat, so the camera must be placed in a dark enclosure and cooled to reduce the dark current and improve the signal to noise ratio (SNR). When used for NRR studies, the camera must be placed out of the neutron beam, as neutrons damage silicon chips. A mirror is placed to reflect the light from the scintillator to the camera. It is important that the mirror be matched to the wavelength of the light output of the scintillator.

The quality of CCD cameras is characterized by the resolution that can be achieved, the size of the image, the noise inherent to the system, and the quantum efficiency. The absolute resolution of a CCD camera is determined by the size of the individual pixel; for situations such as NRR where very high resolution images are not required, the pixels can be binned (the output of an area of pixels is combined into one value) to reduce computation time and file size without a significant degradation of resolution. The final image size is limited to the number of pixels on the CCD chip; for NRR, the larger the CCD camera, the better, as larger objects can be imaged at once. However, larger chips are difficult to make and disproportionately more expensive than smaller chips. These factors must be taken into account when choosing CCD cameras.

More important, to image quality, in our case, than pixel and chip size is noise and the quantum efficiency of the CCD. Noise is generated from dark current and from

readout charge. Dark current is due to thermal excitations of electrons in the silicon chip, according to the statistical distribution:

$$N \propto e^{\frac{-E_g}{2k_B T}}$$

Eq. 2.16

where N is the number of thermally excited electrons, E_g is the energy of the band gap between the conduction and valence band, T is the temperature, and k_B is Boltzmann's constant. From this equation, it is apparent that as the temperature decreases, the number of thermally excited electrons also decreases. CCD cameras are usually operated at very low temperatures to reduce the dark current. In general, the dark current is reduced a factor of two for every drop of ~6 degrees in temperature. While the dark current can be subtracted from the final image, the noise in the dark current (the square root of the dark current) cannot, so it is advantageous to reduce the temperature as low as possible for low-light imaging situations. The readout charge is generated from the transfer of accumulated charge to the digital readout, as well as from the electronics of the system. The readout noise occurs only once for each pixel; by binning the CCD "on chip", or reading out a combination of pixels instead of each individual pixel, the ratio of readout charge to signal can be reduced. Again, the readout charge can be removed from the final image, but the readout noise cannot.

The quantum efficiency of the CCD is the final aspect of CCD quality. Not every photon that reaches the CCD chip will be absorbed and excite an electron: some will be reflected and some will pass through without being detected. The ratio of the number of excited electrons to the number of incident photons is termed the quantum efficiency. This quantity is wavelength dependent. Most CCD chips are front-illuminated, with light entering from the front of the chip and exiting through the back if it is not detected. For an increased economic cost, back-illuminated chips are available and provide significantly higher quantum efficiency levels. The back surface of back-illuminated chips is coated with an anti-reflective coating, which reduces the number of "lost" photons.

2.5.3 Image Correction

The digital images created by CCD cameras are marred by a variety of defects in the CCD chip. CCD chips are often manufactured with some defects, usually seen as "dead" pixels, or individual pixels that have a reduced response to light. Additional defects can be caused by irradiation, as silicon is susceptible to damage by neutron irradiation. "Hot" pixels are those which have higher response than others. Hot pixels are usually caused by the interaction of cosmic rays with the silicon chip or stray neutrons that excite the silicon. Cosmic rays are incident on the earth at a rate of one per cm^2 per minute at sea level, so long exposure times will likely contain a number of unavoidable hot pixels due to cosmic ray interaction [44]. Partial or entire columns of bad pixels (either all dark or all hot) can result from pixel traps, or pixels that interfere with the charge transfer process. Finally, cluster defects can occur when a number of adjacent pixels are flawed.

Images that contain a large number of defects and cosmic ray interactions appear "sparkly". There are a number of ways to remove dead pixels due to defects and hot pixels caused by cosmic rays and lessen the sparkly effect that these lend to the final image. First, a map of known dead pixels can be made. Those pixels will be dead in every image, and the value can be replaced with the median value of the adjacent pixels (usually the eight pixels surrounding the dead pixel). A median filter can then be applied to the whole image. A median filter changes the value of pixel to the median of its neighbors in the same way described above. A median filter applied to the entire image will change the value of most pixels, sometimes eliminating fine structures. An improved median filter has been applied for the images in this thesis, in which only those pixels above or below a specified value are revalued. This process to remove only dead pixels and hot pixels preserves the structure and resolution of the images while reducing the number of defective pixels.

2.6   Previous Work Using NRR

Previous work has shown the validity of NRR for determination of the elemental composition of concealed objects [30]. NRR has been extensively modeled using Monte

Carlo transport methods. Modeling of NRR using Monte Carlo analysis has been used to show the feasibility of NRR for checked luggage. Monte Carlo analytic methods use transport theory to track individual particles as they pass through a material. The specialized Monte Carlo code "COG", developed at Lawrence Livermore National Laboratory (LLNL), was used for these simulations. COG provides high-resolution simulation of neutron, gamma ray, and electron transport through three-dimensional objects. COG is based on the more familiar Monte Carlo N-Particle (MCNP) methodology, but incorporates imaging simulation to provide a 2-dimensional representation of the simulated object and particle transport. Point-wise cross-sections are used for the various materials in the simulations and for the purposes of this simulation were derived from LLNL's ENDL cross-section database. Objects are simulated by defining three-dimensional geometric shapes of known elemental composition.

A "terrorist overnight bag" was used as the object under investigation in the COG NRR simulation, depicted below in Figure 2.13. The bag simulated was a thin rectangular aluminum case with dimensions 40 x 30 x 10 cm^3, covered in cloth with a wooden handle and metal clasps. Inside the bag, the "terrorist" was carrying a newspaper, book, small umbrella, a 100 g bag of sugar, a pen and pencil set, a small camera, a flat paper notebook, and an assortment of cotton, wool and nylon clothing. Hidden among these common items was an automatic pistol with extra ammunition clip, a 100 g stash of cocaine-HCl, a 4" pocketknife, and a 300 g block of plastic explosive (50/50 wt.% mix of RDX and PETN). The average density of the bag was approximately 0.5 g/cm^3, that of a densely packed piece of luggage.

.
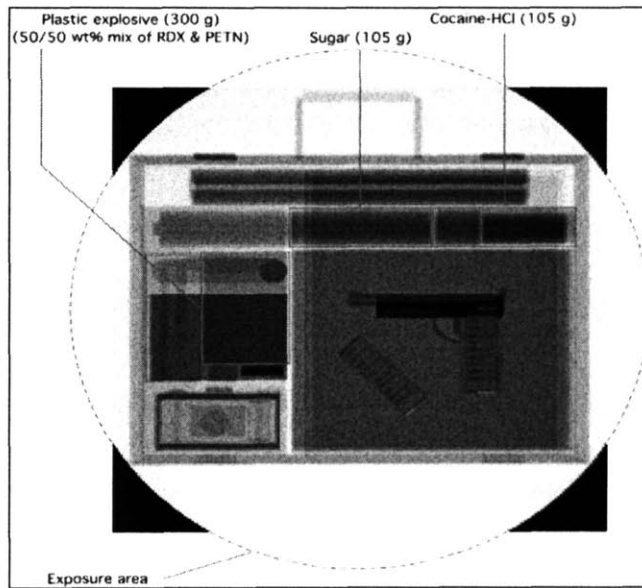
Figure 2.13: "Terrorist Overnight Bag"

The source-to-object distance for the simulation was 150cm while the object-to-detector distance was 50cm, providing a magnification of 1.33 and a viewing angle of ±10° from the center of the bag. The simulation was run using neutron energies corresponding to 0, 25, 40, 50, 60, 70, 80, 90, 100 and 115 degrees from the axis of a real D-D neutron source, or energies ranging from 5.55 MeV to 2.27 MeV. The neutrons transmitted through the bag without scattering off any of the internal components were "detected" and totaled to form a series of ten images, each corresponding to a neutron energy matching resonance features in the neutron cross-section. Only neutrons with the same energy as the incident neutron beam were counted in the final tally, as those with significantly less energy would likely be scattered neutrons. The simulations were run with 500,000,000 incident neutrons per energy. In addition to the neutron images, an image of the bag using 140 keV x-rays was also generated for comparison to the information supplied by the neutron simulations. These simulations are shown below in Figure 2.14.

63
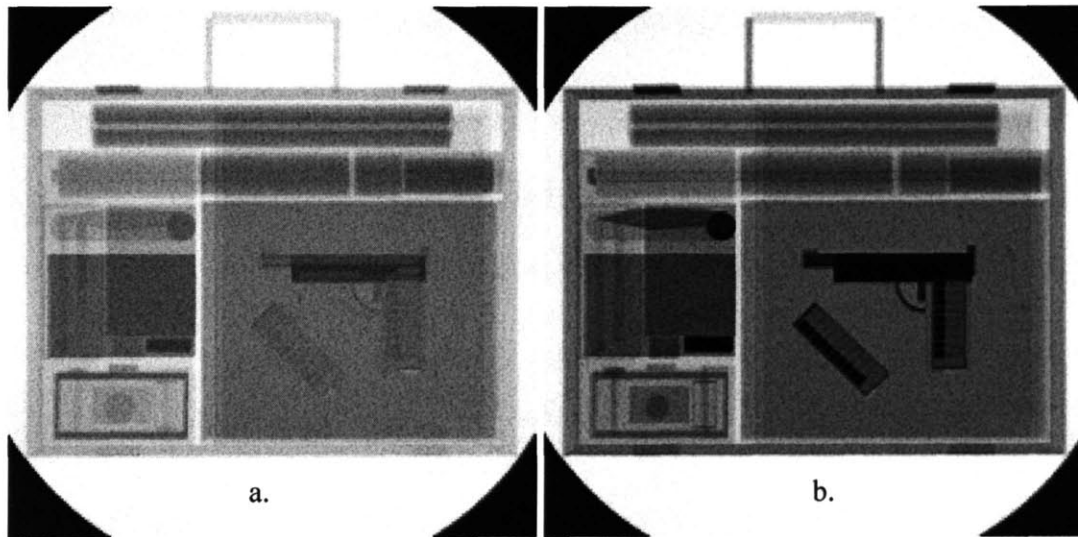
Figure 2.14: a) Neutron Image and b) X-Ray Image.

In Figure 2.14a, the luggage is seen as though imaged by 5.5 MeV neutrons, while in Figure 2.14b, the image is that of 140 keV x-rays. In both images, the darker areas are those where the beam has been attenuated to a great extent due to the high density properties of the metals in the x-ray image and the high cross-section values for the elements in question in the neutron image. In the x-ray image, the contrast between metallic objects such as the gun, the knife, the bullet tips, and the low-density items such as the sugar, drugs, books, and explosives is highly apparent, while it is less so in the neutron image. In neither image can the explosive be distinguished based on shape or density from the other items in the suitcase.

Using only x-rays for imaging purposes would force the screener to open this simulated bag to inspect all the items that appear to have the same low density. However, using NRR to further analyze this bag can distinguish the explosive from the other objects in the suitcase. While not shown here, the simulated images of the bag using neutrons at additional energies (or, equivalently, angles of 25, 40, 50, 60, 70, 80, 90, 100 and 115 degrees) can be used to solve the system of equations in Eq. 2.5. Using the known transmittance of each image simulated with COG, and the calculated attenuation coefficients for carbon, nitrogen, oxygen, hydrogen, and a fifth attenuation coefficient representing all other elements, the elemental distribution of these elements was

determined on a pixel-by-pixel basis. The results of the elemental mapping calculations are shown below.
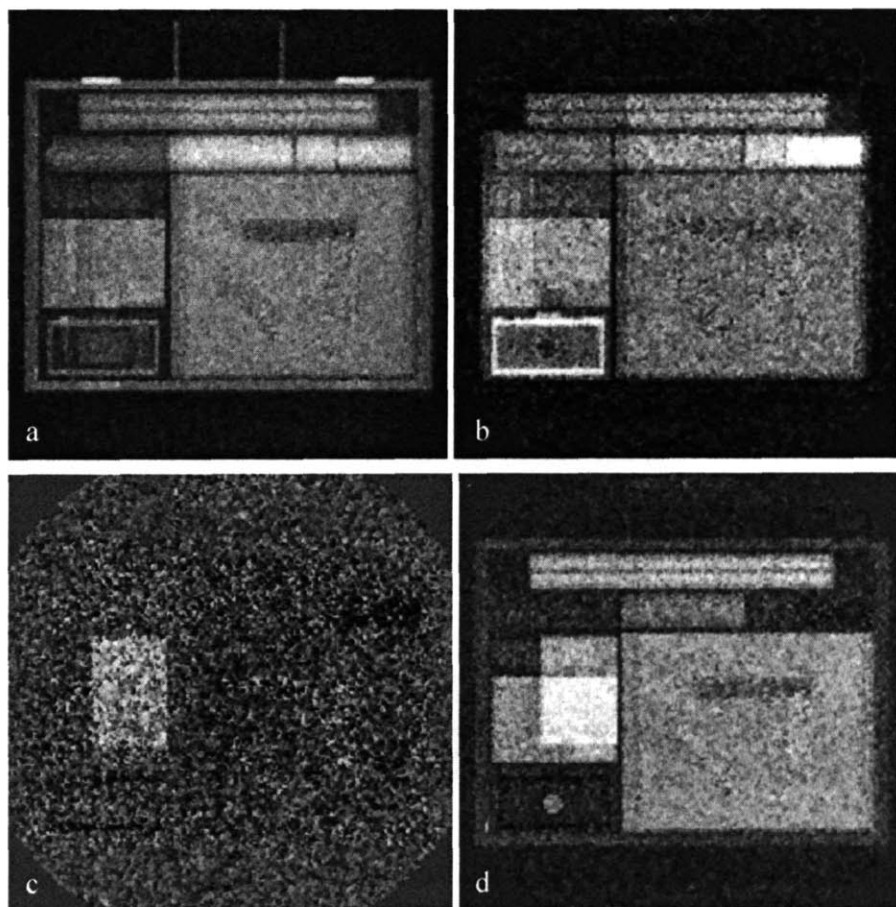
Figure 2.15: Elemental mapping of (from left to right, top to bottom) a. hydrogen, b. carbon, c. nitrogen, and d. oxygen

The images produced by analysis of the elemental distribution clearly show regions where the local HCNO content is high. Figure 2.15a and b shows that hydrogen and carbon are the predominant elements in most of the materials, especially in the sugar, the cocaine, and the books and clothing. Figure 2.15d, the elemental distribution of oxygen, shows the polystyrene handle of the umbrella, the silicon oxide camera lens, and the blocks of sugar and explosive with their high oxygen content. However, Figure 2.15d, the map of nitrogen, clearly shows the PETN and RDX mixture with its high

nitrogen content. Combined with the amount of oxygen present in the same area, this information allows one to distinguish this area of high nitrogen and oxygen content as explosive in nature, while characterizing the other items in the bag as non-explosive material.

2.7 Chapter Summary

This chapter has described the theoretical technique of single- and multiple-element NRR. The procedure for both methods is straightforward, utilizing the peaks and valleys of the neutron cross-section over high (1-6 MeV) energies. By exploiting these differences in the cross-section, the attenuation of the initial neutron beam in radiographic images taken at energies on- and off-resonance can be compared to determine the elemental composition of the items under scrutiny. The elemental composition in addition to the images themselves can bolster current explosives detection methods.

The components of a deployable NRR system include the neutron production system, the target and transport system, and the neutron detection and imaging system. For our purposes, an RFQ accelerator used to accelerate deuterons is employed, along with a high-pressure deuterium gas target, to provide a neutron beam that varies in energy with angle from 2 to 5.5 MeV. The transport system is designed to rotate the target object around the neutron source, stopping at designated angles (energies) to record a radiographic image. The neutron detection system consists of a scintillation detector coupled to a CCD camera for recording images.

Simulations were performed in previous work to prove the validity of NRR for explosives detection in airport situations. The simulations were completed at LLNL on the Monte Carlo computational program COG. A "terrorist overnight bag" was modeled. The simulated contents included densely packed clothing, sugar, books, cocaine, and an explosive mixture of 50/50wt% PETN and RDX. The simulations clearly demonstrate that NRR can be used to determine the elemental composition of objects and separate dangerous items such as explosives from other items commonly found in luggage.

Experimental and laboratory-scale testing is required to show that NRR can be applied in a practical situation.

3 Preliminary Experiments

The activities described in this thesis began with a set of experiments conducted at the Edwards Accelerator Laboratory at Ohio University (OU) in Athens, Ohio. These initial experiments demonstrated that multiple-element NRR can be performed on hidden, unknown objects, but that challenges remain. This chapter describes the experiments and results, following with a discussion of the obstacles encountered that the remainder of this thesis addresses.

3.1 Experimental Setup

The neutron source for the preliminary experiments consisted of a large tandem accelerator for the production of high-energy deuterons and a deuterium gas cell to make use of the D-D reaction. Ohio University's tandem linear accelerator was used to provide a beam of 2.5 MeV deuterons [45]. The OU accelerator facility is well suited to NRR: the accelerator is equipped with a beam swinger that can rotate the end of the accelerator beamline, including the gas cell, from horizontal with respect to the floor up to 158 degrees with 0.1 degree precision. The ability to rotate the deuterium gas cell allows the user to accurately choose neutrons of a desired energy by rotating the beamline to the corresponding angle (see Figure 2.8).

A plan view of the facility and an image of the accelerator are shown in Figure 3.1. The deuteron beam is produced by a Cs sputter source and directed through the high voltage terminal (the large orange tank) to the beam swinger by a series of bending magnets. This ensures that only deuterons of the correct energy are aimed at the gas target.
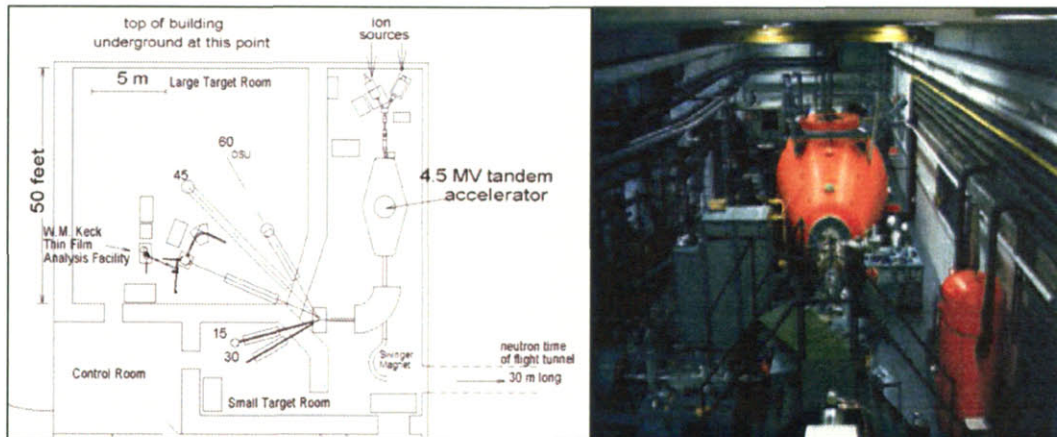
Figure 3.1: Tandem accelerator at the Edwards Accelerator Laboratory at Ohio University [45]

Once neutrons are produced, they are directed into a well-shielded, 30 meter long tunnel, ideal for neutron time-of-flight measurements or neutron/gamma discrimination. The tunnel is situated behind a 1.5 meter thick concrete wall with a circular opening lined with tapered polyethylene to shield off-energy neutrons from the time-of-flight facility. The accelerator facility incorporates other beamlines and target areas, but only the beam swinger and tunnel area were used for the NRR experiments, although time-of-flight measurements were not the purpose of the experiments.

The accelerator facility shown in Figure 3.1 is obviously much too large for applications in which space is a premium, such as NRR. Additionally, the limits on deuteron current at the Ohio facility have the effect of increasing the time required for NRR imaging. Despite these drawbacks, however, the ideal setup and availability of the Ohio machine provided sufficient neutrons for initial proof-of-principle experiments.

The deuterium gas cell itself was one centimeter in diameter and eight centimeters in length, pressurized to 3 atm with deuterium gas. The cell was separated from the accelerator beamline by a 5 μm thick tungsten window, and closed at the far end by a thick gold beamstop to stop any accelerated deuterons that did not interact with the deuterium gas. The fragility of unsupported 5 μm tungsten required that the beam current be kept relatively low to avoid destroying the foil; a constant, 5 μA beam of 2.5 MeV deuterons was used for all experiments.

A 4 cm thick Bicron plastic scintillator, BC-408, designed specifically for neutron detection, was used as the neutron detector and light source for the CCD camera. This scintillator has a hydrogen/carbon ratio of 1.104 and 64% of the light output of anthracene [46]. The light emitted from BC-408 is blue, with a mean wavelength of approximately 430 nm. The efficiency of the scintillator is governed by Eq. 2.10; the 4cm thick detector used had a maximum efficiency of 18%.

The CCD camera used was made by Princeton Instruments CCD array. The chip itself was 24.6 cm square, with 24 μm square pixels. Cooled using liquid nitrogen to 153 K (-120 °C) to reduce noise, the thermal noise generated was low: 2.5 electrons/pixel. The read noise was approximately 5 electrons/pixel. The quantum efficiency of the CCD was 0.5. While the noise inherent to the system is low, the signal from the neutrons is also small. To ensure sufficient signal, the chip was binned to 128 x 128 pixels with 192 μm square pixels and imaging times were on the order of 30 minutes.

The experimental setup is shown below in Figure 3.2. The object under inspection was located two meters from the neutron source, with the scintillator positioned three meters from the object. A mirror redirected light produced from interactions in the scintillator through a 45° angle onto a CCD camera imaging system. The camera was placed in a position behind the thick shielding wall to protect the camera from the harmful effects of stray neutrons. The scintillator, mirror, and CCD camera were enclosed within a light-tight box to eliminate environmental light effects.
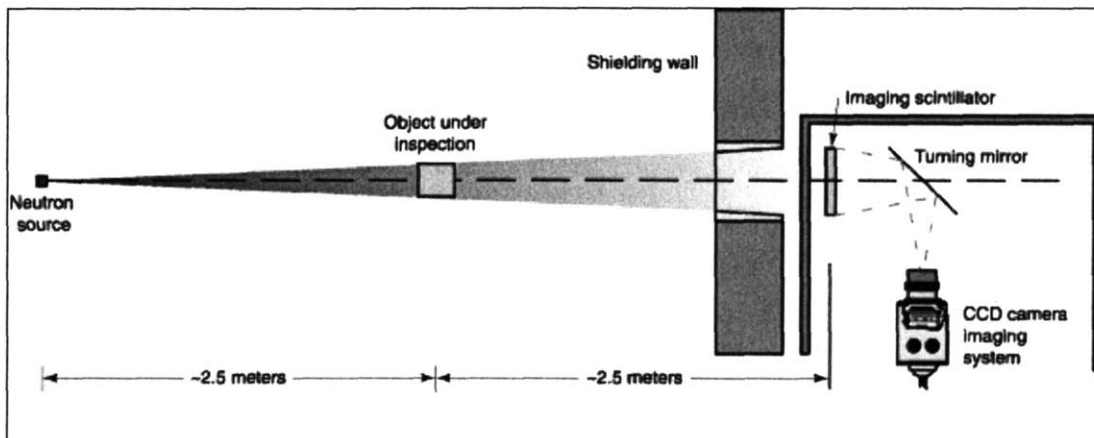
Figure 3.2: Experimental setup at Edwards Accelerator Laboratory [47]

After the radiographs were taken, an image correction algorithm was used to correct for defective pixels in the CCD array, stray effects from cosmic rays, and to smooth the image overall to improve the analysis. First, a map of the "dead" pixels (pixels that have either much less or much more signal than average) was made. The map of dead pixels is constant for all the radiographs. Once the locations of the defective pixels are known, the defects are removed by replacing the dead pixel with the median value of the eight surrounding pixels.

After the dead pixels have been corrected, a simple median filter is applied to the edges of the image. For each edge pixel, the following procedure is used: First, the value of the two pixels on either side of the edge pixel in question (still along the edge) is determined to be within a pre-determined value (usually within three standard deviations of the mean). If the pixel is not within the limits, it is excluded. Second, the median of the "good" pixels is found, not including any of the excluded pixels. Finally, the initial middle pixel in question is replaced with the median. This ensures that the edges of the image are "good", i.e., that any aberrant pixel values have been replaced with median values. For the corners of the image, the same procedure applies, except that one or two of the neighboring pixels used are those on the neighboring edge, rather than the same edge.

The remainder of the image is processed in a similar way. Starting in the upper left corner, the pixel in position (2,2) is evaluated. Five of the surrounding pixels, the edge pixels, have already been determined to be "good". The median and standard deviation of the value of these good pixels is found, and the remaining three neighboring pixels are compared to this value. If the value of the neighboring pixels is within a pre-set limit (approximately three standard deviations), it is kept as "good"; if not, it is rejected. The median of the remaining "good" pixels, combined with the additional edge pixels, is found, and the middle pixel is compared to this value. Again, if the value is within three standard deviations of the median, the pixel remains unchanged; if it is outside the limit, it is replaced with median value of its "good" neighbors. This process is repeated for all the pixels in the image. It is then repeated for the entire image three more times, starting in each corner of the image. The average of the four corrected

images is considered to be the final corrected image. This method is considered to be a modified median filter – it preserves the fine structure and resolution of the initial raw image by leaving those pixels that are not anomalous unchanged, but replaces outlier pixels with median values. This both improves the quality of the image and prevents important artifacts and overall values from over-correction.

3.2 Calibrations

Four calibration materials were used to determine the attenuation coefficients ($A_{i,j}$ in Eq. 2.5) for each element (carbon, oxygen, nitrogen, and hydrogen) at a series of angles. The calibration materials used were pure graphite, polyethylene block, water, and melamine for carbon, hydrogen, oxygen, and nitrogen, respectively. The attenuation coefficients calculated for carbon were subsequently used to determine the coefficients for hydrogen, which was used to determine the values for oxygen, and finally all three were used to determine the coefficients for nitrogen. A brief summary of the calibration objects is given in Table 3.1.

Table 3.1: Properties of calibration objects

Calibration Material	Density (g/cm^3)	Hydrogen (weight %)*	Carbon (weight %)	Oxygen (weight %)	Nitrogen (weight %)
Carbon (C)	1.745	0	100	0	0
Polyethylene (CH_2)	0.931	14.37	85.63	0	0
Water (H_2O)	1.00	11.19	0	88.81	0
Melamine ($C_3H_6N_6$)	1.116	4.80	28.57	0	66.64

*Percentages may not add to 100 due to rounding

The angles used were 0°, 25°, 46.5°, 53°, 63.5°, 70°, 80.5°, 84.5°, 91.5°, 112°, corresponding to average neutron energies of 5.13, 4.87, 4.31, 4.11, 3.76, 3.55, 3.21, 3.08, 2.88, and 2.36 MeV. The "average" neutron energy used here is due to the broadening in the energy of the accelerated deuteron. This broadening occurs due to the slowing down effects of the deuterium gas cell, meaning that deuterons that interact with the gas at the entrance of the cell will produce faster neutrons than those that interact with

the gas at the end of the cell, leading to an approximately 500 keV broadening of the neutron energy spectrum for a given angle.

Determining the attenuation coefficients followed the following procedure. For each angle (neutron energy), an "open beam" radiograph was taken with no obstruction of the beam, followed by a second radiograph of the calibration object (first of carbon). Following Eq. 2.2, the attenuation coefficient, or μ, is determined, from the following equation (for each pixel):

$$\mu = -\frac{\rho \cdot \ln\left(I/I_0\right)}{x}$$

Eq. 3.1

where I is the intensity of the radiographed object, I_0 the intensity of the open beam, ρ is the density of the object in g/cm^3, and x is the thickness of the object in cm. This procedure is followed for the other objects. Since the all the calibration objects save for carbon are compounds, the "attenuation coefficient" determined from this process is the attenuation for the entire material, not the individual element. The attenuation coefficient for each element is found by using the known percentages of the elemental composition of the calibration objects and the value of the attenuation coefficients already found, beginning with carbon.

3.3 "Unknown" Objects

Nine objects were placed in the beam as experimental test objects: ammonium nitrate, water, acetone, methanol, melamine, toluene, sugar, and a polyethylene block. These items were used because of their known compositions, enabling us to compare the experimental values for elemental content to the actual, known values. The materials were held in small, thin-walled, high-density polyethylene bottles. A representative image of the sample objects is shown below, followed by a table of properties.
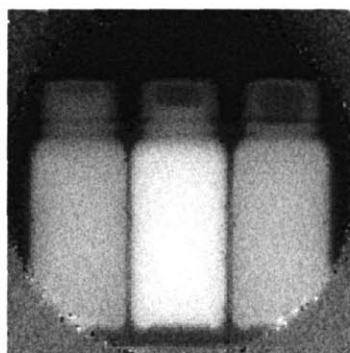
Figure 3.3: Sample image of experimental objects used for preliminary experiments
(from left to right: ammonium nitrate, water, and acetone)

Table 3.2: Properties of "unknown" objects

"Unknown" Material	Density (g/cm^3)	Hydrogen (areal density) [g/cm^2]	Carbon (areal density) [g/cm^2]	Oxygen (areal density) [g/cm^2]	Nitrogen (areal density) [g/cm^2]
Water (H_2O)	1.00	0.638	0.161*	4.850	0
Acetone (CHC_3COCH_3)	0.783	0.472	2.815	1.178	0
Polyethylene Block (CH_2)	0.9686	0.707	4.213	0	0
Toluene ($C_6H_5CH_3$)	0.8531	0.435	4.412	0	0
Sugar ($C_{12}H_{22}O_{11}$)	1.002	0.382	2.465	2.813	0
Ammonium Nitrate (NH_4NO_3)	1.0931	0.328	0.161*	3.580	2.089
Melamine ($C_3H_6N_6$)	1.109	0.317	1.892	0	4.036
Methanol (CH_3OH)	0.7799	0.563	1.758	2.127	0

* The slight amount of carbon is due to the thickness of the high-density polyethylene bottle used as a container. This amount is taken into account when calculating the areal density from the image intensity.

The procedure for determining the elemental composition of the "unknown" objects was similar to that of the calibration objects. First, an "open beam" radiograph was taken, followed by a radiograph of the object in question, at each angle. A "dark" image, or an image with no beam was taken as a background calibration. The images were despeckled using the modified median filter described previously, the background image was subtracted from the open beam image and the object radiograph, and each

pixel in the object image was divided by the corresponding pixel in the open image. The elemental content of each pixel was determined by solving a non-negative least-square fitting function for the equations of Eq. 2.5, using the measured mass attenuation coefficients from the calibration objects for $A_{i,j}$ and the measured intensity of the pixel, B_i.

3.4 Results

The attenuation coefficients were determined from these images and compared to the theoretical values derived from both MCNP and simple analytical methods. These values are shown in Figure 3.4. The colored symbols are the data from four different Monte Carlo simulations, while the black symbols are the experimental results from the calibration materials. It is interesting to note that all the simulations give quite similar values – in most cases, within 0.5% of each other. This uniformity only serves to highlight the difference in attenuation coefficients between the expected values and the actual values calculated from experimental measurements. In all cases, the values of the measured attenuation coefficients are significantly less than the theoretical values.

Further, the variation in attenuation coefficients due to the peaks and valleys in the cross-section is not well defined in the experimental values. Finally, the values derived from the experiment for the attenuation coefficients for hydrogen show a significantly different trend than the theoretical values: instead of decreasing with energy, the attenuation coefficients actually increased. These anomalies, especially the lack of variation in the attenuation coefficients at the various neutron energies, make it difficult, if not impossible, to accurately determine the elemental content of concealed objects.
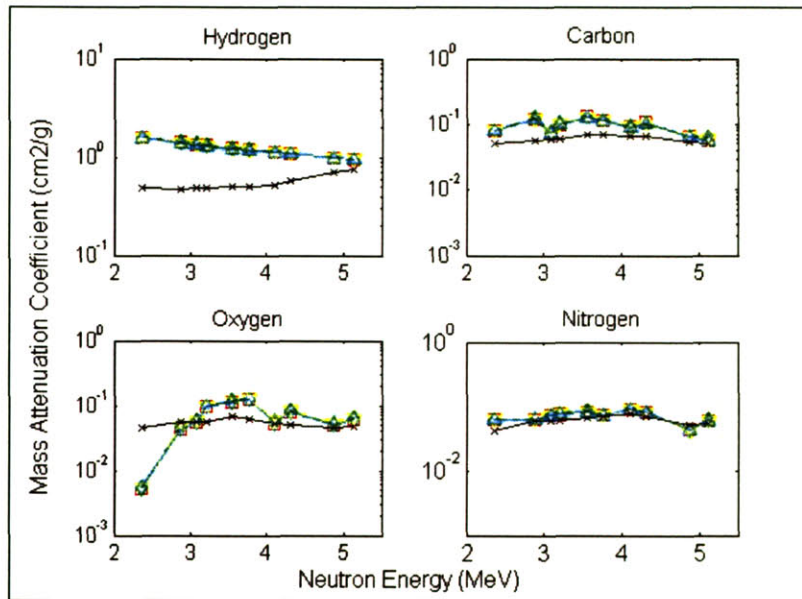
Figure 3.4: Theoretical and experimental values for attenuation coefficients for (a) hydrogen, (b) carbon, (c) oxygen, and (d) nitrogen. The colored symbols and lines correspond to results from simulations, while the black symbols and lines are the results of the experimental analysis. Note the different scale between hydrogen and the other elements.

The attenuation coefficients shown above were used to determine the elemental content of the sample objects using a non-negative least squares algorithm. The qualitative results for all the materials are shown in Figure 3.5a-c, showing, from left to right, relative hydrogen, carbon, nitrogen, and oxygen content. The greater the intensity of the image, the more of the particular element is present (the intensity scale is not matched between images).
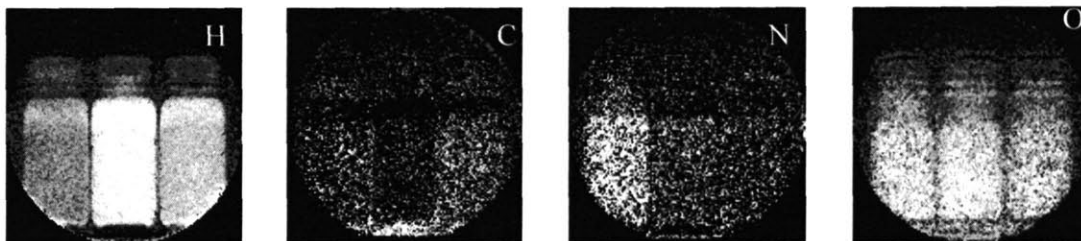
Figure 3.5: Experimentally-derived elemental content for ammonium nitrate, water, and acetone.
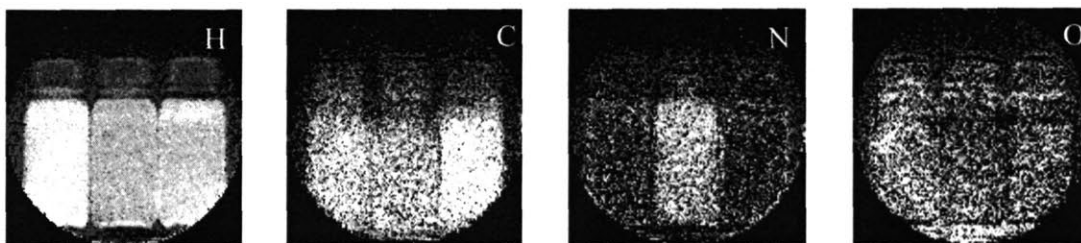
Figure 3.5b: Experimentally-derived elemental content for methanol, melamine, and toluene.
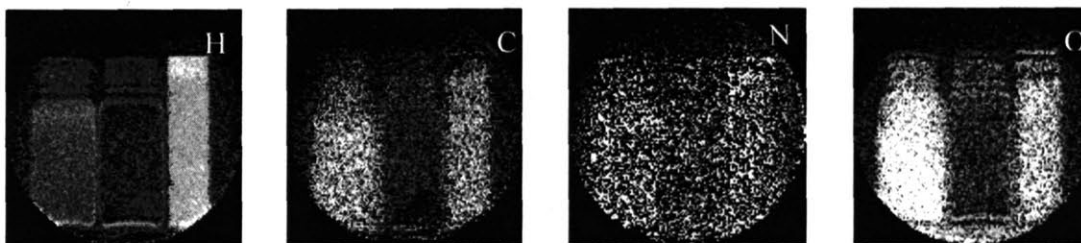
Figure 3.5c: Experimentally-derived elemental content for sugar, an empty bottle, and poly block.

The images in Figure 3.5 demonstrate that a difference in elemental content is quite visible between the different materials tested. For example, in Figure 3.5a, the high hydrogen content of the water is clearly visible, as is the case for the nitrogen content of melamine. These qualitative differences are a first step towards the successful implementation of multiple-element NRR for elemental discrimination. However, the *quantitative* results for the elemental components of the sample materials are not nearly as apparently accurate as the qualitative images shown in Figure 3.5. The numerical values for the elemental areal density – whether hydrogen, oxygen, nitrogen, or carbon – do not correspond well to the theoretical values. This is likely due to the fact that the values for the attenuation coefficients shown in Figure 3.4 are so different from the theoretical values. While there is enough variation in the experimental values to show

qualitative differences in elemental content in images, the numerical values are inadequate for elemental discrimination of the sort that this technique requires for explosive detection.

3.5   Analysis and Future Work

The experiments undertaken at Ohio represent a first step towards the application of NRR beyond simulations. These experiments were designed to test the effectiveness of NRR in determining elemental composition in a laboratory setting; as such, the geometry was simple (two-dimensional instead of three-dimensional setup to reduce any confusing effects from overlapping objects) and the materials chosen consisted only of known amounts of hydrogen, carbon, oxygen, and nitrogen.

The results of the preliminary experiments were both encouraging and provided direction for future experiments. The radiographs of the objects were clear and highly resolved, a requirement for the detection of explosives in checked luggage. Variation in elemental content was clear, as shown in Figure 3.5, but we were unable to determine the absolute amount of each element in the materials studied. This is a significant problem, as positive identification of explosives relies on the ability to determine the amount of each element present, not the differences in elemental content. However, the ability to show qualitative variation in elemental composition was nonetheless encouraging, and the inability to determine absolute elemental composition is likely due to lack of variation in the attenuation coefficients calculated from the calibration materials (Figure 3.4).

Solving the discrepancy between the theoretical values and those measured from the experimental data became the subject of significant study. Further analysis of the results of the preliminary experiments led to the conclusion that detrimental effects of gamma rays were the primary cause of the disagreement between expected and observed values. Although the D-D reaction used to generate neutrons produces no gamma rays, deuteron interactions in the gas target and accelerator components and neutron interactions in the shielding material are significant sources of gamma rays. The magnitude of the gamma ray problem was not recognized through the simulations described in Section 2.6, which did not include gamma ray calculations.

Gamma rays transfer their energy to the electrons present in the scintillating material while neutrons interact with the protons. Both these process emit visible light, which cannot be distinguished simply based on intensity or wavelength. Many scintillators have both a higher efficiency for detection of gamma rays than neutrons and produce approximately an order of magnitude more light when excited by a gamma ray rather than a neutron, as shown in Figure 3.6. The combination of more light produced per gamma than per neutron, as well as the higher efficiency for detection of gammas than neutrons means that the light detected by the CCD camera is more likely to be the result of gamma interactions with the scintillator than neutrons.
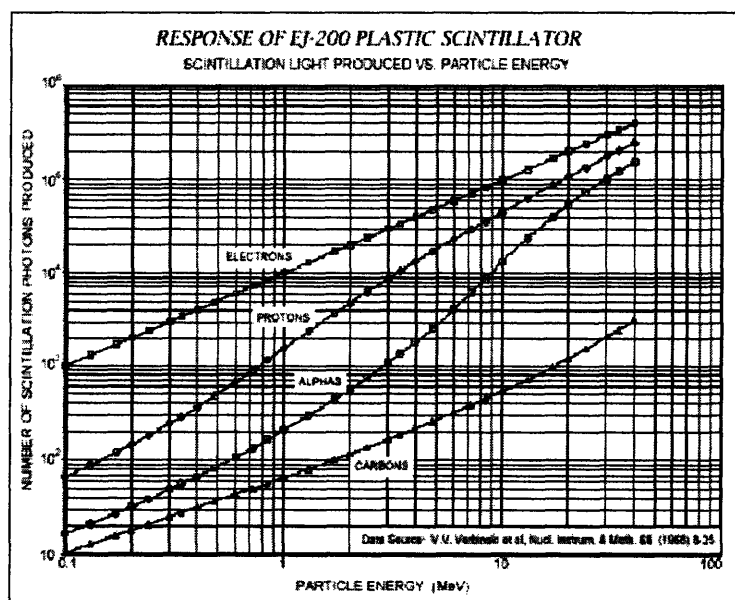
Figure 3.6: Light output of plastic scintillator (EJ-200 from Eljen Technology)

The gamma rays produced by the accelerator and gas target system were measured to determine their energy and number using the time-of-flight tunnel. The gas target was prepared in the same way as for the imaging experiments, with 3 atm of deuterium. The 2.5 MeV deuterons produced the required neutrons, and the neutrons and gamma rays were detected based on their relative arrival times at the end of the 30 meter tunnel. Bicron BC-213 liquid scintillator was used to detect the particles, while a NaI detector was used to measure the gamma spectra. The use of a NaI detector leads to a lack of resolution in the gamma spectra, but the spectra clearly shows a cluster of

medium-energy (400-700 keV) gamma rays with a high-energy tail extending to over 6 MeV (Figure 3.7).
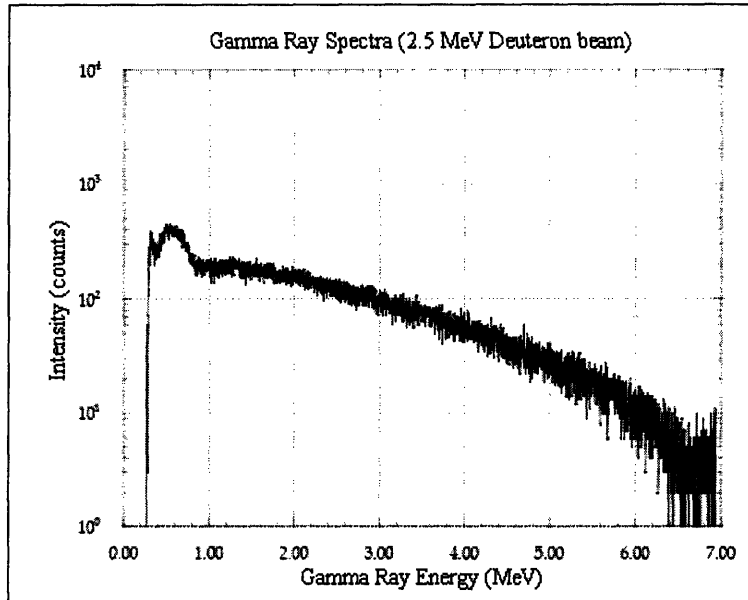
Figure 3.7: Gamma ray spectra from 2.5 MeV deuteron beam

The relative number of gamma rays versus neutrons is shown in Figure 3.8, gamma rays shown in black and neutrons in red. This chart shows both the spread in neutron energy and the large number of gamma rays that are produced in the accelerator and gas target system.
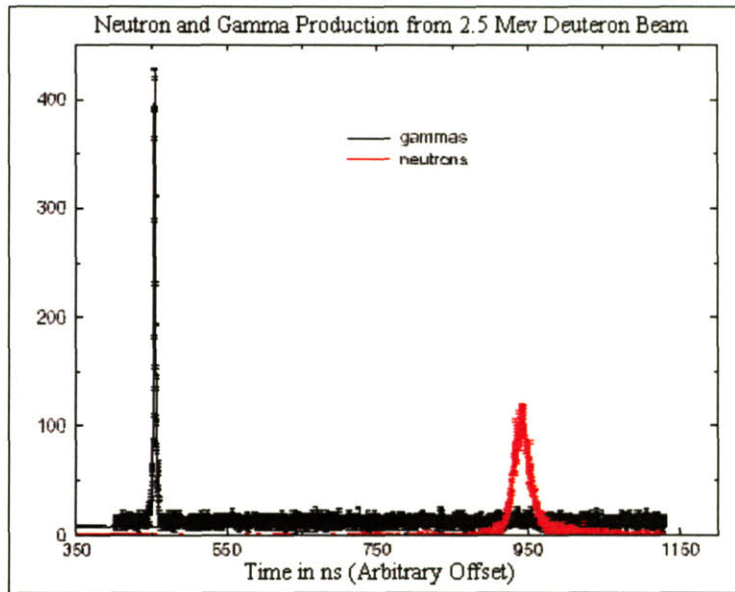
Figure 3.8: Relative gamma and neutron production

The light produced from gamma interactions, as opposed to the desired light from neutron interactions, contributes significantly to the intensity recorded by the CCD camera, artificially lowering the attenuation that the images depict. In other words, instead of measuring pure neutron attenuation, the images of the objects in Figure 3.5 actually show a combination of neutron and gamma attenuation. As gamma rays interact more readily and produce more light per gamma in the scintillator than do neutrons, the "attenuation coefficients" measured are more likely to be due to effects of gammas than of neutrons. This can explain the relatively featureless attenuation coefficients in Figure 3.4, as well as the overall value that varies little with element or energy. Further exacerbating this problem is the use of previously calculated attenuation coefficients in subsequent computations, carrying over any incorrect values to the attenuation coefficients for the next elemental calibration. Correcting this problem and working towards the development of a multiple-element NRR system is the primary goal of this thesis.

4   Gas Target

The gas target is perhaps the most important and complex element in the neutron resonance radiography system. As discussed in Section 2.3, neutron production occurs by accelerating an ion into a target material. The nuclear reaction that occurs produces fast neutrons with an angle-dependent energy spectrum. NRR requires neutrons with very specific properties, and the target for neutron production must be able to withstand long hours of use without significant maintenance. The $D(d,n)^3He$ reaction has been chosen as ideal for NRR, due to the properties described in Section 2.3.2.2; namely, the energy-angle dependence, the high neutron energy, and the straightforward use of gas targets for neutron production. A novel gas target design was developed to provide the neutrons required for NRR. The development and characteristics of the D_2 gas target are described in this chapter.

In order to produce sufficient numbers of neutrons for use in NRR, the deuteron beam current must be at least a few tens of microamps, the pressure in the gas cell must be on the order of 3-4 atmospheres, and the overall energy spread of the resulting neutrons should be less than 500 keV. These requirements ensure that the imaging time is minimized without sacrificing signal-to-noise, and generates a mono-energetic neutron beam at all required energies. Additionally, the target should be composed of materials that produce a minimum number of gamma rays in deuterium reactions to avoid contaminating the resultant neutron images.

While these are essential requirements for the development of NRR, they also cause difficulties in the design of the gas target that must be addressed. High beam currents cause excessive heating in the gas target window – usually a thin metal foil – that separates the deuterium gas from the vacuum system of the accelerator. Heating of the foil results in a decrease in the structural integrity of the window, which can cause the gas cell to fail. The high pressure of the deuterium gas filling the gas target cell further weakens the foil: the pressure difference between the gas cell and the vacuum system results in significant stresses on the foil window regardless of beam current. Increasing the thickness of the foil window would lead to increased structural capability but would

result in an unwanted larger spread of neutron energies by further slowing down the deuterium beam. This chapter describes the development of a novel gas target which addresses these concerns by incorporating a strongback, or strengthening mesh, between the thin foil window of the gas target and the vacuum system to promote robustness and a cooling apparatus to reduce heating in the target. The gas target is also explicitly designed to reduce gamma ray production by incorporating a gas, rather than metal, beam stop and the use of metals that have been shown to produce few gamma rays.

4.1 MIT LABA Tandem Accelerator

The accelerator used to develop and characterize the gas target is located at the Massachusetts Institute of Technology in Cambridge, MA. The availability of the accelerator was the primary factor for its use. This machine was able to provide a continuous beam of deuterons for neutron production, but was plagued by problems inherent to its design that make this type of accelerator a poor choice for large-scale work. Future work using NRR and any deployed system will undoubtedly use an RFQ accelerator as the optimal accelerator system.

The Laboratory for Accelerator Beam Applications (LABA) accelerator is a tandem accelerator based on Cockcroft-Walton tandem acceleration principles (described in Section2.3.1.1), built by Newton Scientific Instruments and shown in Figure 4.1. The accelerator itself is 3.9 m long, 0.94 m wide at its widest point, and 1.6 m high at the center. The compact size of this accelerator means that it can be safely operated in the basement of a building at MIT. Only a brief overview of the accelerator and the beam characteristics will be given here; full descriptions of the ion source, voltage generator, and characterization can be found in [48, 49].
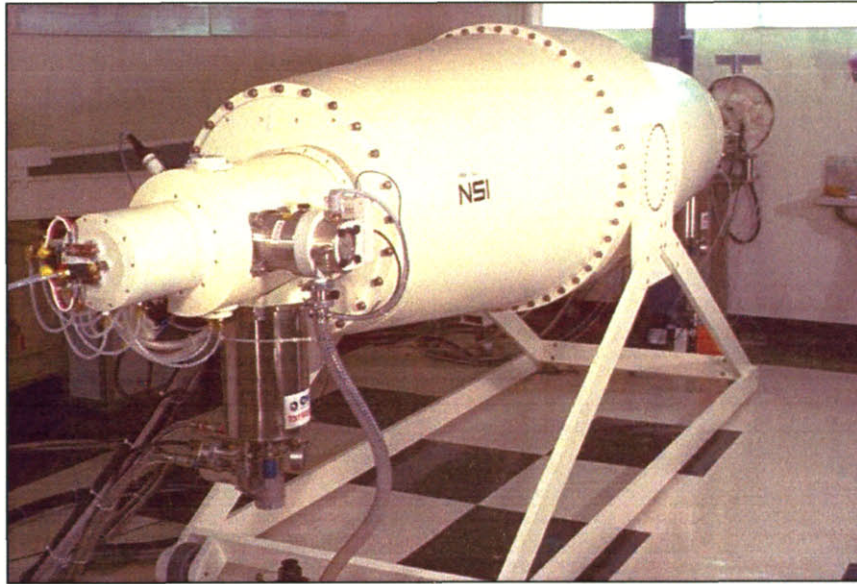
Figure 4.1: MIT LABA tandem accelerator

The LABA tandem accelerator was designed to accelerate a beam of charged particles up to an energy of 4.1 MeV and a current of 4mA. Practically, however, the accelerator was unable to produce deuterons with both high energy *and* high current; we were limited to using 2.6 MeV deuterons and beam currents of a few tens of microamps.

As described in Section 2.3.1.1, electrostatic linear accelerators generate a beam of charged particles through the use of a high-voltage generator. Tandem accelerators, such as the MIT LABA accelerator, have more than one acceleration stage. The LABA accelerator is a two-stage tandem, with the high-voltage terminal placed in the center of the accelerating tube. Two-stage tandem machines are able to produce charged particles with an energy twice that of the terminal voltage by a three stage process. Negatively charged ions are first accelerated up to a kinetic energy of qV_0, where q is the charge of the ion and V_0 the terminal voltage. Second, the electrons are removed, leaving a positively charged ion, and, finally, the positive ion is subjected to the same terminal voltage and accelerated away from the terminal, exiting the accelerator with a final kinetic energy of $2qV_0$.

Negatively charged deuterium ions are produced in the LABA accelerator in the ion source, the first stage of the acceleration process. Within the ion source is a solid tungsten filament, a plasma chamber, and an extraction electrode. High-purity deuterium

gas is passed through the plasma chamber while a high current is passed through the tungsten filament. When the filament reaches 2250 °C, electrons are expelled from the surface. The deuterium gas in the plasma chamber becomes rotationally and vibrationally excited through collisions with energetic electrons generated from the tungsten filament. These excited deuterium molecules and some low-energy electrons produced through ionizations pass into the extraction chamber, where the deuterium is disassociated according to the following reactions:

$$e + D_3^+ \rightarrow D^- + D_2^+$$
$$e + D_2(r^*) \rightarrow D^- + D$$
$$e + D_2(v^*) \rightarrow D^- + D$$
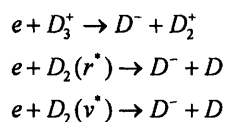
<div align="right">Eq. 4.1</div>

where $D_2(r^*)$ and $D_2(v^*)$ represent the rotationally and vibrationally excited deuterium molecules, respectively. The negatively charged deuterium ions are then drawn from the ion source into the injector by the extraction electrode, where they are focused by two Wein filters, horizontal and vertical steering magnets, and an Einzel lens. The focused beam is then introduced into the acceleration chamber.

The acceleration chamber is a high-vacuum chamber surrounded by a high-pressure SF_6 insulating compartment to prevent electrical breakdown and arcing. The negative deuteron ions are subjected to a terminal voltage as described above. At the axial center of the accelerator column, the negative ions are converted to positively charged ions and accelerated away from the terminal towards the accelerator exit. The conversion from negative to positively charged particles is accomplished though the use of carbon stripper foils. These foils are thin, approximately 10 $\mu g/cm^2$, but strip all the electrons from the deuterium ions, leaving only positively charged deuterons. The lifetime of the stripper foils is dependent on the beam current, particle type and energy, and mounting procedure of the foils, but has been measured to be in the range of 10-100 mA-hr [49].

Once the deuteron beam has been accelerated to the desired energy and exits the accelerating tube, a steering magnet and quadrupole magnets are used to collimate and focus the beam before it is directed into the beam ports shown in Figure 4.2. The beam is

then directed into one of the five beam ports in the radiation vault through the use of a switching magnet.

4.1.1 Setup for Experiments Using MIT-LABA Accelerator

The LABA accelerator has five beam ports (Figure 4.2) that extend into a large, concrete shielded vault used for the experiments described in subsequent chapters. Beam port one was used for all experiments. This port was used for two reasons. Most importantly, the beam is bent by the switching magnet by 30 degrees into beam port one. This bending ensures that only deuterons of the desired energy are directed to the required beam port, as any particles that are heavier, have a different charge, or are of a different energy are accelerated differently by the switching magnet and are not directed into beam port one. This fact guarantees that the final beam of deuterons is monoenergetic, well collimated, and consists only of single deuterons. The layout of the radiation vault is the second reason to use beam port one. The space required for moving the object and detector system around the neutron source eliminates the use of the other beam ports, as rotation to high angles (or, equivalently, low neutron energies – see Figure 2.8) is constrained by the walls of the vault.
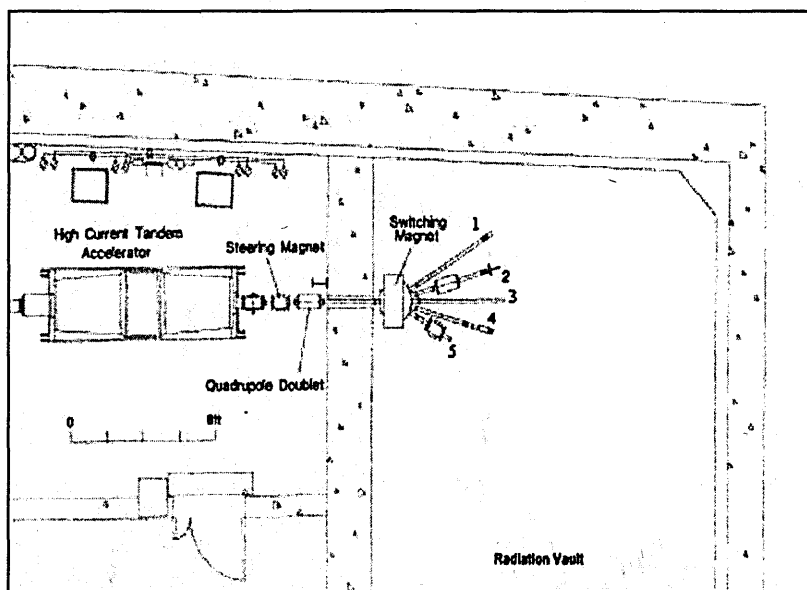
Figure 4.2: MIT LABA accelerator floor plan [48]

Heavy neutron and gamma ray shielding around the accelerator was required to reduce the number of scattered neutrons and gamma rays, as well as to reduce the dose rate to operators and adjacent rooms. The shielding was designed in two steps: first, to moderate and capture as many unused neutrons as possible and second, to shield against any gamma rays produced through neutron interactions or other means.

As the production of gamma rays by any means is detrimental to NRR, the neutron shielding was designed to reduce the number of high-energy gamma rays produced through neutron interactions. Borated polyethylene (5% natural boron by weight) was used as a neutron moderator and capture material. Stray neutrons are moderated in the polyethylene and captured through a $^{10}B(n,\alpha)^7Li$ reaction, emitting a 478 keV gamma ray in the process. This low-energy gamma ray is easier to shield than those emitted from neutron interactions with concrete or simple hydrogenated material such as solid plastic where neutron capture in hydrogen produces a gamma ray at 2.23 MeV. Borated polyethylene was placed around the target except for a thin slit used to provide the neutrons for NRR. Borated polyethylene was also used above the accelerator beam line to shield rooms above the accelerator from neutrons. The borated polyethylene extended at least 30 cm in all directions around the target.

The gamma rays produced both by neutron capture and by deuteron interactions span energies from tens of keV to the mid-MeV energy range. The higher energy gamma rays, especially, are difficult to shield as a significant amount of high-Z material is required. Four inches of lead was placed around the accelerator beam tubes in order to shield the camera from any gamma rays produced directly in the accelerator beamline by deuteron interactions with the stainless steel tubes. The shielding was supported by high-density concrete bricks, 3.84 g/cm^3.

4.1.2 Beam Characteristics

A key advantage in designing accelerator targets for neutron resonance radiography is the ability to tolerate large deuteron beam sizes. The relatively low resolution, on the order of mm, needed for explosives detection allows a large, 1 cm

diameter deuteron beam spot size to be used for the production of neutrons. This reduces the power density in the target windows for a given beam current, and thus allows higher beam currents to be used. A large beam spot has certain drawbacks, however. If the spot is too large, scraping of the beam along the accelerator beam tube results in the loss of deuterons and contributes significantly to the number of gamma rays produced. An analysis of the beam spot size and distribution was made to characterize the deuteron beam produced by the MIT LABA accelerator. Previous work has shown the beam spot to be relatively reproducible over extended periods of accelerator use [49]. However, as the accelerator had not been used for several years prior to this work and the deuteron energy at 2.5 MeV was higher than that used in previous experiments, a re-evaluation of the beam spot size and shape was necessary.

A cooled solid carbon target and digital x-ray imaging plate were used to record images of the deuteron beam [50]. In order to ensure that the beam was aligned and centered on the target, a transparent quartz window was placed at the end of beam port 1 (Figure 4.2) and a 0.5 µA deuteron beam was directed onto the quartz. When the deuterons interact with the quartz, the quartz emits light, which was viewed through a camera pointed at the quartz target. The accelerator and magnet settings were optimized to create a circular, centered beam spot on the quartz window before replacing the quartz window with the carbon target. Using the same settings as for the quartz window to maintain a symmetrical and centered beam, the beam current was increased to 16 µA. The deuterons interact with the carbon through a deuterium capture reaction, activating the carbon target only where the deuteron beam impinged according to:

$$d + {}^{12}C \rightarrow {}^{13}N + n - 0.679 MeV$$
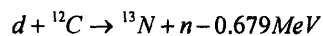
Eq. 4.2

The ${}^{13}N$ subsequently beta decays with a half-life of 9.965 min, releasing a characteristic photon of 2.22 MeV.

The activated carbon flange was allowed to decay until the dose on contact with the back of the flange was in the 5 mrem/hr range. The flange was then removed and the carbon pressed against the imaging side of the ionizing plate, with a thin plastic film interposed to avoid contamination. The beta particles from the nitrogen decay produce an image of the beam spot as shown for a typical spot in Figure 4.3.
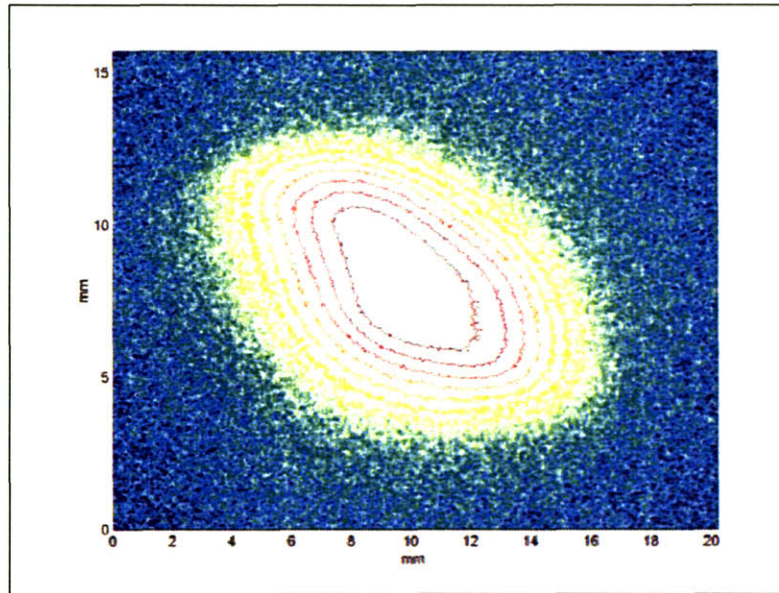
Figure 4.3: Deuterium beam spot

As this figure shows, the beam spot is neither entirely symmetric nor circular. The spot is approximately 1 cm in height and 1.4 cm in width[v], although the most intense portion of the beam is 0.5 cm in width and 0.5 cm in height. The beam does not have Gaussian characteristics; the distribution of intensity across the beam spot is shown in Figure 4.4, which is a histogram of intensity for a line drawn across the center of the beam spot. The intensity is in arbitrary units.

---

[v] In this image, "width" and "height" correspond only to the image, not to the beam as it exits the accelerator as the image has not been aligned with beam orientation. The beam is likely elongated along the vertical axis, i.e., is 1.4cm in height and 1cm in width as it exits the accelerator beam tube.
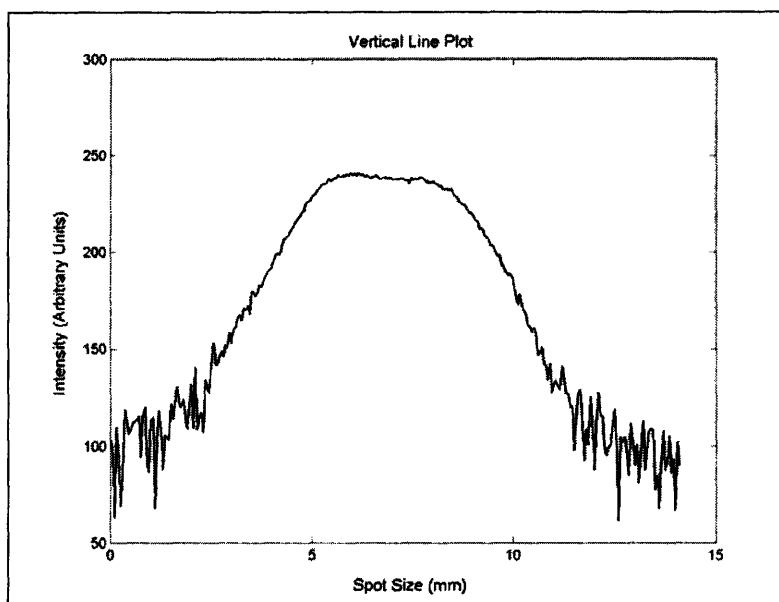
Figure 4.4: Beam intensity across beam spot cross-section. Values were taken from a vertical slice across the beam spot; pixels are 3.6 mm on a side.

Figure 4.3 and Figure 4.4 show a beam that is not symmetric and not Gaussian, but instead is elongated with a relatively large area in the center which has roughly equal intensity. While the spot size is not perfect, the size, shape, and intensity profile are all sufficient for NRR. The beam was found to be reproducible over the period of experimentation. The deuterium gas target, described further in the following sections, is designed to accept a beam larger than 1 cm in diameter through the use of beam scrapers which shape and center the beam. A smaller beam spot is not necessary; in fact, a large beam spot is required to avoid burning a hole through the thin foil windows of the gas target due to power density. The LABA accelerator provides a deuteron beam of sufficient current, size, and reproducibility for all NRR experiments.

4.2 Gamma Spectroscopy

For the purposes of NRR and in particular for the experiments in this thesis, neutron detection (discussed in Section 2.4 and further in Chapter 5) is accomplished by the use of a solid plastic scintillator. Plastic scintillator is a commercially available product designed for neutron detection as well as the detection of heavy ions and gamma

90

rays. Unfortunately, the detection of gamma rays significantly degrades the contrast of neutron images, as the response of scintillators to gamma rays is larger than the response to neutrons (Figure 3.6) due to the energy loss per path length [43]. It has been shown that gamma contamination of NRR images significantly reduces the ability to determine elemental composition [51].

The production of gamma rays is unavoidable to a certain extent as significant numbers of gamma rays are produced through deuterium impingement on various beamline components and through neutron absorption, but the gas target should be designed to produce as few as possible. The first step in designing a gas target was to determine the gamma ray production from various target component candidate materials when subjected to a deuteron beam.

4.2.1 Experimental Setup

Materials for use in a deuterium gas target must meet the following requirements. They must have high melting points to withstand the high temperatures caused by heat deposition from the accelerated deuterium ions, they must have high stress tolerance to avoid premature failure, they must be easy (or at least possible) to fabricate into the necessary components, and, finally, they must produce a minimum number of gamma rays. Besides the beamline material itself, components of the gas target that are exposed to deuterons includes the thin foil window, the metal strongbacks that support the foil windows, and the beamstop which ultimately absorbs any deuterons which do not produce neutrons or are not absorbed in the strongbacks. Previous work has investigated the gamma production from tantalum, steel and the cobalt-based alloy Havar due to 5 MeV deuterons in support of the development of gas targets for NRR, but gamma production will vary with neutron energy and it was necessary to establish the gamma production due to 2.5 MeV deuterons [29]. The metals chosen for evaluation were nickel, iron, stainless steel, tungsten, machinable tungsten (heavy metal), molybdenum, and gold.

These metals were chosen for a variety of reasons. Stainless steel is the primary component of the beamline materials; some deuterium impingement is likely despite the

best efforts in focusing the beam. Nickel and iron were chosen as separate materials to determine the contributions to the stainless steel spectrum. Tungsten is a primary candidate for thin foil windows for the gas cell due to its high melting point and ability to withstand mechanical stress; however, it is an extremely difficult material to machine and quite expensive for high purity material. Machinable tungsten is available in a variety of alloy compositions. We used a material made from 90% tungsten, 7% nickel, and 3% iron; the combination results in a material that is much easier to use but retains most of the strength and heat resistance of pure tungsten. Molybdenum has similar properties to tungsten, while gold has been used as the beam stop in many gas targets. A summary of important material properties is shown in Table 4.1.

Table 4.1: Material properties

Material	Purity (%) / Composition	Density (g/cm^3)	Melting Point (°C)
Stainless Steel	AISI 316	8.17	1399
Gold	99.95	19.32	1064.2
Nickel	99.95	8.91	1455
Tungsten	99.998	19.30	3410
Machinable Tungsten	90%W, 7%Ni, 3%Fe	17.42	~1200
Molybdenum	99.95	10.22	2623
Iron	99.95	7.87	1538

4.2.1.1 Metal Target Mounting

Thin metal foils were used as target materials for the stainless steel, pure tungsten, gold, nickel, iron, and molybdenum, while a thick (1/4 inch) piece of machinable tungsten was used due to availability. The thin metal foils and the thick piece of machinable tungsten were attached to an aluminum blank flange, cooled with a constant flow of chilled water through the back of the flange (a similar target is shown in Figure 4.5).
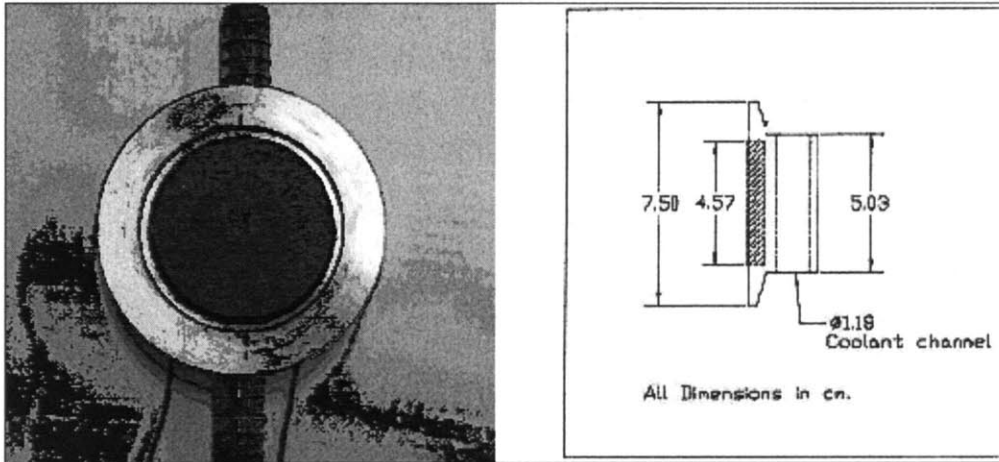
Figure 4.5: Water-cooled target for gamma spectroscopy [50]

The thin metal foils were attached to the flat face using double-sided conductive carbon tape to hold the foil flat against that flange, ensuring good heat conductivity to the aluminum for adequate cooling and electrical conduction through the carbon tape. The thin metals foils were of sufficient thickness to ensure that the entire deuteron beam was stopped in the foil. To minimize the amount of deuteron beam spray onto the aluminum flange, the metal foil was made large enough to cover the entire flange face.

The flange and foil assembly was placed on the end of beam port one of the MIT-LABA accelerator (Figure 4.2). The use of beam port one guarantees that only deuterons of the desired energy are directed onto the foil as discussed above. A beam shaping system was placed upstream of the foil. The beam shaper consisted of four tungsten scrapers which serve to shape the beam into a 1 cm diameter beam spot. Current was measured on the four scrapers in order to position the deuteron beam in the center of the scraper system and thus the center of the foil. The flange and foil were electrically isolated downstream from the scrapers by a ceramic break and the deuterium beam current was measured on the aluminum flange. While all attempts were made to minimize the amount of deuterium beam spray onto beamline components other than the foil in question, a small number of deuterons inevitably impinged upon the tungsten beam scrapers and a small aluminum beamline adaptor. The contribution of gamma rays from

93

these components is small, and is pointed out when any gamma rays from these materials are observed.

4.2.1.2 Detector Arrangement

The gamma ray detector used was a liquid nitrogen-cooled, high-purity germanium (HPGe) detector (a good description of HPGe detectors can be found in ref. 30). HPGe detectors have good energy resolution, which facilitates the identification of the energy of the gamma ray peaks. Energy resolution on the order of 3 keV over an energy range of 80 – 5500 keV was easily achieved. Cesium-137 and cobalt-60 sealed radiation sources were used to calibrate the detector. Typical gamma rays detected in the background were from potassium-40 and thallium-208, also used to calibrate the detector. The low energy (661.62 keV)of the ^{137}Cs gamma rays, medium energy (1173.24, 1332.5, and 1460.75 keV) ^{60}Co and ^{40}K gamma rays, and high energy (2614 keV) ^{208}Tl gamma rays allowed for accurate calibration of the detector over the entire energy range.

A key concern was the detection of gamma rays produced by deuteron impingement on the metal foil, rather than those of the gamma rays produced by any other means. In an attempt to filter out those gamma rays produced from various parts of the beamline components, the detector was aligned at a ninety degree angle to the deuteron beam, aimed directly at the target foil edge-on. The detector was heavily shielded and collimated. A 30.5 cm long collimator with a rectangular opening 2.54 cm wide by 5.08 cm high was centered on the HPGe detector face and was aimed at the foil at a detector-foil distance of two meters. The sides of the column were shielded heavily with lead. On the side of the detector facing the accelerator beam ports, a minimum of 15.25 cm of lead was placed to shield the detector from gamma rays produced in the beamline. The side of the detector away from the accelerator beamline was shielded with 10 to 20 cm of lead. The bottom of the detector was shielded with 7.62 cm of lead, while the top of the detector was shielded with 15.25 cm of lead to shield the detector from background radiation and reduce the dead time in the detector to produce adequate signal-to-noise ratios. By aiming directly at the foil and shielding the detector, we were able to minimize the number of gamma rays detected that were produced in the beamline.

Figure 4.6 shows the arrangement of the detector and shielding apparatus, aimed at beam port one.

Figure 4.6: Gamma ray detector and shielding arrangement

4.2.1.3 Experimental Procedure

Gamma production from each metal was assessed using a stable beam of 2.5 MeV deuterons. For all the experiments involving gamma spectroscopy, beam port one was used to ensure that only the desired 2.5 MeV deuterons were directed onto the target foil, as any particles of greater or lesser energy or mass would be directed elsewhere and would never impinge on the target foil. While the beam current generally was kept fairly low to minimize the size of the beam[vi], the current was varied depending on the metal due to the differences in melting point, heat conductivity, and offgassing inherent to each material. The nickel, in particular, tended to melt when a beam current greater than 5 μA was applied, while the stainless steel produced sufficient amounts of gas when heated that the vacuum necessary for the accelerator to operate was degraded. In addition, the thin

---

[vi] While a higher beam current would have resulted in a higher signal to noise ratio and faster data collection times, a higher beam current also meant a larger beam spot which increased the amount of beam on the scrapers of the beam shaper. For these experiments meant to determine gamma production from a specific material, the amount of beam on the scrapers was minimized by using a lower beam current.

foils were not efficient at conducting heat to the flange and the heating of the foils was kept to a minimum by using low beam currents.

Gamma ray spectra were taken for at least the minimum time necessary in order to achieve adequate statistics. In general, this amounted to irradiation times on the order of 3600 seconds. All data collected was subsequently normalized to beam current and irradiation time to account for the differences in beam current used in these experiments and the different irradiation times. The irradiation times and beam currents used for each material are shown in Table 4.2.

Table 4.2: Irradiation currents and times

Material	Beam Current (μA)	Irradiation Time (s)
Gold	3.72	3661
Pure Tungsten	2.88	3602
Machinable Tungsten	2.69	3609
Stainless Steel	2.01	1819
Molybdenum	2.94	3668
Nickel	1.70	2361
Iron	3.47	2908

Once the gamma detection with the deuteron beam on was completed, the foil was taken off the aluminum flange and placed directly in front of the HPGe detector to determine any activation of the foil. The gamma radiation from the foil was counted for between 1500 and 3600 seconds after the foil was irradiated. The foil and counting times are shown in Table 4.3.

96

Table 4.3: Activated foil counting times

Material	Counting Time (s)
Gold	2554
Pure Tungsten	3600
Machinable Tungsten	1802
Stainless Steel	3606
Molybdenum	2656
Nickel	1513
Iron	3198

4.2.2 Results of Gamma Spectroscopy

As mentioned, the gamma spectra have been normalized by irradiation time and current so that results can be compared. The gamma ray spectra are shown in Figure 4.7 through Figure 4.13. These figures have been individually scaled to highlight features of each spectrum; Figure 4.14 shows the gamma ray spectra from all seven materials on the same scale for better comparison.
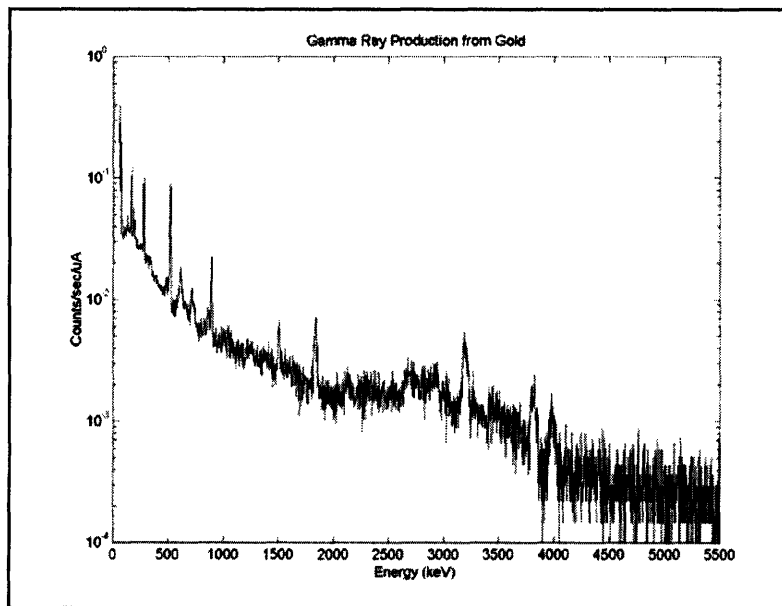
Figure 4.7: Gamma ray production from gold
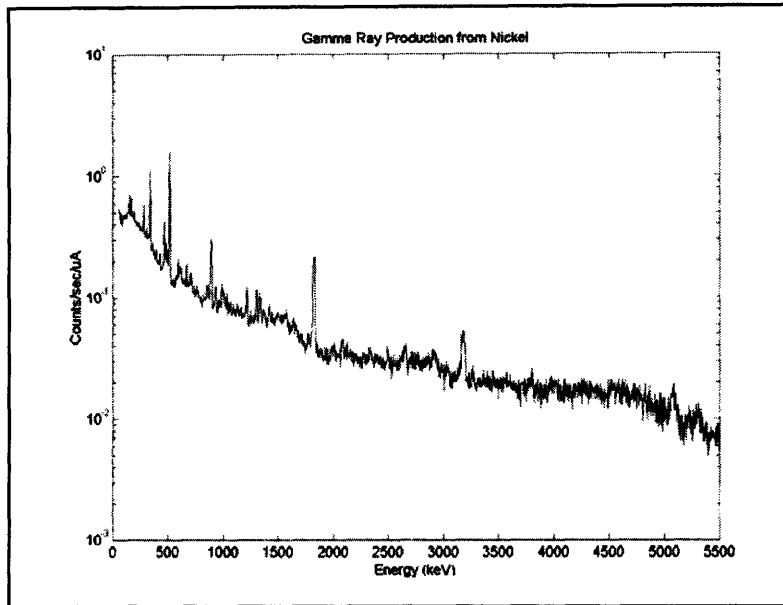
Figure 4.8: Gamma ray production from nickel
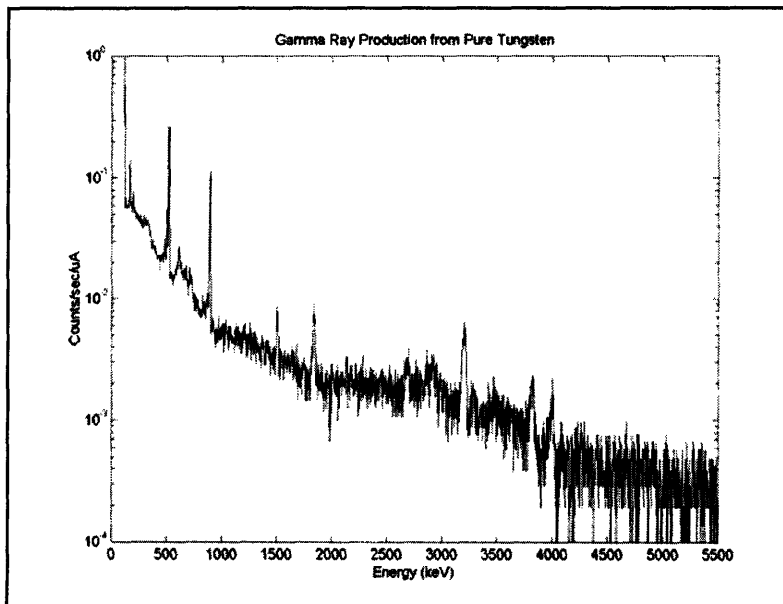
Figure 4.9: Gamma ray production from pure tungsten
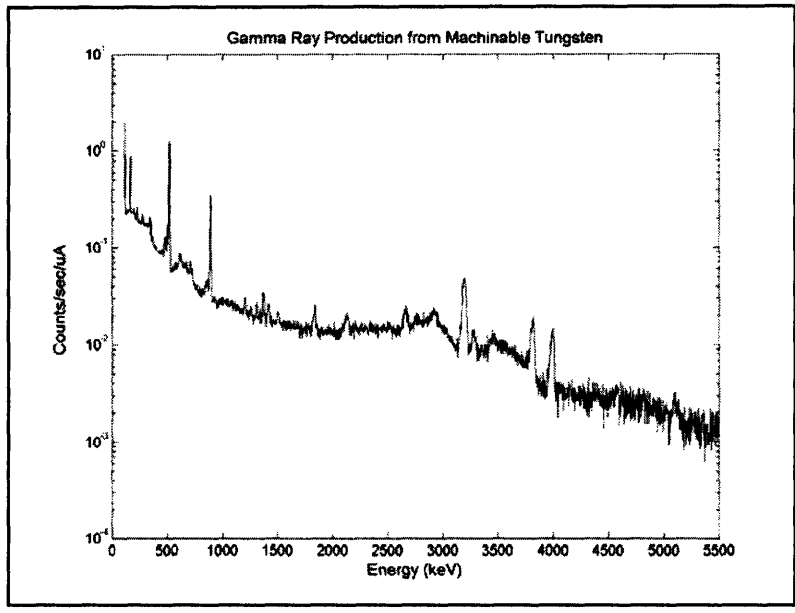
Figure 4.10: Gamma ray production from machinable tungsten
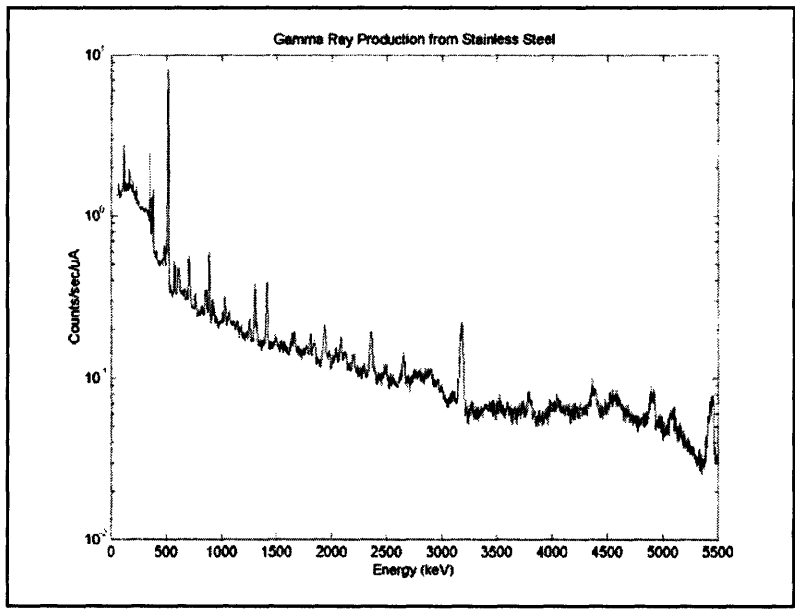
Figure 4.11: Gamma ray production from stainless steel
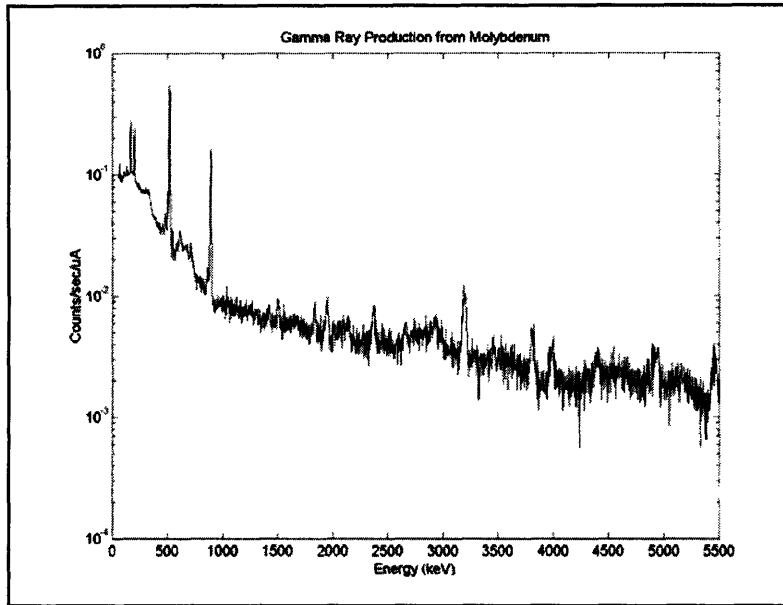
Figure 4.12: Gamma ray production from molybdenum
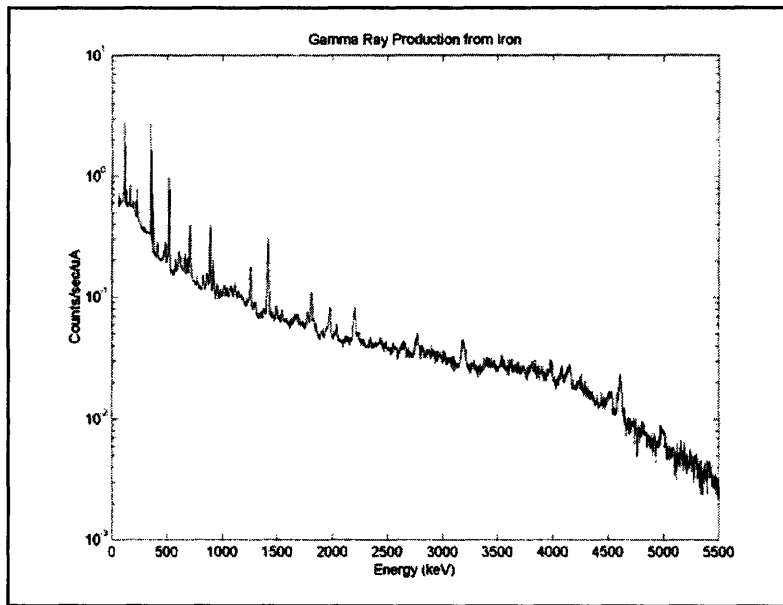
Figure 4.13: Gamma ray production from iron

100
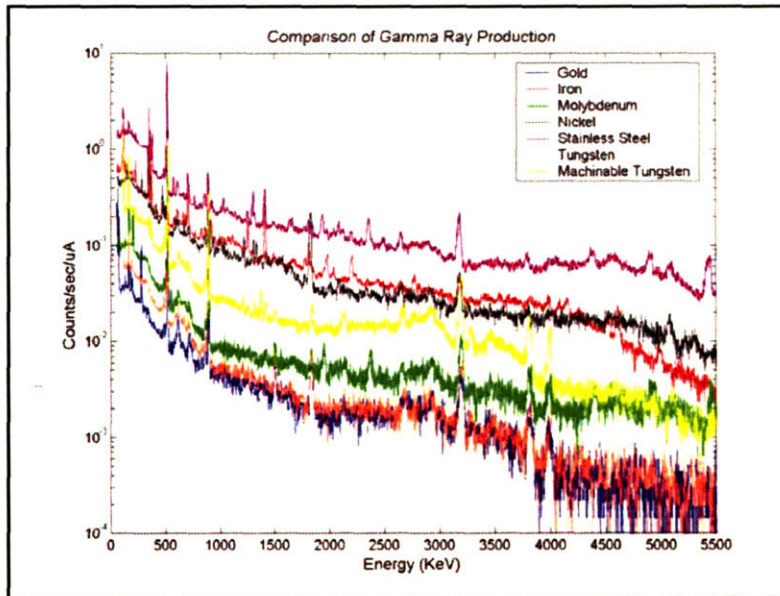
Figure 4.14: Gamma ray production from all materials

Not only is the prompt gamma production important, but the activation of the foils is as well. Foil activation leads to requirements on safety and handling of the foils after irradiation, especially in the event of an abrupt foil failure. If radiation is present for extended periods of time, the used foils are considered a radiological hazard. The material used for the gas target windows should ideally produce few prompt gamma rays and exhibit little, if any, activation. The activation of each material under consideration for the foil windows was measured by removing the irradiated foil from the flange immediately and placing only the foil directly in front of the HPGe detector. The radiation emitted was thus measured and normalized to the number of incoming deuterons and time. The results are shown in Figure 4.15 through Figure 4.21 below.
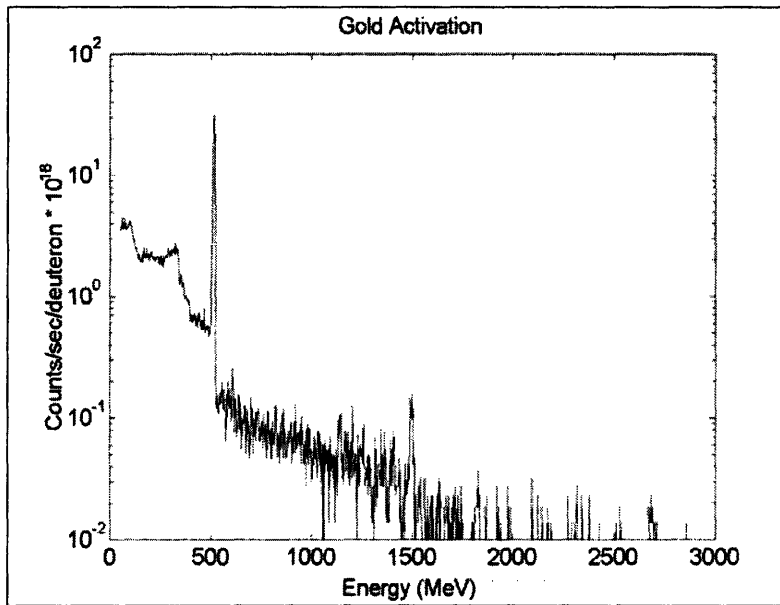
Figure 4.15: Gold foil after activation
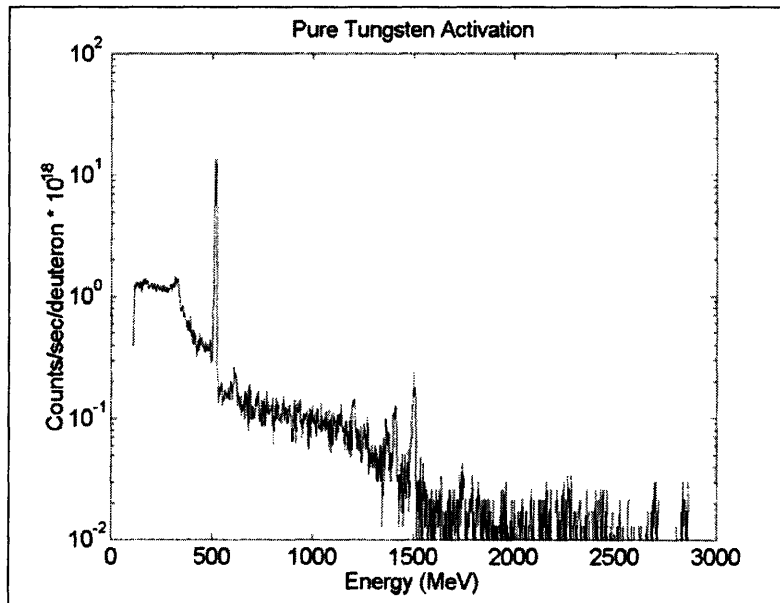
Figure 4.16: Pure tungsten foil after activation

102
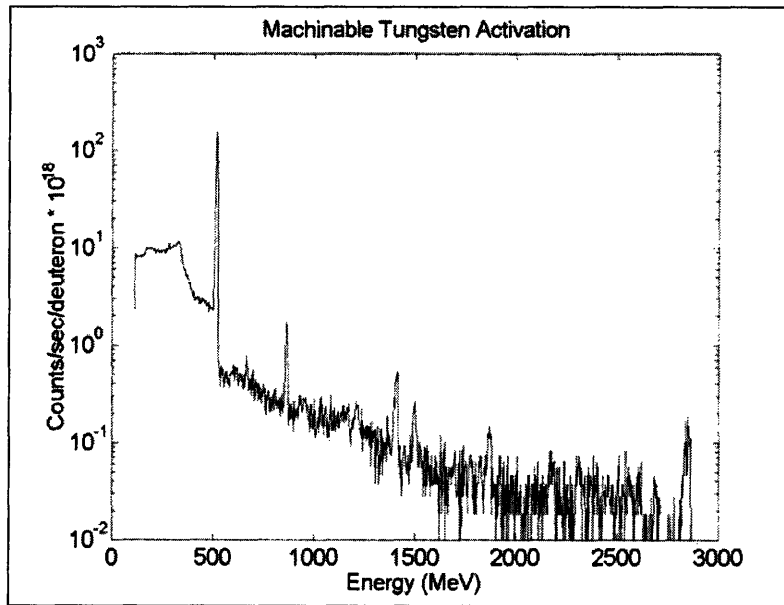
Figure 4.17: Machinable tungsten foil after activation
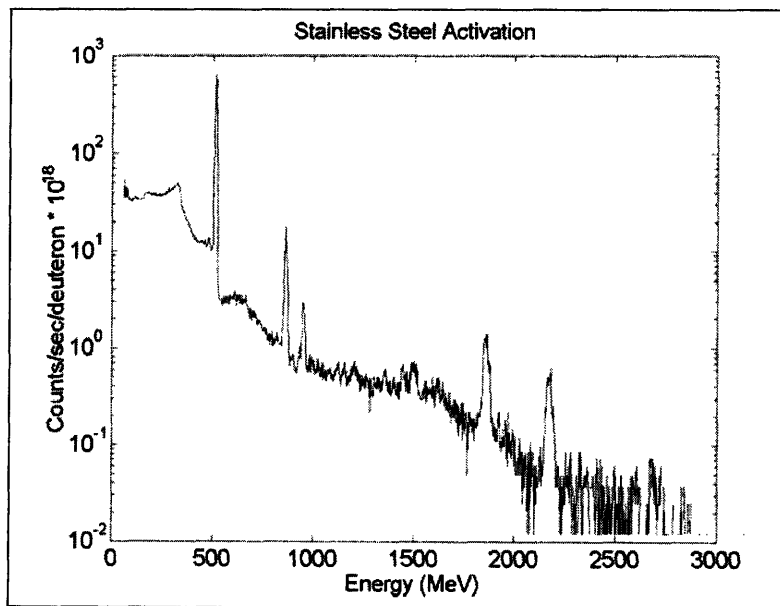
Figure 4.18: Stainless steel foil after activation
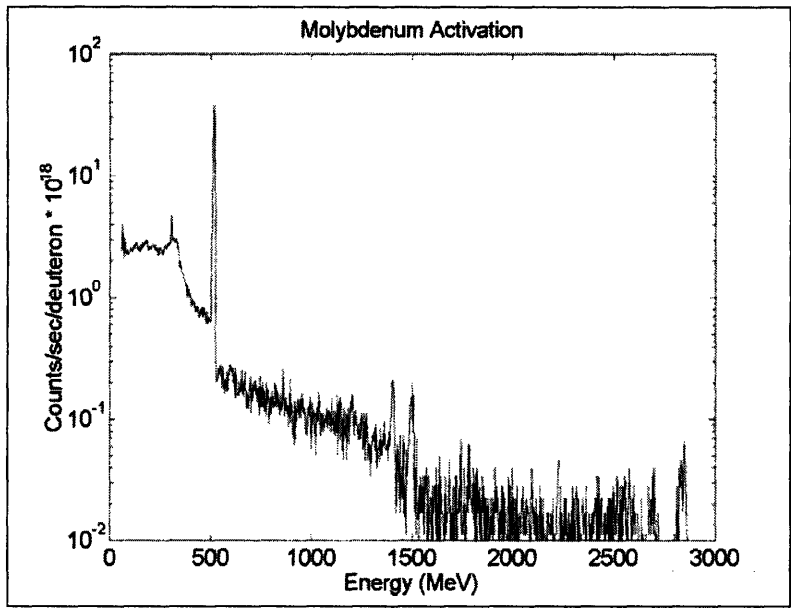
Figure 4.19: Molybdenum foil after activation
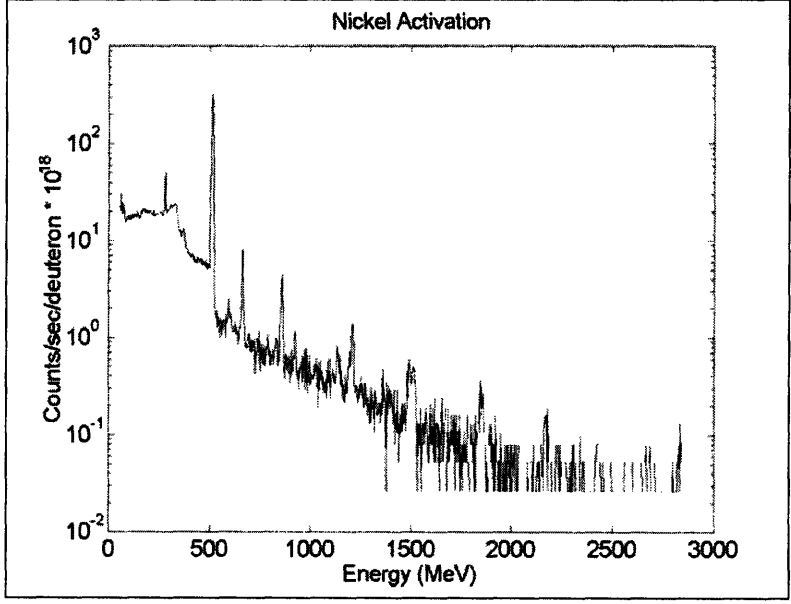
Figure 4.20: Nickel foil after activation
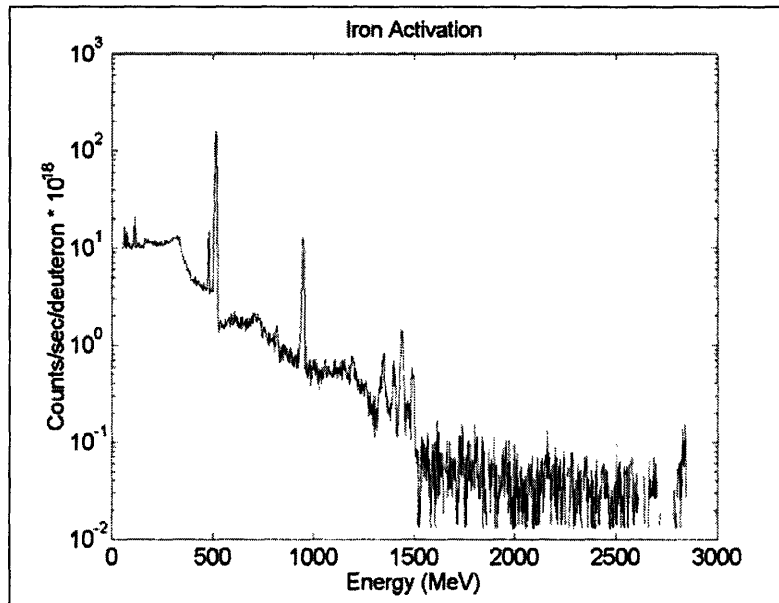
Figure 4.21: Iron foil after activation

4.2.3 Discussion of Gamma Production

The gamma spectroscopy clearly showed a difference in the overall number of gamma rays produced by different metals and in the characteristic energy of the main peaks observed. Stainless steel was by far the most prolific source of gamma rays, both in absolute number as well as the number of high energy gamma rays and number of distinct energy peaks. This is problematic, as the majority of accelerator beam tubes are constructed of stainless steel. A tightly focused beam spot with little, if any, stray particles that have the opportunity to interact with the beam tube is a necessity. On the opposite end of the spectrum, gold, molybdenum, and tungsten produced quite similar gamma spectra, with a low overall count rate and small number of high energy peaks. Of these three metals, only tungsten and molybdenum are suitable for thin windows; gold is too soft and has too low a melting point to serve as a strong window. The choice of material was thus limited to tungsten and molybdenum.

There are striking similarities between the gamma production for gold, molybdenum, and tungsten. Some of these similarities are inherent to germanium detectors and gamma spectroscopy, such as the 511 keV annihilation peak and the gamma rays produced from neutron inelastic scattering in the germanium detector itself.

105

Neutron inelastic scattering produces the broad peak at 689 keV from scattering off ^{72}Ge and the broad peak at 595 keV from ^{74}Ge. The three peaks between 3000 and 4000 keV are present in both the molybdenum and the tungsten spectra, although lower energy peaks differ. Molybdenum has a few higher-energy peaks than tungsten, namely, the 5400 keV and 4900 keV peaks shown in Figure 4.12. In terms of activation, molybdenum has slightly higher activation levels than tungsten, but both are relatively low, especially when compared to the activation present in stainless steel or iron.

Tungsten and molybdenum are both suitable metals for the foil windows of the gas target. Tungsten is marginally better, given that it produces the fewest gamma rays from deuteron bombardment and is the strongest of the metals tested, but it is also much more difficult to find as pinhole-free thin foils than other metals. The gas target is able to accommodate both tungsten and molybdenum foils with little difference in result.

4.3 Gas Target Design

The gas target design was based in part on the need for a large neutron flux and low maintenance requirements as well as the need to reduce the overall number of gamma rays produced. The design work for the gas target was undertaken at Lawrence Livermore National Laboratory (LLNL), while the final gas target was manufactured by the Champ Co. in Campbell, CA. The design specifications included a neutron flux on the order of 10^9 n/sr/s at $0°$, using beam currents on the order of 50 μA. The deuteron energy was specified to be 3.0 MeV[vii].

As discussed in Section 2.3.3.3, a windowed gas target consists of the deuterium gas cell, isolated from the vacuum of the accelerator system by a thin foil window, and outfitted with a beamstop to absorb accelerated particles that pass unaffected through the gas cell. The thin foil window must be able to withstand high mechanical stresses and temperatures without failing, but cannot be made so thick that the energy of the incoming

---

[vii] Although the deuterons used in the experiments in this chapter were at an energy of 2.5 MeV, this was due to limitations of the MIT LABA accelerator. The gas target described here and developed for the purposes of high-current NRR was designed to accommodate deuteron energies up to 3.0 MeV, which expands the range of neutron energies available.

106

deuterons is unduly affected. The materials that the gas cell is made of must be transparent to neutrons and produce few, if any, gamma rays from deuteron bombardment. In addition, for use in a high-throughput environment, the gas cell must be fairly inexpensive and relatively easy to manufacture, while maintenance requirements should be low and replacement straightforward.

The gas target designed for the NRR experiments described in this thesis is an attempt to remedy deficiencies in windowed gas target designs. The thin foil window for the gas cell has been augmented by a metallic strengthening support lattice ("strongback") to allow for higher beam currents and higher gas pressures. The gold metal beam stop of previous gas targets was replaced with a thick tungsten beamstop, supported by a second support lattice. To decrease the stress on the target due to temperature increases from beam deposition, the gas cell was surrounded by a chamber through which an argon gas was pumped for target cooling. Upstream from the gas cell is a beam scraper assembly, consisting of four tungsten plates that serve to shape and center the deuteron beam. Deuteron beam current can be measured on each of the four plates to ensure that the beam is centered through the beam tube. The beam scrapers ensure that the deuteron beam is 1 cm in diameter and does not come into contact with the sides of the beam tube to produce gamma rays though deuterium interactions with stainless steel. A cross-sectional diagram of the entire gas target is shown in Figure 4.22. The individual components are described in more detail in the following sections.
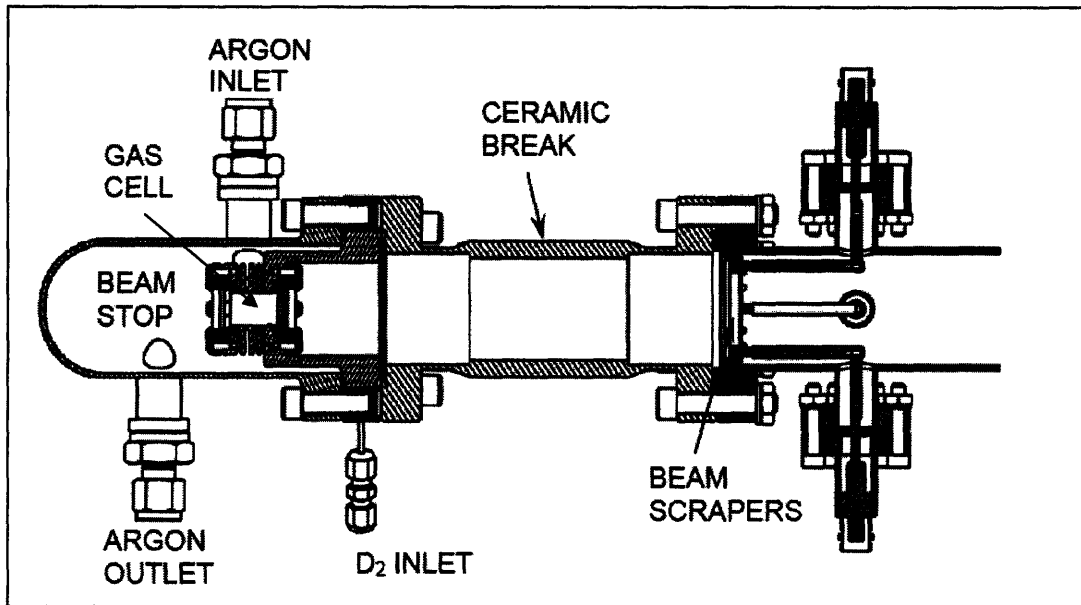
Figure 4.22: Gas target design

4.3.1 D₂ Gas Cell

The deuterium gas cell is the neutron production site. The cylindrical gas cell is a 1.5 cm long, 1 cm diameter cylinder, closed at either end with thin metal foils. These foils provide the only separation between the vacuum of the accelerator beamline and the deuterium chamber on the front end of the gas cell, and the only separation between the argon cooling system and the gas cell at the exit of the gas chamber. The front foil must therefore be pinhole-free to avoid deuterium leakage, but must also be as thin as possible to allow for minimum deuteron energy loss. The front foils used in the experiments described in this thesis were 5 μm tungsten or 7 μm molybdenum foils, chosen for the excellent mechanical properties outlined in Table 4.1 and the low gamma production as shown in Figure 4.9 and Figure 4.12. The back tungsten beamstop was a 0.1 mm thick tungsten foil.

While the outer flange is made of aluminum, the gas chamber is lined tungsten to ensure that all components facing the deuteron beam are composed of tungsten. This allows the overall design to be easily machined and less expensive than if the entire gas cell were made of tungsten. The metal foils are supported by two thick tungsten lattice structures which are designed to allow for 60% beam transmission and provide additional

108

support for the thin windows (see Section 4.3.1.1). The lattice structures and the foil windows are held down by aluminum rings bolted to the gas cell body, with a tungsten cover on the beam-facing side. The cell is sealed at the thin windows by a rubber O-ring. As a means of cooling, the gas cell is surrounded by aluminum fins, designed to conduct heat from the gas cell, the foil windows, and the strongbacks to the circulating argon cooling chamber. A length-wise cross-section of the gas target, without the argon chamber, is shown below in Figure 4.23.
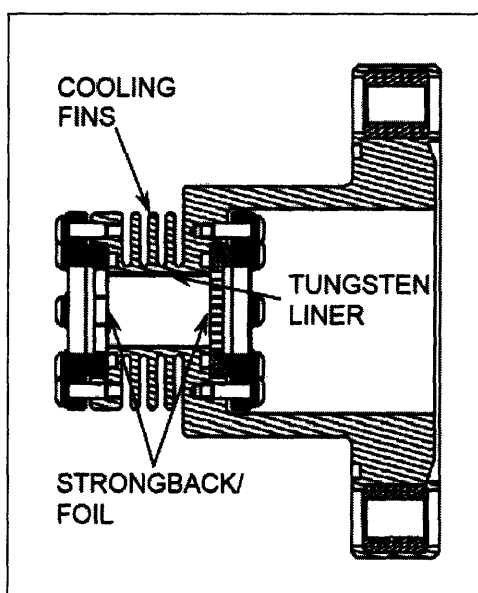
Figure 4.23: D_2 gas cell design

A primary advantage of the gas cell is that all the components are standard sizes and thus readily replaceable. The flanges connecting the target modules to each other and to the accelerator are standard Conflat ™ type, and the insulating ceramic break and the scraper modules are based on off-the-shelf vacuum components. If the foil windows break or are punctured, the gas cell can be purged and removed from the gas target, broken foils removed and easily replaced, and the gas cell reattached to the accelerator and refilled. Originally, three gas targets were purchased; all the material parts are interchangeable and the tools needed are standard sizes. In a commercial implementation, it is most likely that the targets will be replaced as units and returned to a central location for window replacement or other maintenance.

4.3.1.1D₂ Cell Window Strengthening

The deuterium gas cell window was strengthened by adding a tungsten lattice backing to the thin front entrance window. This backing, or strongback, was designed to be thick enough to provide significant support to the window and allow for extra heat transfer to reduce heating in the thin window itself. An identical strongback was placed on the exit window of the gas target. The strongbacks were made of tungsten to take advantage of the favorable material properties previously discussed in Section 4.2.2.

The entrance strongback is shown below in Figure 4.24. The strongback itself is 2.5 mm thick with 73 circular holes 0.1 cm diameter. The holes are patterned in such a way as to allow for 60% transmission of the deuteron beam, while the solid portions of the strongback are thick enough to stop the entire beam within the metal. The strongback is placed flush against the thin tungsten window and the unit is held down and sealed as discussed above.
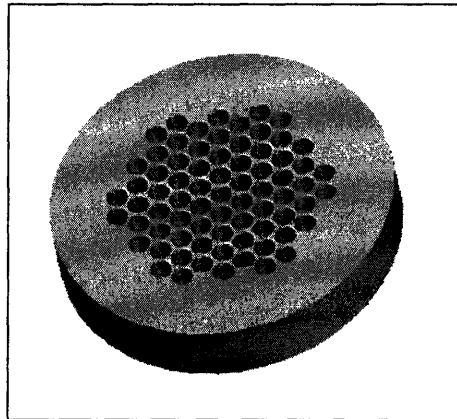
Figure 4.24: Front tungsten foil window support structure

4.3.1.2Deuteron Slowing Down

The foil windows of the gas target provide the only means of separation between the vacuum of the accelerator system and the gas target and between the gas target and the argon cooling chamber, so the windows must be strong enough to withstand the heat and pressure induced by the deuteron beam. However, the front window that separates the vacuum from the gas cell does reduce the energy of the incoming deuterons and creates some energy broadening of the incoming deuteron beam that affects the energy of

110

the resulting neutrons. A trade-off exists between the thickness, and thus the strength, of the foil windows and the maximum energy of the deuterons able to reach the deuterium gas cell. The maximum thickness of the foil window was determined by the slowing down power of the foil, while the minimum thickness was determined by the heat and power deposition in the foil and the resulting deformation and structural degradation.

As the incident deuteron beam passes through the gas cell foil window, energy loss due to electromagnetic interactions between the deuterium ion and the metal foil cause the deuteron to interact with the deuterium gas at a lower initial energy. The energy of the deuteron beam is also spread by interactions within the gas cell. Broadening of the energy spectrum of the incident deuteron beam causes broadening in the energy of the neutrons produced. For applications such as NRR, in which a monoenergetic neutron beam is required, the energy spread of the deuterons in the gas target system is a vital quantity.

The deuteron energy loss can be calculated using the freely available SRIM/TRIM computational software [52]. Simulations of the energy loss of a 2.5 MeV deuteron beam in a 5 μm tungsten window and a 7 μm molybdenum window show average deuteron energy after the foils of 1.89 ± 0.040 MeV and 1.83 ± 0.030 MeV, respectively, as shown in Figure 4.25. Figure 4.26 shows the final energy of a 3.0 MeV deuteron beam through the same windows to be 2.45 ± 0.030 MeV and 2.40 ± 0.027 MeV, respectively. Due to the lower density of molybdenum, the broadening of the energy spectrum is less significant than that of the tungsten window, although the thicker foil increases the average energy loss. These two figures show that although there is some energy spread of the deuterons after they pass through the foil window, the broadening is small, no more than 150 keV. The greater effect of the foils is on the overall energy of the deuteron beam.
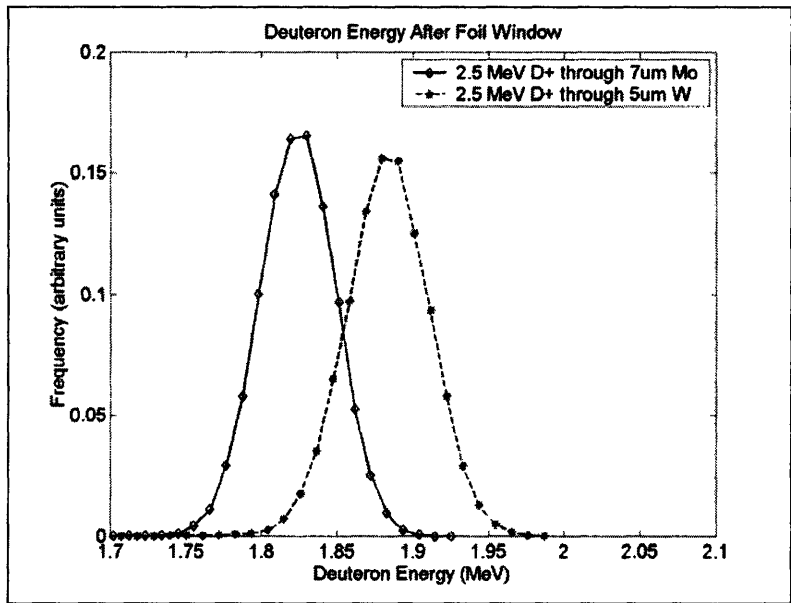
Figure 4.25: Energy broadening of the 2.5 MeV deuteron beam through gas cell thin foil windows.
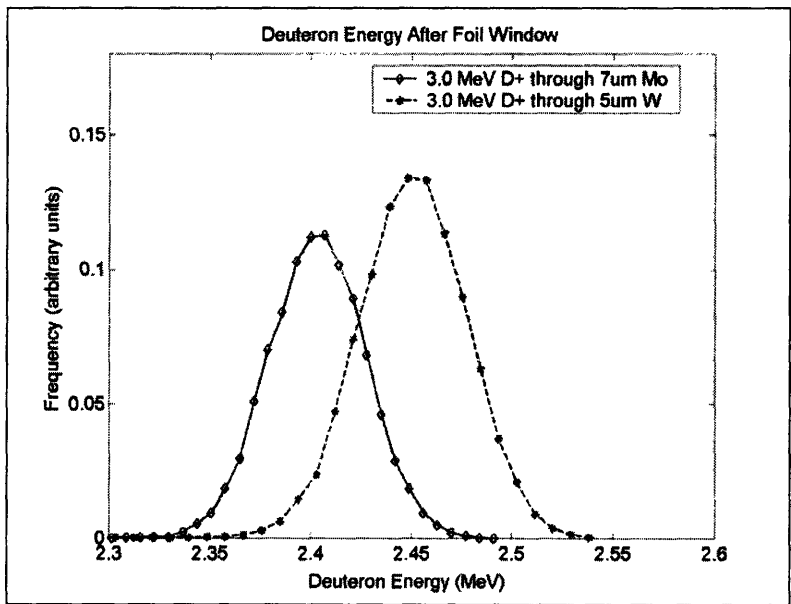
Figure 4.26: Energy broadening of the 3.0 MeV deuteron beam through gas cell thin foil windows.

The deuteron energy distribution is further broadened through the deuterium gas in the cell, which contributes most significantly to the neutron energy spread. Deuterium ions can react with the deuterium gas to produce neutrons throughout the length of the cell, creating an energy spread in the neutron beam between those neutrons created at the front of the target and those created at the back. Using SRIM, the energy spread of the resultant neutrons from initial deuterons of 2.5 MeV (including the energy drop from the foil windows shown in Figure 4.25) is 420 keV for the 5 μm tungsten window and 440 keV for the 7 μm molybdenum window. The average energy spread of the neutrons produced by a 3.0 MeV deuteron after passing through a 5 μm tungsten window is 328 keV and through a 7 μm molybdenum window is 335 keV. For the purposes of NRR, this spread in energy of the neutron beam is acceptable, so long as the object under investigation spans an angle of less than 10°, larger objects can be probed by scanning smaller slices to build up a composite image.

4.3.1.3 Heating in the Gas Cell

As the beam passes through the windows of the gas cell, energy is deposited in the metal as a function of deuteron energy and metal thickness. Table 4.4 shows the energy deposition in various components of the gas cell due to a uniformly distributed, 1 cm diameter, 3 MeV, 1 μA deuteron beam, assuming the holes in the rear strongback are aligned with the front strongback. It is apparent that most of the power lost will be lost to the front foil and front strongback, the argon beamstop (discussed in the following section), and the rear foil. Removal of the heat from these components is a key concern, as studies have shown that cooler gas targets produce more neutrons and higher neutron to gamma ratios [53].

Table 4.4: Energy deposition in gas cell components

Target Component	Energy Density (W/cm^2)	Total Energy Deposited (W)
Front foil (5µ W)	0.7057	0.320
Front strongback	3.8197	1.269
Deuterium gas (4 atm)	0.2042	0.092
Rear foil (5µ W)	0.8188	0.371
Argon beamstop	2.0919	0.948

4.3.2 Beam Stop

The beam stop of any gas target serves its obvious primary purpose – stopping the deuterons which do not interact with the target gas – but in the case of the target described here, the beam stop also serves a secondary purpose as a cooling system. Argon was chosen as the beamstop gas for a number of reasons. First, argon was thought to have few deuteron interactions that produced neutrons or photons (in practice, it turned out that significant numbers of "off-energy" neutrons were produced and the target was modified to stop the beam in tungsten – see below.) Second, the deuteron stopping power of argon is high since it is a relatively heavy gas. Third, as a noble gas, argon is nontoxic and inert so there are no safety concerns related to the use of argon, and finally, argon is a fairly inexpensive gas. It should be noted that flowing gas beam stops in general have the advantage that the deuterium gas formed from the stopped deuterons is swept out of the target system and thus will not interact with subsequently arriving beam deuterons. In a solid beam stop, deuterium can accumulate, and in interacting with deuterons that are slowing through a wide range of energies, can produce off-energy neutrons. This effect has not been found to be significant in experiments to date, but should be considered as beam currents are scaled up in future gas target designs. Unfortunately, as will be discussed later, it was discovered that neutrons could also be produced by deuterons in argon, so that care was necessary to avoid this.

The beamstop itself is an aluminum housing that fits around the gas cell, attaches to the cell housing with 6 ¼-20 bolts and is sealed by a rubber O-ring. The beamstop can

thus be easily removed to allow access to the gas cell back window without removing the entire assembly from the accelerator beamline. The beamstop has two gas fittings – one on either side of the housing – which allow for circulation of the argon. A cross-section of the beamstop is shown along with the rest of the gas target assembly in Figure 4.22. The beamstop extends three centimeters from the rear window of the deuterium gas cell.

The principal function of the gas beamstop is to fully stop all the deuterons that do not interact with the deuterium in the gas cell so that they do not reach the aluminum housing of the gas target. To reduce the stress on the rear window of the gas cell, the beamstop was designed to hold 4 atm of argon so that the beamstop pressure would be equal to that of the gas cell. The equal pressure reduces the stress on the rear foil window. Using SRIM, the stopping power of three centimeters of argon at 3 atm was calculated to ensure adequate stopping of the beam, shown in Figure 4.27. Obviously, the stopping power of 4 atm of argon is more than enough to fully stop the deuteron beam, leaving some room for error in under-pressurization[viii].

1.17 MeV d+ in 3 atm Ar

0   Gas Target Length (mm)   30 mm
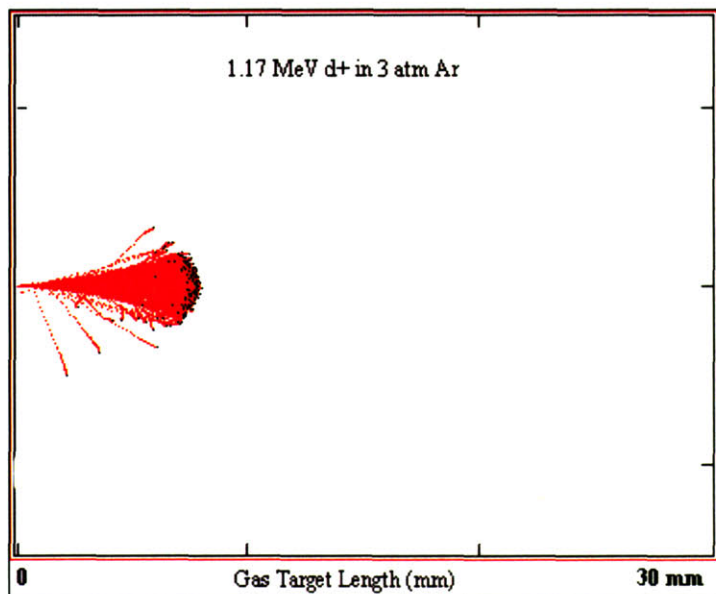
Figure 4.27: SRIM simulation of argon stopping power. Deuteron energy was 1.17 MeV; pressure in the gas beamstop was 3 atm.

[viii] It is better to underpressurize the beamstop than to overpressurize. The rear window of the gas cell is supported by the strongback lattice on the outside of the cell, meaning that underpressurization of the beamstop forces the foil window against the strongback, providing support and structural backing. In the event of overpressurization of the beamstop, however, the foil window is pushed *away* from the strongback into the gas cell. In this case, the foil window is likely to rupture.

4.3.2.1 Cooling of D_2 Gas Cell

Although the beamstop was designed in such a way that 4 atm of argon could be confined, the gas can also be circulated through the beamstop, which is required for any significant beam current. This is a great advantage for NRR, as the argon cools the deuterium gas target, permitting the cell to accept higher beam current and thus produce more neutrons. A constant flow of argon provides a means of forced convection to dissipate the heat deposited in the gas cell rather than simple conduction to stationary air in the beamstop or metal-to-metal contact with the gas cell. As discussed in Section 4.3.1, aluminum fins surround the gas cell to increase conduction.

The argon beamstop is not expected to remove all the heat deposited within the gas cell; however, as shown in Table 4.4, even some reduction in heating makes a significant difference. The rate of heat transfer to forced convection from the flowing argon can be found from the following equation [54]:

$$\dot{Q} = \bar{h}A(T_w - T_\infty)$$

Eq. 4.3

where Q is the heat removal rate, h is the convection heat transfer coefficient, and the quantity $T\text{-}T_\infty$ is the difference between the temperature of the surface (T_w) and the temperature of the argon (T_∞). As the heat transfer coefficient, h, is a function of the velocity of the argon, an increase in the argon flow or a decrease in the argon temperature will reduce the temperature in the gas target. For the experiments described in the following chapters, argon was flowed through the beamstop at atmospheric temperature, 2.5 scfm, and 35 psia[ix]. This pressure in the beamstop is enough to stop all the deuterons in the beam, and the argon flow cooled the gas cell to the extent that we were able to consistently run at minimum current of 20 μA with no appreciable increase in accelerator vacuum pressure due to heating of the gas target.

Although the experiments in this thesis flowed argon through the target but did not recirculate the gas, future systems can be developed for the same gas target design

---

[ix] The pressure at the outlet of the argon tank was 40 psia, while the pressure of the argon leaving the gas cell was 30 psia.

that can recapture the argon in a cooling/pumping system. Cooled argon gas will further reduce the temperature in the target and enable an increase in deuteron beam current. Recirculating the argon will obviate the need to replenish the argon supply. However, the requirements on the pump to provide continuous argon flow at ~ 4atm and 3 scfm are considerable, and for the proof-of-principle experiments described here, the added expense and complication of a recirculating argon system was unnecessary.

4.4   Experimental Assessment

Trial experiments before full-scale use of the gas target were performed to guarantee that the target design was safe and effective. The most important factors to consider when using the gas target were limitations on beam current due to heating and structural failure of the target window and the effects of increasing the heat conduction of the target in order to determine the requirements for future deuterium and argon pumping systems.

The importance of heating and overall temperature was outlined in the preceding section but is discussed in more detail here. Heating of the gas cell components has three significant effects on NRR. First, heat can degrade the accelerator beamline vacuum due to offgassing from the foil and strongback to such an extent that the beam current must be reduced. Second, heat weakens the structural components of the gas cell, most specifically the thin windows, and can lead to catastrophic failure of the foil window. Lastly, heating of the deuterium gas itself decreases the density of the deuterium gas because the system is operated at constant pressure. This results in fewer deuteron molecules in the path of the deuteron beam and hence fewer neutrons are produced.

While the simulations of the gas target show that the heating in the gas window and the pressure on the window created by the deuterium gas should not exceed the failure points of the tungsten foils, experimental tests were undertaken to show that the gas cell would perform as expected [51]. Two experimental procedures were undertaken to demonstrate the feasibility of running high current into a high-pressure cell. First, the cell was pressurized and increasing current was directed into the cell to test the at-temperature strength of the foil windows. After the initial pressure testing was complete,

an infrared camera was used to characterize the temperature of the foil window, the strongback, and the surrounding target enclosure.

4.4.1 Pressure Testing

The gas cell was designed to sustain a pressure differential of at least 4 atm. To test the capability of the gas target and to estimate the maximum deuteron current that could safely be used for extended periods of time, the gas cells were pressure tested on the accelerator. The purpose of the pressure tests was three fold: First, to demonstrate the ability of the gas cell to withstand high pressure and high current, second, to evaluate the use of the beam scrapers to steer and center the beam, and finally, to determine the failure behavior of the foil window. Instead of using tungsten foils, however, a 5 μm thick stainless steel foil was used for the front gas cell windows along with a tungsten strongback. A stainless steel window was used instead of tungsten due to a limited supply of pinhole-free thin tungsten foils. Stainless steel is a good substitute in this test, however, as the strength and temperature properties of stainless steel are substantially worse than those of tungsten, indicating that the results shown here are conservative estimates of what the gas target can withstand. The gas cell was closed on the rear side with a 50 μm nickel foil, thick enough to stop the entire deuteron beam. It is expected that there will be no pressure differential on the rear end of the gas cell, so a thick foil was used to stop the beam to isolate the pressure effects on the front cell and ensure that we were able to accurately determine those effects.

For the pressure test, the deuterium chamber was pressurized with argon to a 2.4 atm differential. Argon was used as it is an inert and inexpensive gas; the lower pressure than the design is expected to tolerate was required due to the inferior structural properties of stainless steel. The argon beamstop housing was left off the target and only natural convection cooling was used. The temperature of the target was measured by attaching a thermocouple on the top of the aluminum target housing near the cooling fins to measure the temperature closest to the foil window, the hottest portion of the target. The current was measured on all four beam scrapers and the target module, the temperature was measured on the top of the aluminum housing, and the pressures of the

118

accelerator beamline and the internal target pressure were measured to quantify any pressure increase in the deuterium chamber due to assembly heating or leaking of gas into the accelerator beamline. These quantities were all measured as the deuteron beam current was increased, shown in Table 4.5.

Table 4.5: Results of pressure testing

Target (μA)	Top Scraper (μA)	Right Scraper (μA)	Bottom Scraper (μA)	Left Scraper (μA)	Gas Chamber (psi)	Beamline Pressure (Torr)	Temperature (°C)
0	0	0	0	0	20	1.72e-7	23.3
1.2	0	0	0	0	19.5	2.6e-7	25.6
3.5	0	0	0	0	19.5	2.58e-7	29.4
6.2	0.03	0.04	0.04	0	19.5	3.01e-7	36.1
8.9	0.04	0.05	0.03	0.05	19.5	3.82e-7	42.2
10.7	0.10	0.05	0.12	0.08	19.5	5.92e-7	50.6
12.8	0.08	0.06	0.25	0.06	19.5	1.04e-6	58.3
15.5	0.15	0.08	0.12	0.04	19.5	1.10e-6	63.9
18.1	0.18	0.11	0.22	0	19.5	1.13e-6	70.0
20.0	0.20	0.13	0.31	0.10	19.5	1.17e-6	76.1
23.0	0	0.25	0	0.20	19.5	1.26e-6	89.4
26.1	0.04	0.30	*	*	*	*	93.9

* Results unavailable due to foil failure

This experiment demonstrated several important factors concerning the gas target. As seen from the results in Table 4.5, the beam transport down the tube and into the target chamber is quite good. Even at elevated beam current, over 98% of the beam was focused onto the target. Additionally, in most of the cases, the currents measured on the top and bottom beam scrapers are similar, while those measured on the right and left scrapers are also similar. This indicates that the beam is well centered and has retained the slightly elongated shape seen in Figure 4.3, as illustrated by the higher current measured on the vertical beam scrapers relative to the current on the horizontal scrapers. Secondly, target temperatures, although high, did not noticeably deteriorate the beamline pressure. As the current was raised to 26.1 μA, the beamline pressure was seen to slowly rise. This is likely due to degradation of the accelerator vacuum by heat and offgassing from the stainless steel foil and the tungsten window, as this behavior was also noticed

when stainless steel was used as the target material in the gamma spectroscopy experiments. At 26.1 μA, however, the pressure in the accelerator beamline rose above the level at which the accelerator can operate and could not be lowered. At the same time the beamline pressure was seen to increase, the target chamber pressure began to decrease. It was realized that a target failure had occurred. Once this was realized, the experiment was terminated. It is important to note that although the target had failed, the mechanism of failure was slow enough to allow the operators to close a gate valve to isolate the target from the accelerator beamline, and thus to maintain operating vacuum in the high voltage section of the machine and bring the entire system down without any other components being affected. This has positive implications for use in an environment when safety and control is paramount, even during unexpected failures.

Closer inspection of the target upon removal from the accelerator indicated that softening of the Viton O-ring had occurred. Although it is impossible to determine exact temperatures, based on the properties of Viton, the target foil was likely subjected to temperatures in excess of 206°C. Small pinholes were also evident on the foil. Thus, the failure mechanism postulated was verified, and as long as the temperature of the O-ring is kept below its maximum operating temperature and strong, pinhole-free foils are used as target windows, the gas cell should maintain high pressure and high current for extended periods of time.

4.4.2 Temperature Characteristics

Following the pressure tests and initial functional testing of the gas target on the accelerator, a series of measurements were made using an infrared camera from FLIR Systems™, Inc. (ThermaCam® P65) to record the temperature distribution on the target windows and strongbacks [55]. The temperatures observed were used to correlate experimental results with simulations of the gas target to verify that the edges of the foil would not exceed the failure limit for the Viton O-rings used to seal the gas cell. The infrared camera was able to measure temperatures up to 580 °C with 0.3 mm spatial resolution and 0.1 °C temperature resolution. A front surface mirror was used for imaging to avoid placing the camera directly in line with the deuteron beam. For the

temperature experiments, 5 µm thin tungsten foils and the front strongback were used on both the entrance and exit windows of the gas target (see Figure 4.24).

The absolute temperature calibration for the images is dependent on the emissivity of the material, while the emissivity of a material is dependent on the temperature and surface condition. To accurately measure the temperature of the foils and strongback, a measurement of the emissivity was made following the irradiation of the gas cell. The irradiated front tungsten window was used to measure the emissivity, as the window had been subjected to high heat loading with resulting oxidation. These characteristics are a significant factor in the emissivity of the foil; using a fresh, unirradiated foil would have resulted in incorrect emissivity values. Estimates based on these measurements were used to assign emissivity values for all temperature measurements.

The foil was removed from the target after irradiation and affixed to a steel plate using carbon conductive tape. Sufficient adhesive was left on the edges of the foil as a reference point for the emissivity calculation since the emissivity of the tape is nearly one. The plate was then placed on an electrically controlled hot plate and heated to a uniform temperature. An infrared image of the plate, foil, and tape is shown in Figure 4.28.
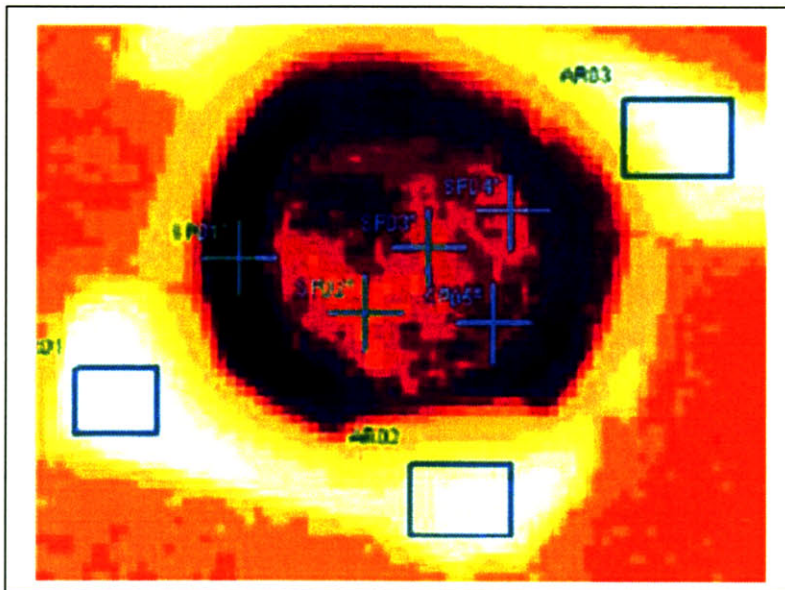
Figure 4.28: Emissivity calculation using irradiated tungsten foil

121

In this figure, the bright white spots are the carbon conductive tape and the purple area is the irradiated tungsten foil, all held at approximately 160 °C. As the plate, foil, and tape are all at a uniform temperature, the chosen emissivity of the foil can be varied such that the temperature of the foil in the image is equal to that recorded in the region of the carbon tape. The three boxed areas were used to get an average plate/foil/tape measurement to use as a reference, as the emissivity of those areas is known to be one. Five spots on the tungsten foil were used to calculate the emissivity. These spots were chosen due to high variation in oxidation and appearance of the foil to span a broad range of emissivities. Based on the reference points, the emissivities calculated for the various points on the foil are: SP01 - 0.20, SP02 - 0.71, SP03 - 0.58, SP04 - 0.53, SP05 - 0.38. The high emissivities values observed for spot #2, #3, and #4 are likely due to the higher oxidation levels which occur when hot tungsten reacts with air. For the following experiments, the temperatures were calibrated using an emissivity of 0.5 for tungsten, as the foil would be somewhat less oxidized than it was for the emissivity calibration. The error in the peak foil temperature at the highest beam current is estimated at about 5% due to uncertainty in the calculations of emissivity.

Experiments were next undertaken to characterize the thermal behavior of the gas cell when struck by a deuteron beam. The temperature of the front and rear window foils and strongbacks, the rate of heating and thermal equilibration, and temperature dependence on beam current were investigated. The gas cell was left open to air and the argon chamber removed for all the tests. The first experiment was designed to measure the temperature of the rear strongback and foil. The infrared camera was focused on the image of the rear strongback in the mirror. The camera was set to record an image of the foil and strongback every 20 seconds. A 5 µA beam of 2.5MeV deuterons was run through the gas cell and the resulting temperature rise on the rear strongback was measured. No cooling mechanism was applied. A representative image of the strongback is shown in Figure 4.29. Unfortunately, the beam tube was not centered correctly, so the beam impinges on the foil slightly higher than the center of the target in the vertical direction.

122
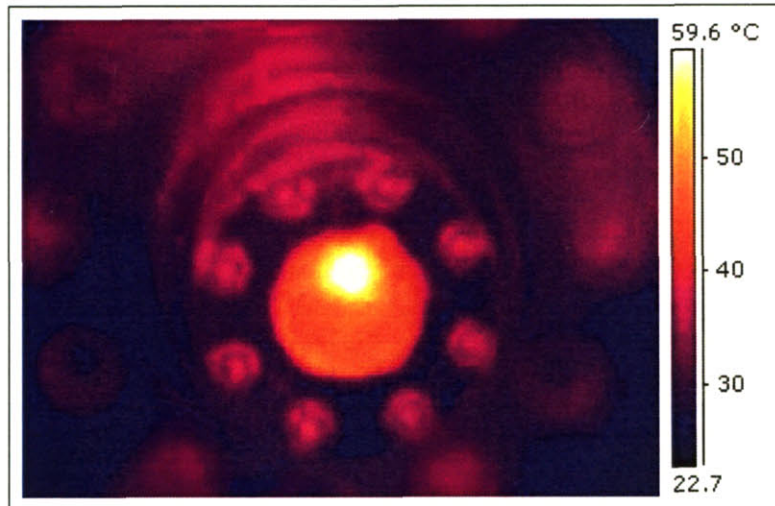
Figure 4.29: Rear strongback and foil at equilibrium under a 5 µA deuteron beam

In this image, two things are apparent. First, the temperature difference between the strongback and the foils is noticeable, as the lattice structure of the strongback is discernable in the infrared image. The second important point from this image is that the beam, although not centered uniformly in the gas cell, is shaped nicely into a circle of approximately 1 cm by the scrapers. The foil is hottest in the area where the beam hits, approximately 64 °C, while the rest of the foil is held at an approximate temperature of 35 °C. These temperatures did not change noticeably over the course of the 10 minute irradiation period, indicating that the equilibrium temperature of the foil under constant irradiation is stable.

The front foil window is expected to be the most critical component of the target. It operates at a higher pressure differential than the back window and the consequences of failure are potentially greater since they involve leakage of gas into the accelerator. Experiments to characterize the front window thermal behavior were therefore more extensive than those for the back window. In addition to the argon beam stop housing, the rear foil and strongback were also removed, allowing full view of the front foil through the empty gas cell. In this case, the foil was facing the camera so the strongback was not visible. Forced air was directed onto the outside of the housing of the gas cell at the location of the front foil as a cooling mechanism to approximate the argon cooling that would be present in a complete gas target assembly.

123

Temperature measurements of the front foil were taken to characterize the temperature dependence on beam current and to establish the rate of temperature increase and stabilization of the foil. A beam of 2.5 MeV deuterons was used for these experiments, beginning with a beam current of 5 µA. Infrared images of the front foil were recorded at 10 second intervals for beam currents up to 35 µA in 5 µA steps. Again, the beam was not distributed evenly over the foil and appears to be high in the images. Figure 4.30 below shows a typical image of the foil under irradiation with a 35 µA deuteron beam, using an emissivity value of 0.5.
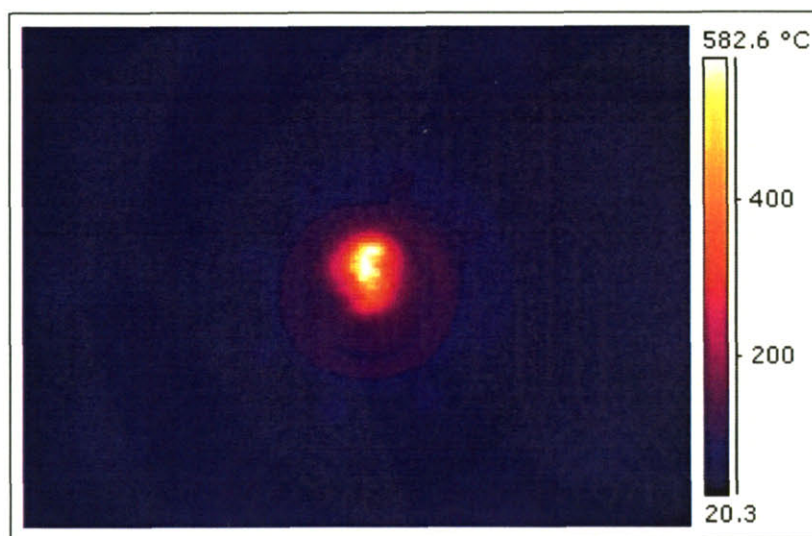
Figure 4.30: Infrared image of front foil (35 µA beam)

Figure 4.30 shows the asymmetrical heating due to the off-center position of the beam on the foil. Although this results in higher temperatures in the immediate area surrounding the beam, the relatively limited area of heating around the beam spot suggests that, once the beam is fully centered, the O-ring will not reach temperatures higher than its melting point as the heat from the beam spot does not spread quickly throughout the foil. As melting of the O-ring is the likeliest short-term pathway for gas cell failure, the ability to sustain a beam current of 35 µA with an off-center beam is indicative that the target will withstand even higher currents. The maximum temperature of the foil at 35 µA exceeded the temperature range of the infrared camera, although by

124

no more than 15 °C. The maximum temperature recorded in the center of the beam spot was 552 °C at 35 μA; the average temperature of the hottest portion of the beam spot was 530 °C. These values are significantly lower than the melting point of tungsten, and are very close to the temperature calculated in simulations [51].

The rate of temperature rise and equilibration of the foil is shown in Figure 4.31.
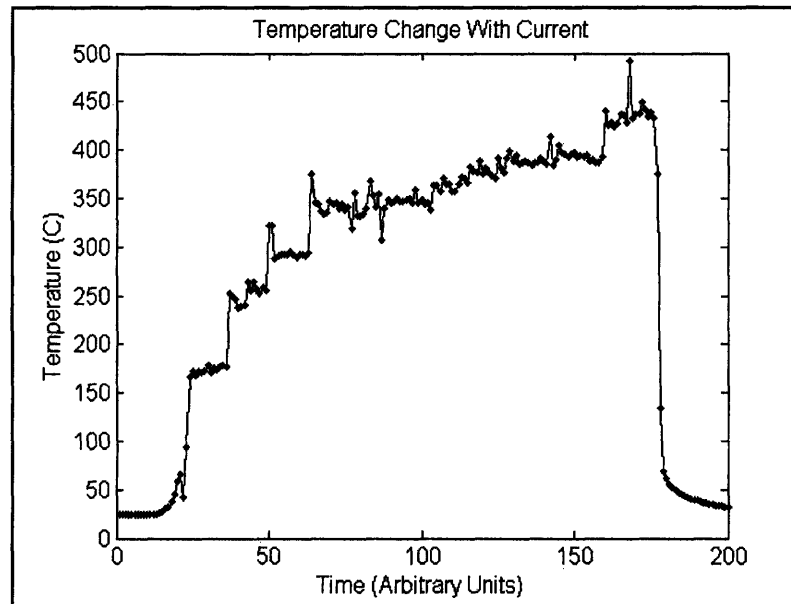
Figure 4.31: Foil temperature rise for beam currents of 5 – 35 μA

Each point in this figure represents the average temperature of the beam spot. The average temperature is plotted as a function of time (arbitrary start), with a measurement made every ten seconds. The "steps" evident in this figure indicate regions where the beam current was increased by 5 μA. These plateaus clearly show that the time required for the foil to come to an equilibrium temperature is less than 10 seconds. In the case of lower beam currents, from 5 – 25 μA, the current was increased every two minutes. Once the current reach 25 μA, however, the beam current was allowed to slowly rise over a period of 20 minutes to 30 μA before being increased to 35 μA at the end of the experiment. This was done to determine if the foil could withstand high currents for an extended period of time.

The measured temperature of the foil was also compared to the theoretically expected temperatures derived from ADINA™ simulations. These measurements were made to determine the effect of increasing current on the foil temperature. Figure 4.32 shows the temperature of the foil as a function of current compared to the simulated values.
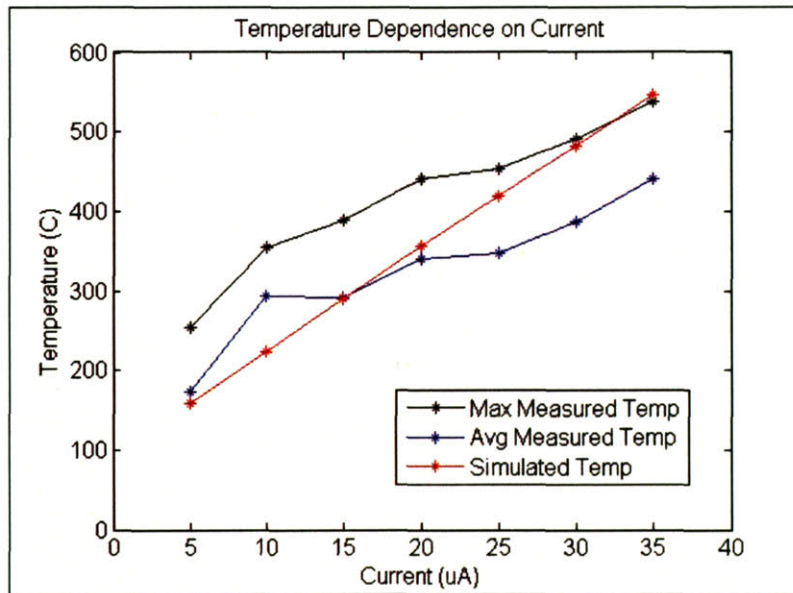
Figure 4.32: Temperature measurement compared to simulations

Figure 4.32 displays the maximum temperature of the foil, the average temperature of the foil in the most intense portion of the beam spot, and the theoretical maximum temperature of the foil from ADINA™ simulations [51]. This comparison shows that the temperature rise with current is fairly linear, as expected. The measured temperatures correspond well to the simulation results, even though the beam was not fully centered correctly and the heat distribution therefore not uniform. Finally, the temperature of the foil at the edges where there is contact with the Viton O-ring do not show an increase in temperature sufficient to warrant any concern over melting of the O-ring. The maximum temperature of the foil at the outer edges is less than 100 °C, below the melting point of Viton by approximately 100 degrees. These results make us confident that the tungsten foils can withstand the high currents required for high neutron production required for NRR.

126

4.5   Gas Target, Version 2.0

All systems benefit from the information gained by extended use, leading to improvements in design. While the gas target as described in this chapter did provide the desired neutrons without catastrophic failure, a number of difficulties were encountered in practice that were not apparent in initial tests or simulations. The solutions to these problems are simple, but must be incorporated into future gas targets.

First and foremost, the use of argon as the beamstop/cooling gas, despite its seemingly favorable properties, has a serious flaw that was not immediately realized – the ^{40}Ar(d,n)^{41}K reaction has a relatively high cross-section, close to one 1 mb [56]. As a fair number of deuterons must be stopped by the argon, this reaction results in a large number of neutrons produced that are not of the desired energy. In fact, up to a third of the total neutrons produced by the gas target are from reactions with argon. To remedy this situation, the argon must either be replaced by a different gas or the back foil must be thickened to act as a metal beamstop. Few gases are as available as argon: the gas must be inert, have few interactions with neutrons or deuterons, and be inexpensive and readily available. The most expedient solution was to replace the thin tungsten back window and wide-holed strongback with a 25 μm foil and a small-holed front strongback to better support the foil at the high temperatures induced by stopping the entire remaining beam. Note that there is no reason to use the strongback with larger holes, since it was intended to maximize transmission of the beam to the argon. Tungsten produces relatively few gamma rays, especially with slower deuterons, and the increased gamma flux from the metal beamstop proved to be much less a problem in the NRR imaging process than the undesired radiation produced in argon. The argon gas flow was retained as a cooling mechanism.

A second important issue was the deuterium gas cell. To ensure the purity of the deuterium, the cell was evacuated with a vacuum pump and refilled with deuterium gas prior to each use. The purge had to be handled with extreme care as the back foil was unsupported against a vacuum in the gas cell, which can lead to an "implosion" of the back foil if the beam stop pressure exceeds that of the gas cell. Despite precautions,

127

several foils were destroyed in this way. Future gas targets must incorporate a flow-through system for the deuterium by adding a second deuterium outlet to the gas cell. This serves a number of purposes. First, it addresses the problem of foil implosion during purging by eliminated the need to evacuate the cell. Second, flow-though of the deuterium ensures the purity of the gas and removes the ^{3}He that is produced by the D(d,n)^{3}He reaction. If a recirculating deuterium gas system is implemented, two further benefits can be realized. Deuterium gas density can be better maintained at high beam power densities by reducing the average gas temperature in the cell. Finally, flowing the deuterium through the cell will provide an addition means of cooling the cell, as the movement of the gas past the heated components of the target will carry away some of the heat. These issues must be addressed in future iterations of the gas target.

4.6 Chapter Summary

A new deuterium gas target was designed for neutron production for NRR. The target was designed to produce a neutron flux 6.6 x 10^7 neutrons/sr/μA/s at 0°, reducing to 7.2 x 10^6 neutrons/sr/μA/s at 90° to the neutron beam. The gas target incorporates a tungsten-lined deuterium gas cell designed to contain at least 4 atm of deuterium gas. The gas cell is closed on either end by thin, 5 μm tungsten foils, supported by thick tungsten strongbacks. The strongbacks, patterned with a hexagonal structure that allows for 60-80% transmission of the deuteron beam, facilitate strengthening of the gas cell to support high pressures and high currents. The gas cell is constructed out of aluminum, with three cylindrical cooling fins to assist in cooling of the gas chamber. The gas target also includes a beam scraper/shaper assembly upstream from the gas cell. The scraper assembly consists of four tungsten plates arranged so that a 1 cm diameter hole forms in the middle of the beamtube through which the deuteron beam passes. The scrapers remove the outer edge of the deuteron beam, shaping the beam into a 1 cm diameter circle. Current is measured individually on each of the four tungsten plates, ensuring that the beam is properly centered on the target. Finally, the deuteron beam is stopped in a cooled, recirculating argon beamstop. The argon serves to help cool the gas cell assembly as well as stop the deuterons which do not interact with the deuteron gas and

exit through the rear of the gas cell. Argon is recirculated at a pressure of 4 atm at 4 scfm to remove heat and stop the beam.

It has been determined that gamma interactions in the scintillating material used for neutron detection has detrimental effects on elemental determination. Gamma spectroscopy experiments were performed to determine the gamma flux emanating from various materials irradiated by 2.5 MeV deuterons. Seven metals were tested: stainless steel, molybdenum, nickel, tungsten, machinable tungsten, iron, and gold. Stainless steel produces by far the most gamma rays, both in terms of overall number and those of highest energy. Pure tungsten and gold produced the fewest gamma rays overall, with few high-energy gamma rays. Because of its other beneficial properties such as its strength and high melting point, tungsten was chosen as the material for use in the gas cell foil windows, strongbacks, and beam scrapers. The gas cell was also lined with tungsten thick enough to stop any penetrating deuterons. This ensured that all surfaces facing the deuteron beam were composed of tungsten, reducing the number of gamma rays produced.

The heating of the gas cell foil windows was also measured. Using a FLIR Systems™, Inc., infrared camera, the temperature of the rear strongback and foil window was measured under a deuteron beam of 5 μA. As expected, the temperature difference between the strongback and the window was apparent. The temperature of the front foil as a function of beam current was also measured. The beam current was increased from 0 to 35 μA in 5 μA increments and the maximum temperature and the average temperature of the beam spot were recorded. Again, as expected, the foil temperature increased linearly with current to a maximum temperature of approximately 580 °C at 35 μA. The temperature measurements of the foil closely matched those calculated by heat transfer simulation codes. Most importantly, the temperature measurements of the foil proved that the thin tungsten foils can withstand high deuteron beam currents without failure. Significant temperature increase is confined to the area immediately around the deuteron beam, with the edges of the foil reaching no more than 100 °C, much lower than the melting point of the Viton O-rings which seal the gas cell. As the primary failure point of the gas cell is by excessive heating, either of the tungsten window or melting of

the O-ring seal, these temperature measurements show that the gas cell can sustain the desired beam currents for high-flux neutron production.

5 Neutron Detection System

Detection of neutrons, especially fast neutrons, is quite difficult; preserving the spatial location of those detected neutrons is harder still. The neutron detection system used for NRR was outlined briefly in Section 2.4. It consists of a neutron-photon converter, a lens, and a CCD camera. Secondary radiation is produced in the scintillator during neutron interactions; this light is subsequently focused onto a CCD chip by means of a lens to create a digital image of the object under investigation. The creation of a clear, well-resolved image is essential for the successful determination of elemental composition using spatially resolved imaging techniques.

Because of the importance of neutron detection and imaging to the feasibility of NRR, this chapter is devoted to examining the quality of the imaging system, especially the scintillator and the CCD camera. The characteristics of the CCD camera, including the read noise, dark current, dynamic range, and spatial resolution are discussed in detail. The imaging setup and handling system are also described.

5.1 Imaging Setup

The CCD camera is very sensitive to external light since the amount of light produced by the neutrons is low and easily overwhelmed. The entire imaging system is enclosed in a light-tight box to reduce outside light contamination. The box made for the scintillator and camera system was 12 inches wide by 15 inches long and 36 inches high. The CCD camera and lens were sealed in the bottom of the box and the box was placed vertically facing the accelerator. A schematic of system was shown in Figure 2.4.

The inside of the box was painted flat black to diminish any reflected light and sealed with black tape. The scintillator was placed vertically at the top of the box facing the object of interest. Behind the scintillator, a 10 inch by 12 inch reflective mirror was placed at a 45° angle to the scintillator to reflect light to the lens below. It is necessary to reflect light from the scintillator with the mirror, as placing the CCD camera directly behind the scintillator would expose the CCD chip to damaging neutrons. The mirror,

however, is unaffected by the radiation field and the placement of the CCD camera helps to protect the camera and make the imaging apparatus stable and portable.

5.2 Optical System

An optical lens is mounted on the CCD camera and used to focus the light produced by the scintillator onto the CCD chip. The performance of the CCD camera and the focusing lens contribute significantly to the creation of well-resolved images with a high signal-to-noise ratio. There is a significant amount of light lost through the minification of the image by the lens and the quantum efficiency of the CCD camera. Additionally, the variety of noise inherent to the CCD camera substantially increases the requirement on the neutron flux.

5.2.1 Lens

A single lens can be described by two parameters, the focal length, f, and the F-number. The F-number, or the ratio of the focal length to the diameter of the lens, is a measure of the amount of light that can be collected by the lens. In other words, a lens with a larger diameter can collect more light and has a lower F-number. The lens that was used to focus the image onto the CCD chip was from Nikon, with a focal length of 50 mm, a diameter of 42 mm, and an F-number of 1.2.

The equation describing a single lens is as follows:

$$\frac{1}{S_0} + \frac{1}{S_1} = \frac{1}{f}$$

Eq. 5.1

where f is the focal length of the lens and S_0 and S_1 are the distance between the lens and the scintillator and the lens and the camera, respectively, as shown in Figure 2.4. As the lens focuses the light from the scintillator onto the CCD chip, the image is minified. The minification can be described by:

$$m = \frac{H_0}{H_1} = \frac{S_0}{S_1}$$

Eq. 5.2

132

where H_0 is the height of the object and H_I the height of the image. Using Eq. 5.1, the source-lens distance can be defined as a function of the focal length and minification, or object and image height:

$$S_0 = (1+m) \cdot f$$

Eq. 5.3

The lens has a sizeable effect on the amount of light that is finally focused from the scintillator onto the CCD camera chip [57]. The minification of the image results in a significant amount of light loss. For a Lambertian light source such as a ZnS(Ag) screen, the light lost through the lens is a function of the F-number and the minification of the lens:

$$L = \frac{1}{4F^2(1+m)^2 + 1}$$

Eq. 5.4

where F is the F-number, m is the minification, and L is the fraction of light captured by the lens [57]. For a non-Lambertian light source that can be measured as a point source, such as plastic scintillator, the fraction of light captured by the lens is given by:

$$L = \frac{1}{16F^2(1+m)^2 n_s^2}$$

Eq. 5.5

where n_s is the index of refraction of the scintillator (typically 1.58 for the scintillators used here – see Table 2.1). From these equations, it is clear that a smaller F-number and a smaller minification ratio lead to more light capture. A summary of the key properties of the lens is offered in Table 5.1.

Table 5.1: Nikon F/1.2 lens properties

Optical System and Lens Properties	
Diameter (d)	42 mm
F-Number (F)	1.2
Focal length (f)	50 mm
Minification (m)	9.2
Fraction of light collected for Lambertian source (L)	1.7×10^{-3}
Fraction of light collected for point source (L)	1.7×10^{-4}

Use of a lens to focus the light from the scintillator is obviously a major drawback for NRR. The magnitude of the loss of light through the optical system, when coupled with the low detection efficiency of the neutron detectors, places highly restrictive lower limits on the required neutron flux.

5.2.2 CCD Camera

The CCD camera used in the NRR experiments described in this thesis was an Apogee Instruments, Inc., Alta U9 camera. The CCD array is an Eastman Kodak Company KAF-6303E, 3072 x 2048 pixels (27.65 x 18.43 mm), with each pixel 9 x 9 μm. The high resolution of this CCD camera is not required for NRR, but there is the ability to bin the pixels such that an adequate level of signal is received without sacrificing significant resolution of the image. The ability to bin the camera up to 10 x 10 pixels prior to image readout is essential to NRR, as this increases the signal per "pixel" but does not introduce additional read noise.

The performance of any CCD camera in low-light situations depends primarily on the noise level in the system. There are multiple contributions to the noise level, including pattern noise, quantum noise, dark noise, and readout noise. Pattern noise is a fixed amount of noise due to manufacturing of the CCD chip and other system components. Quantum noise is the statistical noise dependent on the electron buildup in each charge well. Dark noise is due to the effects of temperature on the silicon CCD chip, while readout noise is the noise added when the charge of each pixel is "read" and recorded by the system. The dark noise can be reduced by cooling the CCD camera using the built-in thermoelectric cooler.

The noise level of the camera as a function of temperature was evaluated to determine an optimal operational temperature. While maximum cooling will reduce the dark current the maximum amount possible, it is not recommended to cool most CCD cameras more than 50 °C below room temperature due to the possibility of condensation

on the CCD chip[x]. A measurement of the dark current was taken in increments of 5 °C from 15 °C to -25 °C. Due to the extremely low dark current, the dark current integration times were 30 minutes each. The results are shown in Figure 5.1.
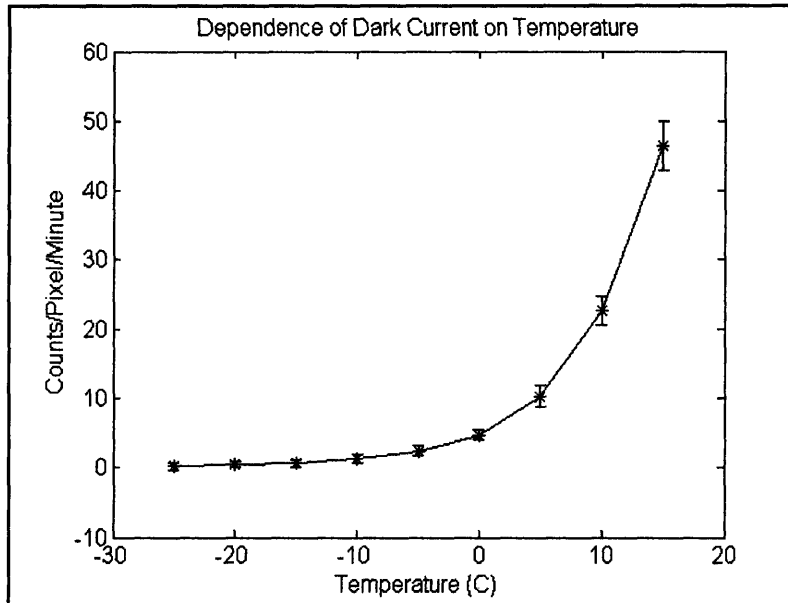
Figure 5.1: Dark current as a function of temperature

An operating temperature of -25 °C was chosen for the experiments described in this and subsequent chapters. This temperature was chosen because of the stability of the cooling system at this temperature, the extremely low dark current, and to account for the fact that the atmosphere of the room was not controlled. In case of temperature or humidity increase, we did not want the temperature of the camera to be readjusted to ensure no more than a 50 °C difference in temperature between the chip and the atmosphere.

To evaluate the performance of the CCD camera and establish an approximate value for the expected signal to noise ratio, the dark current and readout noise were first determined. These two sources of noise, along with the pattern noise, were subsequently

---

[x] Hard vacuum sealed cameras can be cooled more than 50 °C below ambient. The Apogee Instruments camera used in these experiments incorporated a sealed soft-vacuum chamber with argon backfill to reduce the maintenance associated with cooling and the low temperature limit was thus increased.

removed from all images. The readout noise and the dark noise were determined from a series of experiments comparing the average counts per pixel versus the variance in the image. All of the "images" described in this section were taken with the shutter closed, to measure only the effects of dark noise and readout noise. The number of electrons for any pixel over a fixed imaging time is given by:

$$N_{i,j} = n_{i,j} + n_{read}$$

Eq. 5.6

where $n_{i,j}$ is the actual signal[xi] and n_{read} is the fixed signal due to offsets and read counts. The statistical variance in the number of electrons detected is given by

$$\sigma^2 = \sigma_{i,j}^2 + \sigma_{read}^2$$

Eq. 5.7

As the variance $\sigma_{i,j}^2$ is simply equal to $n_{i,j}$, we are left with:

$$\sigma_{i,j}^2 = n_{i,j} + \sigma_{read}^2$$

Eq. 5.8

The analog-to-digital converter (ADC) converts the signal in electrons to digital counts with a gain G:

$$A = G \cdot n_{i,j}$$

Eq. 5.9

where G is in units of counts/electron.

To determine the variance in the system, the difference between two images is used. Two images are taken for the same amount of time, from one second to six minutes. A summary of all the relevant parameters of these images is given in Table 5.2.

[xi] In this case, the signal is due to dark current, whereas in images taken with the shutter open, the signal would be due to both the effects of dark current and of the true image signal.

Table 5.2: Properties of images used for determining gain and dark current

Exposure Time (min)	Average Counts/Sec	RMS	Variance
5 (Image 1)	2034.4 ± 16.79	19.781	195.723
5 (Image 2)	2034.5 ± 16.82		
10 (Image 1)	2036.0 ± 18.74	19.832	196.659
10 (Image 2)	2035.8 ± 18.77		
15 (Image 1)	2037.4 ± 19.37	19.890	197.817
15 (Image 2)	2037.3 ± 19.35		
20(Image 1)	2038.5 ± 20.28	19.980	199.608
20 (Image 2)	2038.8 ± 20.26		
30 (Image 1)	2042.6 ± 21.01	20.234	204.716
30 (Image 2)	2042.6 ± 22.00		
60 (Image 1)	2049.6 ± 28.74	21.178	224.262
60 (Image 2)	2049.9 ± 28.75		
90 (Image 1)	2057.8 ± 36.56	21.208	227.014
90 (Image 2)	2057.9 ± 36.51		
120 (Image 1)	2062.1 ± 45.30	21.866	239.067
120 (Image 2)	2062.1 ± 45.42		

The ADC counts per pixel in each image, using Eq. 5.6 and Eq. 5.9, can be written as:

$$A = G \cdot n_{i,j} + G \cdot n_{read}$$

$$B = G \cdot n'_{i,j} + G \cdot n'_{read}$$

Eq. 5.10

Subtracting the two images leaves us with

$$\Delta = A - B = G(n_{i,j} - n'_{i,j}) + G(n_{read} - n'_{read})$$

Eq. 5.11

Writing this in terms of the variance of the electron counts, we have

$$\sigma^2 = G^2(\sigma^2_{i,j} + \sigma'^2_{i,j}) + G^2(\sigma^2_{read} + \sigma'^2_{read})$$

$$= 2 \cdot G^2 \cdot \bar{\sigma}^2_{i,j} + 2 \cdot G^2 \cdot \bar{\sigma}^2_{read}$$

$$\frac{\sigma^2}{2} = G^2 \cdot \bar{n}_{i,j} + G^2 \cdot \bar{n}_{read}$$

$$= G \cdot C + G \cdot C_{read}$$

Eq. 5.12

where C is the average number of counts/pixel in the signal and C_{read} is the average number of counts/pixel due to read noise. As the differences in the variance of each pixel and of the read noise are negligible, the average values for the variances can be used in Eq. 5.12. In this case, the standard deviation of the image, σ^2, is a value that can be determined using the value of each pixel in images A and B. The mean of the image is given by the standard equation:

$$\bar{A} = \frac{\sum_{i,j} a_{i,j}}{N}$$

Eq. 5.13

where N is the number of pixels in the image and $a_{i,j}$ is the value of the pixel at location i,j. The root mean square of the pixel values can then be determined:

$$RMS = \left(\frac{\sum a^2_{i,j}}{N}\right)^{1/2}$$

Eq. 5.14

Finally, the standard deviation can be found:

$$\sigma^2 = \left[\left(\frac{\sum a^2_{i,j}}{N}\right) - \bar{A}^2\right]^{1/2}$$

Eq. 5.15

Thus, we can create a plot of half the variance as a function of average counts/pixel and fit a linear equation to the resulting points, the gain of the system is the slope of the line and the read noise is the intercept divided by the gain.

Before this plot can be created, however, the offset of the system must be determined. The offset of the system is the lowest value that the average counts/pixel can reach. This offset is found by plotting the average number of counts/pixel against the time of the image, using data from Table 5.2. A line can subsequently be fit to this data; the slope is the dark current (counts/pixel/sec) due to thermal motion while the intercept is the inherent offset of the system. Figure 5.2 shows the average counts/pixel against the integration time of the image with a linear fit.

138
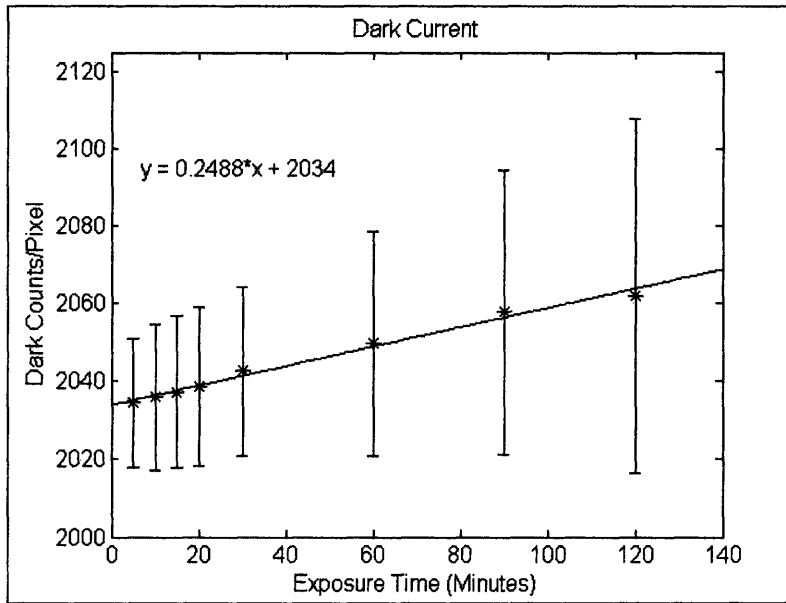
Figure 5.2: Average counts per pixel due to dark current at -25°C

From the slope of the line fit, we can determine that the dark current is approximately 0.004 counts/pixel/sec and the offset of the system is 2034 counts/pixel/sec. These two values will be subtracted from the final images to remove the signal due to dark current and the offset, leaving only the signal due to detected neutrons. A plot of the variance versus corrected average counts is shown in Figure 5.3. The slope of this line indicates that the gain is approximately 1.6 counts/electron, or about 0.625 electrons/count.
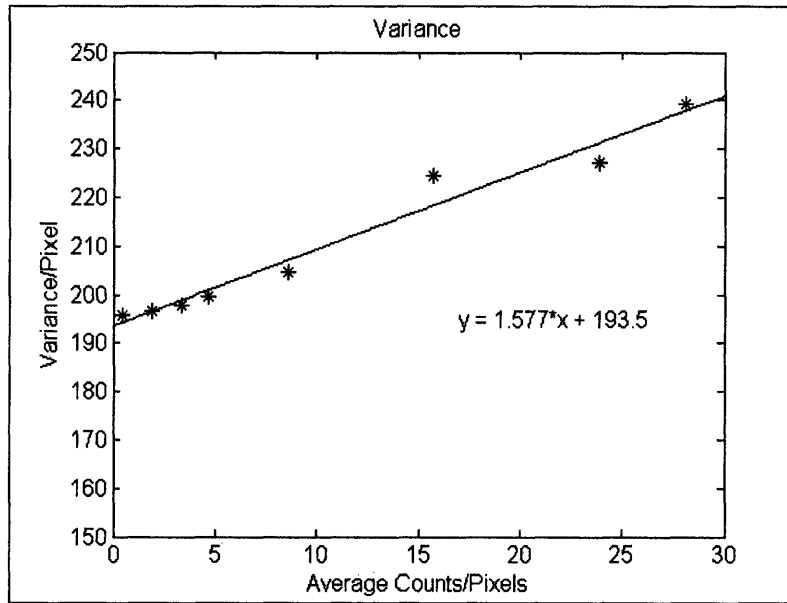
Figure 5.3: Calculation of the gain

While the above noise factors are all dependent to some extent on temperature, binning, and length of exposure, one factor that cannot be changed is the quantum efficiency of the CCD camera. The efficiency of all CCD chips is sensitive to the wavelength of light that is emitted by the scintillator. Shifting the light towards the red end of the optical spectrum generally results in higher efficiency. The quantum efficiency of the Apogee Alta U9 is shown in Figure 5.4. The quantum efficiency at the wavelengths that are emitted by the scintillators used in this thesis is approximately 0.3 − 0.4. Thus, regardless of the amount of light emitted by the scintillator and focused onto the CCD camera by the lens, an automatic 60 − 70% reduction in detected light occurs.
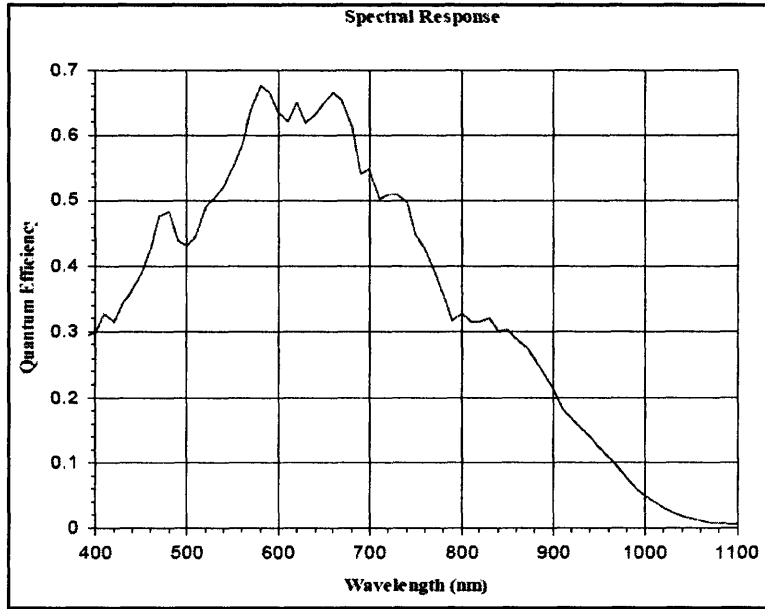
Figure 5.4: Quantum efficiency of Kodak KAF-6303E CCD chip [58].

5.3 Signal-to-Noise Ratio

The signal-to-noise ratio (SNR) is the definitive measure of the performance of the CCD camera. Maximizing the SNR provides a clearer image, allowing for superior elemental and spatial identification. The SNR can be expressed as a function of the incoming photon flux (Φ_{ph}), the dark current (Φ_{dark}), read noise (N_{read}), background flux ($\Phi_{background}$), quantum efficiency of the CCD (η_{CCD}) and the total integration time (t):

$$SNR = \frac{\Phi_{ph} \cdot \eta_{CCD} \cdot t}{\sqrt{(\Phi_{ph} + \Phi_{background}) \cdot \eta_{CCD} \cdot t + \Phi_{dark} \cdot t + N_{read}^2}}$$

Eq. 5.16

In this equation, the photon flux, background flux, and dark current are in terms of particles/pixel/second, while the read noise is expressed in terms of electron RMS/pixel at a given readout rate. The dark current and the read noise dominant in two separate regions. If exposure times are short, the read noise is dominate and Eq. 5.16 reduces to:

$$SNR = \frac{\Phi_{ph} \cdot \eta_{CCD} \cdot t}{N_{read}}$$

Eq. 5.17

141

If the exposure time is long, however, the dark current dominates, the read noise is negligible, and Eq. 5.16 reduces to:

$$SNR = \frac{\Phi_{ph} \cdot \eta_{CCD}}{\sqrt{(\Phi_{ph} + \Phi_{background}) \cdot \eta_{CCD} + \Phi_{dark}}} \sqrt{t}$$

Eq. 5.18

In the case of NRR, the background flux is negligible compared to the photon flux, and imaging times are long, enabling the use of a modified version of Eq. 5.18:

$$SNR = \frac{\Phi_{ph} \cdot \eta_{CCD}}{\sqrt{\Phi_{ph} \cdot \eta_{CCD} + \Phi_{dark}}} \sqrt{t}$$

Eq. 5.19

This equation can be rewritten as a function of SNR or of photon flux, which enables an operator to determine the required imaging time for a given photon flux and desired SNR, or to determine the SNR given constraints on imaging time and photon flux.

5.4 Light Collection Requirements

The previous sections in this chapter have discussed the light lost in each part of the optical system and the effects of system noise. As the amount of light finally collected and converted into a digital signal is the ultimate measure of the success of an NRR system, these light loss pathways should be discussed as a whole along with the constraints placed on the system due to the actual dark current and readout noise. The overall effect of these system limitations is discussed in this section.

The number of electrons generated in the CCD chip that are ultimately read and analyzed can be expressed by the following equation [28]:

$$N_e = \Phi_n \cdot A_p \cdot \eta_n \cdot g_1 \cdot g_2 \cdot \eta_{CCD}$$

Eq. 5.20

In this equation, Φ_n is the incident neutron flux (n/cm^2/s), A_p is the pixel area, η_n is the neutron detection efficiency of the neutron detector (either ZnS(Ag) or plastic scintillator), η_{CCD} is the quantum efficiency of the CCD camera, g_1 is the number of photons produced per detected neutron in the screen, and g_2 is the optical coupling efficiency of the lens. The quantum efficiency of the CCD camera (Figure 5.4) is 0.40 at

142

the wavelength of the scintillation photons. The neutron detection efficiency of the ZnS(Ag) screen is low, on the order of a few percent, while the efficiency of the plastic scintillator is higher at close to 20%. The number of photons produced by the scintillating screen per detected neutron is also given by the manufacturer of the screen. The number of photons produced is dependent on the energy that the detected neutron transfers to the screen; for our purposes, the percentage of emitted light energy compared to the absorbed energy is approximately 18%, or approximately 100,000 photons per detected neutron for ZnS(Ag), and on the order of a few thousand for plastic scintillator[59]. As previously discussed, the pixel area is 9 μm x 9 μm, although this number can be increased by binning the pixels to reduce the effect of read noise and increase the SNR. For the purposes of this section, however, no binning is assumed and the final result can be increased by the appropriate sizing factor in the event that the CCD camera is binned. The last limiting factor in this equation is the lens coupling efficiency, described in detail in Section 5.2.1. The light collection efficiency of the lens is 1.7×10^{-3} for a Lambertian source, and 1.7×10^{-4} for a point source. Combining the numerical value of these factors with Eq. 5.20 provides a lower bound on the required neutron flux:

$$N_e(Lambertian) = 1.1\times10^{-6} \cdot \Phi_n$$
$$N_e(Point) = 5.5\times10^{-8} \cdot \Phi_n$$

Eq. 5.21

This equation demonstrates the need for high neutron flux. In addition to the number of electrons produced by the incident neutrons, electrons are produced in the CCD chip by the dark current as well. Eq. 5.21 can also be written more definitively including the dark current:

$$N_n + N_{dark} = 2.8\times10^{-6} \cdot \Phi_n$$

Eq. 5.22

where N_n and N_{dark} are the number of electrons produced due to the neutron flux and dark current, respectively.

5.5 Chapter Summary

The performance of the CCD camera and optical system is essential to the success of NRR. The neutron detection system consists of a neutron scintillator, reflecting mirror, and lens-coupled CCD camera enclosed in a light-tight portable box. The lens used was a Nikon F/1.2 lens, with a light collection factor of 1.7×10^{-3} for a Lambertian light source and 1.7×10^{-4} for a point source. A lower F-number does not significantly change the fraction of light collected. The light loss due to lens coupling is a serious drawback for NRR using CCD cameras, as the flux from the initial neutron source must be high enough to overcome the light loss through the lens system.

The Apogee Alta U9 camera was chosen for its extremely low dark current, large chip size, and high quantum efficiency relative to other CCD cameras. The Kodak KAF-6303E chip is 3072 x 2048 pixels (27.65 x 18.43 mm), with 9 μm square pixels. The camera has the ability to bin on-chip, increasing the amount of signal per "pixel", and the small size of each pixel means that even a 10 x 10 bin results in camera-limited resolution of 0.09 mm, much better than that required. The dark current measured for the Apogee Alta U9 camera was 0.004 counts/sec/pixel at -25 °C, the bias at 2034 counts/sec/pixel, and the gain at 1.6 counts/electron.

6   Elemental Determination Using NRR

The previous chapters have described the components of a complete explosives detection system using fast neutrons. In this chapter, the results of experiments using these components are described. The experiments discussed here provide the experimental basis for evaluation of the use of NRR and its ability to identify elemental content of concealed objects.

Two sets of experiments were performed to show the principle of NRR and its ability to identify elemental content. The first set of experiments was undertaken at MIT, using the MIT LABA accelerator described in Section 4.1. The second set of experiments was performed at the MIT Bates Accelerator Laboratory with an RFQ accelerator that will be described later in this chapter. The goal of these experiments was to show the differences in the carbon attenuation coefficients at a number of neutron energies, as opposed to the invariant attenuation coefficients discuss in Chapter 3. Demonstration of variance in the attenuation coefficient of carbon, the only pure calibration material, is especially important for NRR to progress, as all other material identification ultimately depends on the values of the carbon attenuation coefficients.

6.1   Experiments Conducted at MIT LABA

The MIT LABA facility, as mentioned, is highly accessible and useful for neutron experiments given its location and layout. The MIT accelerator has been described in previous chapters. Beam port 1 (Figure 4.2) was again used for these experiments to provide the maximum possible rotation, and hence neutron spectra, around the neutron source. The experiments carried out with LABA accelerator were the first experimental demonstration of multiple-element using a D-D neutron source and CCD camera.

6.1.1 Experimental Setup

After extensive use of the gas target, the scrapers were sufficiently conditioned to allow for a constant 25 μA deuteron beam to be used[xii]. The gas target described in Chapter 4 was used as the monoenergetic neutron source. The gas cell was pressurized to 4 atm for all experiments and a steady argon flow of 2.5 scfm at a pressure of 3 atm was used to cool the gas target. Small-holed strongbacks were used on both the front and back window as supports for the thin foils. A 7 μm molybdenum thin foil was used for the front window, while a thick 25 μm tungsten foil was used for the back end as a beamstop to avoid neutron production via the $^{40}Ar(d,n)^{41}K$ reaction.

A serious drawback of the MIT facility is the size of the shielded vault that houses the end of the accelerator beamline. The concrete walls of the vault provide enough shielding for operators, but neutrons that interact with the shielding produce a 2.23 MeV gamma ray as well as slower neutrons. The proximity of the shielding walls to the accelerator beamline and neutron source inevitably leads to a significant gamma flux and off-energy neutron flux, as many of the neutrons that are produced in the gas target impact on the walls of the vault.

To reduce the number of neutrons that are able to reach the vault walls, a shielding system consisting of borated polyethylene was constructed around the gas target. A minimum of 30 cm of borated polyethylene was stacked around the gas target. Wedges of borated polyethylene were strategically placed around the target at the angles of interest for NRR; when removed, a 7.5 cm high slit was made to allow neutrons produced in the gas to escape the shielding. This system was designed to ensure that only neutrons of the desired energy were allowed to leave the gas target system. The advantage of using borated polyethylene is that most of the neutrons interacting with the shielding produce a 478 keV gamma ray through boron capture, rather than the 2.23 MeV gamma ray from hydrogen interactions. However, the gamma flux from both the boron capture and interactions with concrete and the hydrogen in the borated polyethylene is still high.

[xii] Here, "conditioning" is used to mean the period in which new components are broken in. Heating the scrapers burns any residue off the metal and allows the vacuum system to adjust to offgassing from various components. Repeated use removes more offgassing material; the longer a part is used, generally, the better the vacuum and the hotter the part can become before negatively affecting the vacuum.

In addition, although the switching magnet is useful for separating the deuterons of desired energy from any other particles produced in by the accelerator, the particles that are not directed to beam port 1 unavoidably interact with the material of the beamline and other beam ports. Given that the accelerator material is predominately stainless steel, these interactions create a large gamma ray flux. Thus, between the interactions with the accelerator beamline, neutron interactions in shielding material, and the gamma rays produced in the gas target from deuterons on tungsten, the gamma flux is quite large. Measurements of the neutron to gamma flux indicated that the number of gamma rays outnumber neutrons by a factor of ten to one.

6.1.2 Neutron Detection Apparatus

The high gamma ray flux in the vault precluded the use of plastic scintillator as a neutron detector; a 2.5 mm thick ZnS(Ag) screen was used instead. This screen is essentially gamma-blind, leaving light produced from neutron interactions the only source of light to reach the CCD camera. However, the low efficiency of the ZnS(Ag) screen dictated long imaging times.

The Apogee Alta U9 CCD camera described in Chapter 5 was used to record the neutron images. The camera was cooled to -25 °C. To protect the CCD camera from stray radiation, the camera was surrounded by lead and concrete to form a gamma ray and neutron shield. Four inches of lead bricks were placed on each side of the camera, reaching from the floor up twelve inches to the bottom of the box, almost completely enclosing the camera (a small opening was required for air flow for the camera cooling system). Outside of the lead, two layers of six inch wide concrete bricks were placed to stop any stray neutrons from reaching the CCD chip or electronics. The concrete blocks also reached twelve inches high.

As a test of the shielding, a 20 minute "image" was taken with the camera shutter closed with no neutron beam and another 20 minute image with the shutter closed but a 15 μm deuteron beam directed into the gas target. Any neutrons or gamma rays that reach the CCD chip when the beam is turned on should interact with the chip, exciting electrons and creating more counts per pixel in the final image. However, the second

image showed no significant difference in average counts or standard deviation than the first, "beam off" image, indicating that the lead and concrete adequately shielded the camera from most unwanted radiation.

An object stand was affixed to the outside of the CCD camera box. The stand was placed a distance of 0.5 m from the scintillator and fixed such that the objects under investigation were located in the center of the imaging plane. Keeping the object at the same point is especially important in NRR, where a pixel-by-pixel comparison between images must be made. By fixing the object stand to the CCD camera box, a stable platform guaranteed that the object was consistently in the same place for each image. The entire box and stand was rotated around the neutron source to take advantage of the various neutron energies. The total distance from the neutron source to the scintillator was 2.0 meters, resulting in an object magnification of 1.

6.1.2.1   Spatial Resolution of Imaging System

The spatial resolution that can be obtained in the final images is due to three main factors: the size of the original neutron beam, the light spread within the ZnS(Ag) screen, and the size of the pixels on the CCD chip or the size of the pixel binning. For explosives detection, the resolution requirements of the system are not demanding: resolution of a few millimeters is sufficient. The size of the neutron source is a minimum of 1 cm (the diameter of the deuteron beam), which, combined with Eq. 2.13, places a lower bound on the resolution of 5 mm. The CCD camera is binned at 8 x 8 for maximum light collection to reduce exposure time; the size of the binned pixels is 0.072 mm x 0.072 mm. According to Table 2.2, the light spread from the ZnS(Ag) scintillator is 1.36 mm. Thus, the limiting factor in resolution is the size of the neutron source.

A test of the system was performed to measure the resolution in a practical situation, rather than rely solely on theoretical values. Five holes, with diameters of 5.08 cm, 2.54 cm, 1.27 cm, 0.63 cm, and 0.31 cm, respectively, were drilled into a one-inch thick slab of polyethylene. The slab was placed in front of the camera at the same distance as subsequent objects – 1.5 meters from the neutron source and 0.5 meters from

the scintillator – at zero degrees relative to the target (4.89 MeV neutrons on average). The slab was then exposed to a 20 μA beam of neutrons for 30 minutes. The resulting image, shown in Figure 6.1, was background corrected and subjected to the same modified median filter to reduce speckling and show the maximum resolution possible with the imaging system[xiii]. As expected, the 0.63 cm-diameter hole is resolved clearly, while the 0.31 cm-diameter hole, while visible, is not, demonstrating that the imaging system has the ability to resolve objects as 0.6 mm, a key requirement for spatial imaging.
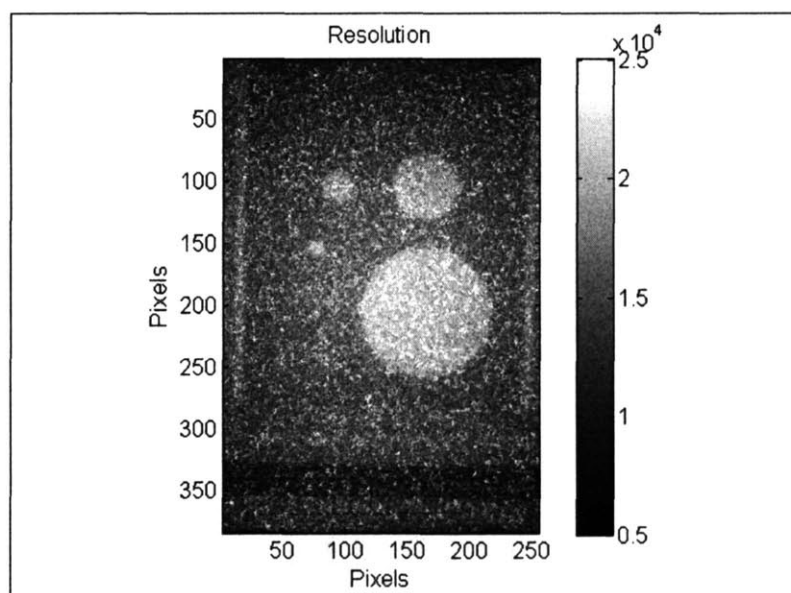
Figure 6.1: Image of one-inch thick polyethylene block with holes of varying diameter (5.08, 2.54, 1.27, 0.63, and 0.31 centimeters). The image was taken at 0 degrees (4.89 MeV neutrons) for an exposure time of 30 minutes. The source-to-object distance was 1.5 meters; the object-to-detector distance was 0.5 meters, resulting in a magnification of 1.5. The dark lines across the bottom of the image is the object platform

---

[xiii] The image processing software used was MaximDL from Cyanogen, provided with the CCD camera by Apogee Instruments, Inc. The background subtraction is a built-in system of the MaximDL software, but the modified median filter was written specifically for this application and implemented in MatLab™.

149

6.1.3 Carbon Attenuation Using Image Averages

A large carbon block was used to measure the carbon attenuation coefficients. The block was rectangular, with dimensions of 9.5 cm wide by 14 cm high by 7 cm thick (5.5 in x 3.75 in x 2.75 in). The thickness was enough to affect a significant amount of the beam (at least 40%) at all neutron energies, but not thick enough to attenuate the entire beam. The density of the carbon block was measured to be 1.68 g/cm^3, slightly less than the theoretical carbon density of 1.77 g/cm^3.

Four neutron energies were chosen that represented the most disparate values in the carbon cross-section, and hence should have resulted in the largest variation in the measured attenuation of the neutron beam. The neutron energies chosen were 4.89, 4.74, 4.12, and 3.15 MeV, corresponding to angles of 0°, 20°, 48°, and 80° relative to the gas target. These energies are average values, given that 4 atm of deuterium gas contributes approximately 440 keV of energy spread to the neutron beam. The averaged carbon cross-section at these neutron energies are 1.307, 1.47 1.95, and 1.85 barns for 4.89, 4.74, 4.12, and 3.15 MeV neutrons, respectively. The theoretical attenuation coefficients are found, using Eq. 2.1, to be 0.066, 0.074, 0.098, and 0.093.

Two images were taken at each angle: one open beam image with no object and a second image of the carbon block. The camera was binned 2 x 2 on chip to reduce speckling and cosmic ray interactions, and then subsequently binned by hand to 8 x 8 to increase the signal per pixel. At 0° and 20°, the neutron flux is largest, and 30 minutes of imaging time was sufficient to obtain good images. The final images were made of ten minute images added together to reduce the speckling and interference from stray particles and cosmic rays. This method is useful for image processing, but adds a small amount of noise to each final image from the additional read noise that results from taking multiple images. However, this noise is small, on the order of 15 counts/pixel, and the added benefit of fewer speckles in the image compensates for the additional noise.

Each 10-minute image was despeckled according to the process outlined in Section 2.5.3. A background image was subtracted from each 10 minute image, the series of images were combined and normalized to total current, and each pixel in the carbon image was divided by the corresponding pixel in the open beam image to determine the attenuation of the neutron beam due to the carbon block. Background-

corrected, normalized composite images of the open beam and carbon block at 0° are shown in Figure 6.2. An example image of the attenuation due to the carbon block is shown in Figure 6.3 (The slight tilt in the images is due to a small rotation of the camera).
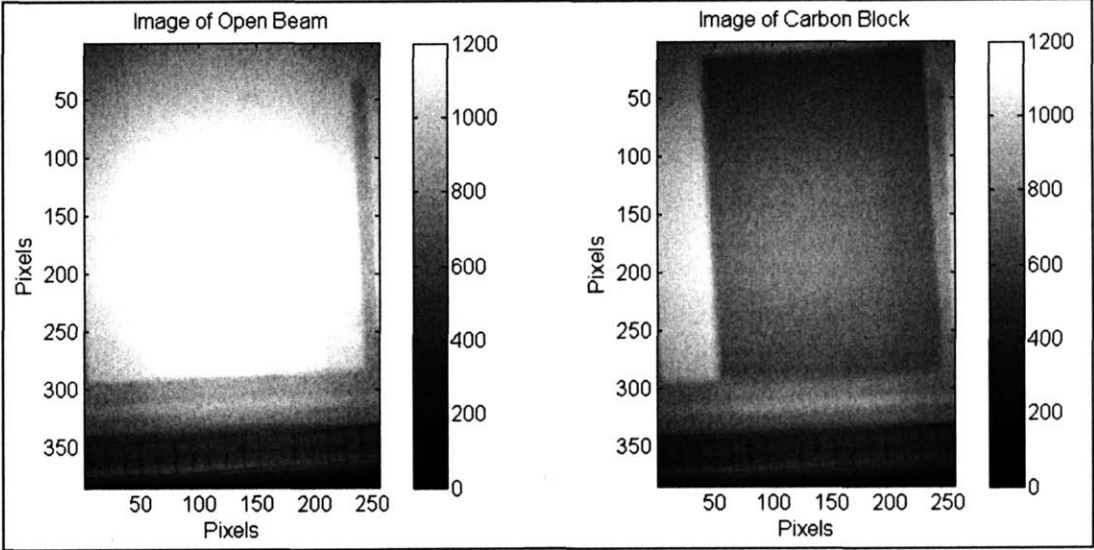
Figure 6.2: Open beam and carbon block images at 0°
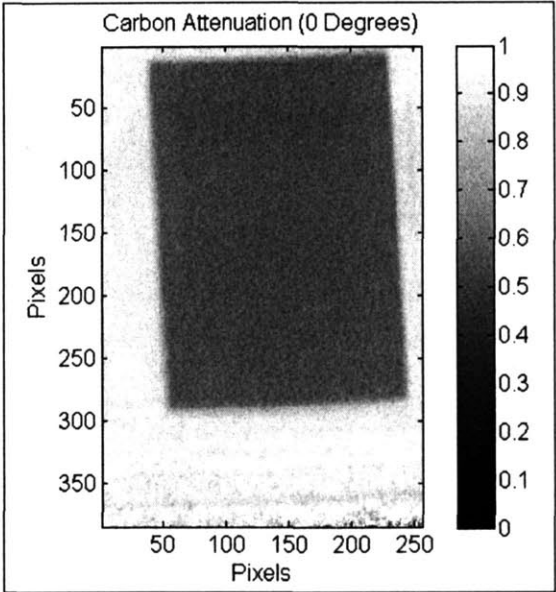
Figure 6.3: Attenuation due to carbon block at 0° (I/I_0)

A sizable box, 100 by 100 pixels, and encompassing the center of the carbon block was used to find the average of the attenuation. A table of the calculated attenuation coefficients is shown in Table 6.1 along with the expected values, for the four angles analyzed here.

Table 6.1: Measured and expected attenuation coefficients

Angle/ Energy (degrees/ MeV)	Measured Value (cm^2/g)	Expected Value (cm^2/g)
0/ 4.89	0.0529 ± 0.0013	0.066
20/ 4.74	0.0422 ± 0.0022	0.074
48/ 4.12	0.0636 ± 0.0043	0.098
80/ 3.15	0.0526 ± 0.0063	0.093

6.1.4 Carbon Attenuation Using Median Value

It is clear from Table 6.1 and the preceding analysis that the attenuation coefficients evaluated from the carbon images made by despeckling, or replacing pixel values with the median of its neighbors, do not match the expected attenuation coefficients. A second evaluation technique was used that did not involve despeckling to determine the attenuation coefficients. The despeckling, as noted above, creates an artificial average that is not necessarily representative of the overall attenuation. This second technique obviates the need for despeckling, but is not as useful for imaging. The aim was to determine what the true carbon attenuation was for the purpose of proving the physics, rather than attempting the more difficult task of image analysis. This method, even if it could show reasonable correlation of expected attenuation values with the measured values, would not be very useful for NRR, as the imaging method relies on the ability to determine the elemental content of each pixel, rather than the entire image. In short, this method was intended solely to determine if something approximating the expected differences in carbon attenuation at different neutron energies could be extracted from the CCD camera information.

For each angle (neutron energy), the "dark" image was subtracted from the carbon image and the open image. The resulting dark-corrected images were normalized to

beam current, and each pixel in the carbon image was divided by the corresponding pixel in the open image. The result was a "speckled" attenuation image, as shown below.
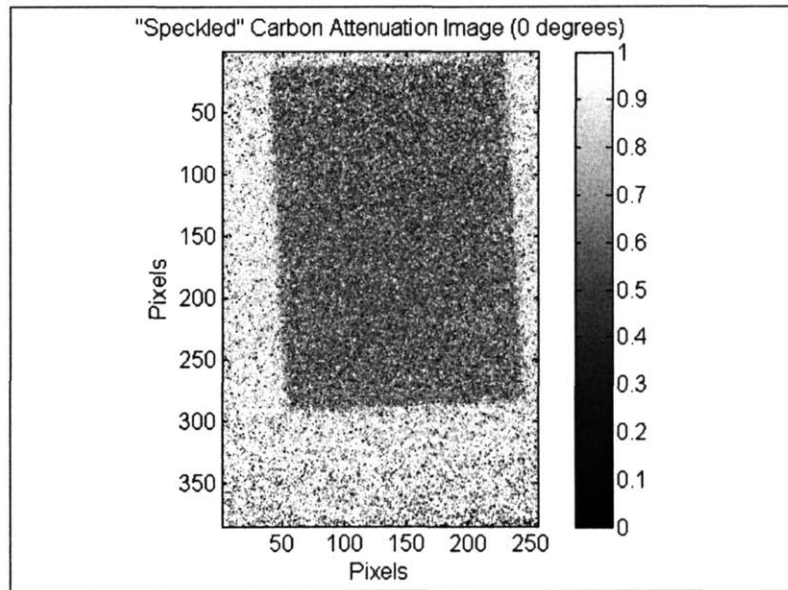
Figure 6.4: "Speckled" carbon attenuation image (0°)

The same area of the carbon block used in the previous "despeckled" images was used for this second analysis. However, instead of an average of the pixels, a histogram was made of the values of the carbon attenuation. Ideally, the histogram would be close to Gaussian in shape with a small error. Histograms of the attenuation values are shown for 0°, 20°, 48°, and 80° in Figure 6.5 through Figure 6.8.
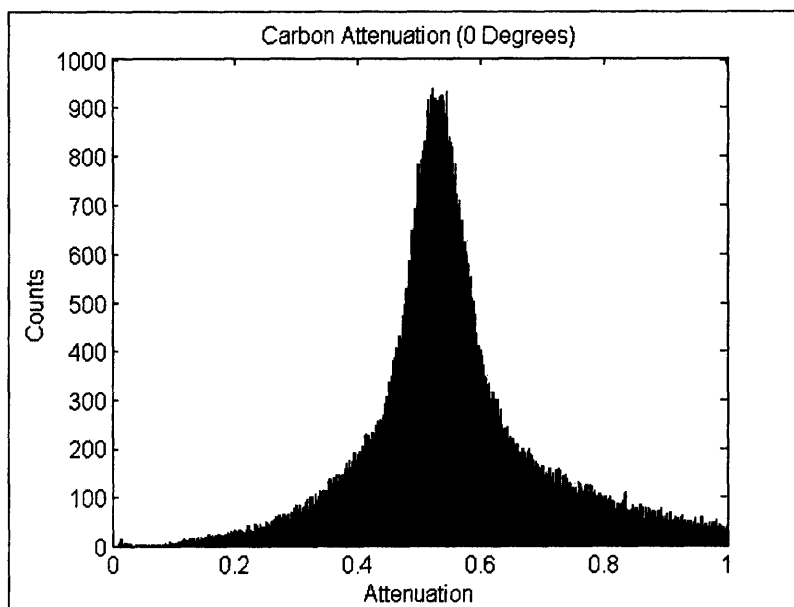
Figure 6.5: Histogram of carbon attenuation values at 0°
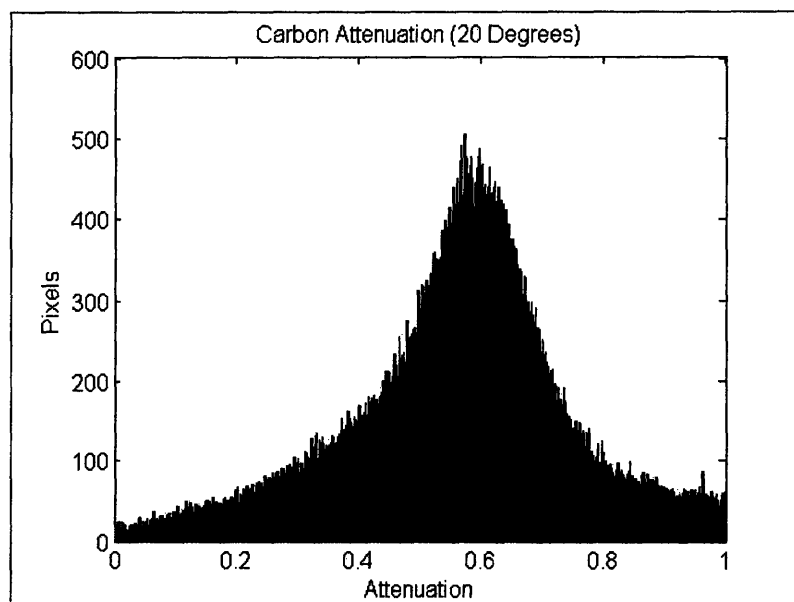
Figure 6.6: Histogram of carbon attenuation values at 20°

154
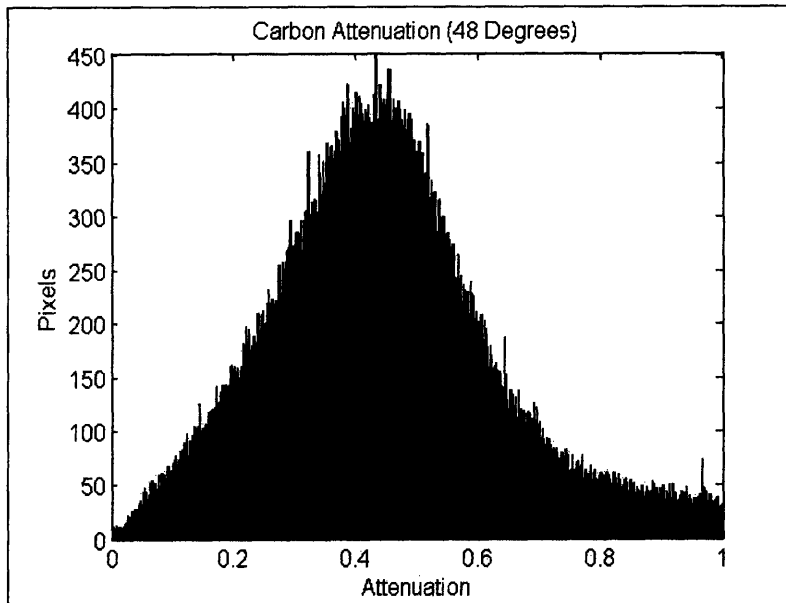
Figure 6.7: Histogram of carbon attenuation values at 48°
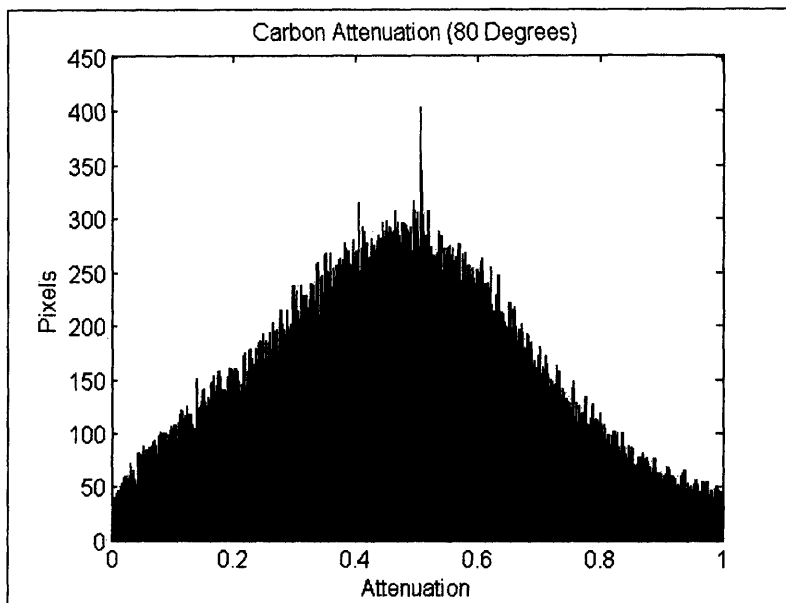
Figure 6.8: Histogram of carbon attenuation values at 80°

The shape of the histograms is similar to a Gaussian curve. As expected, the range of values (and the standard deviation) for the image taken at 80° is greater, as the neutron flux is lower and the attenuation larger at higher angles. The standard deviation

in the measurement was determined using the FWHM of the peak ($\sigma/2$). The attenuation coefficient derived from the peak attenuation value for each angle, along with the standard deviation in the measurement, is shown in Table 6.2 along with the expected values from analytic derivation.

Table 6.2: Peak carbon attenuation using histogram values

Angle/ Energy (degrees/ MeV)	Measured Value (cm^2/g)	Expected Value (cm^2/g)
0/ 4.89	0.054 ± 0.009	0.066
20/ 4.74	0.044 ± 0.02	0.074
48/ 4.12	0.073 ± 0.03	0.098
80/ 3.15	0.063 ± 0.05	0.093

These results are somewhat better than those obtained using despeckling procedures. Some variation in the attenuation coefficient is noticed between the angles, although the effect is fairly small and does not approach the level necessary for elemental discrimination, and the error in these measurements is also quite large.

Using a most likely value without despeckling removes the error inherent to the artificial averaging in low-signal situations. This method seems to indicate that the theoretical premise of NRR can be demonstrated in practice, as Table 6.2 shows some differences in the attenuation at different angles that follows the expected trend. However, this method does not solve the problems inherent in low-signal situations: the attenuation coefficients are not significantly different, especially within the large margins of error. This indicates that the problem in accurately determining the attenuation coefficients is in large part due to the dearth of light produced by the neutrons. There are simply too few neutrons that pass through the carbon and are subsequently detected and recorded by the CCD camera.

6.1.5   Analysis of Results Obtained at MIT LABA

Although the carbon experiment at MIT LABA was originally designed to be the first in a series of experiments designed to determine the attenuation coefficients for all

156

the calibration objects at all the necessary neutron energies and subsequent determination of the elemental content of various unknown objects, the result of the simple carbon experiment described above showed that this course of action would be futile. The variation in the attenuation coefficients at a number of neutron energies is the fundamental basis of NRR; as we were unable to show any variation in the carbon attenuation at different neutron energies, the basic requirement for NRR was not fulfilled.

The results shown above for the calculated attenuation coefficients do not match those that were expected from simulations and theoretical analysis. More importantly, the two attenuation coefficients measured should be significantly different from each other. Unfortunately, they are quite similar, and are also very similar to both the pattern and numerical value of the attenuation coefficients measured from the carbon attenuation experiments discussed in Chapter 3.

This result suggests two factors besides contaminating gamma rays that may contribute to the disappointing results from both the data taken at Ohio and at MIT. First, in addition to gamma rays, off-energy neutrons could also reduce the contrast between attenuation at different neutron energies. In other words, if a large component of the neutron beam was due to off-energy neutrons, the attenuation would not correspond to that expected from neutrons of the desired energy. While the borated polyethylene collimation was meant to ensure that only monoenergetic neutrons were emitted from the target to reach the neutron detector, it is possible that the shielding around the target was not adequate to fully stop all the fast neutrons. Alternatively, it is possible that neutrons that did not interact with the scintillator (a large number – up to 99% of the neutron beam) did interact with the walls and floor of the vault or the extra shielding around the camera, rebounding back to the ZnS(Ag) screen. These counts would reduce the apparent attenuation of the neutron beam by the carbon.

However, attempts to determine the energy of the neutrons reaching the scintillator do not seem to bear out this theory. While the MIT facility does not incorporate a time-of-flight tunnel, the usual method of determining neutron energy, a liquid scintillation detector was available. The advantage to using liquid scintillator is the ability to separate gamma rays from neutrons as well as characterize neutron detections by energy. A neutron detector from Scionix utilizing Eljen liquid scintillator EJ-309

(Table 2.1) was placed beside the camera box at the same height as the ZnS(Ag) screen [60]. In liquid scintillators, the pulse fall time is different for neutron and gamma events and thus we can separate neutrons from gammas. These values neatly separate the neutrons from the gammas, as neutrons have longer rise time than gamma rays [61]. A high speed digitizer was used to analyze the pulses (see Section 2.4.2), enabling the construction of a chart depicting pulse height vs. rise time. Figure 6.9 below shows a 300 second count of the number of neutrons and gamma rays detected from the D-D target (3.3 μA, 2.5 MeV deuteron beam) with the liquid scintillator, plotted by pulse height vs. rise time. The gamma ray events are clearly distinct from those of neutrons.
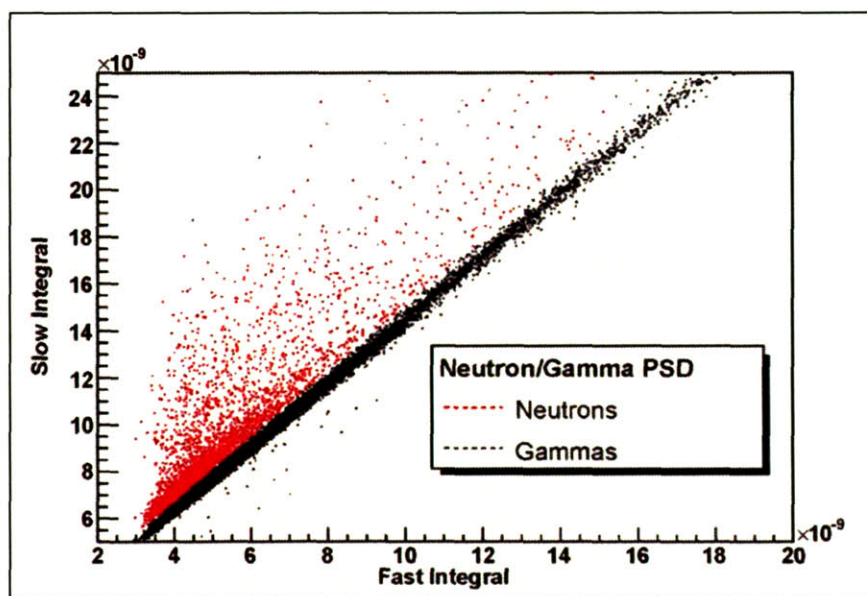
Figure 6.9: Neutron/gamma discrimination for D-D neutron source

Further analysis of the pulses due to neutron detection shows that the energy of the neutrons is fairly well collimated. Figure 6.10 and Figure 6.11 show the (uncalibrated) neutron and gamma ray energy spectrum. The large peak in neutrons indicates that the majority of the neutrons detected with the liquid scintillator are monoenergetic, albeit with some broadening in energy. A "tail" of higher-energy neutrons is evident, however, which shows there some off-energy neutrons present that reached the detector.

158
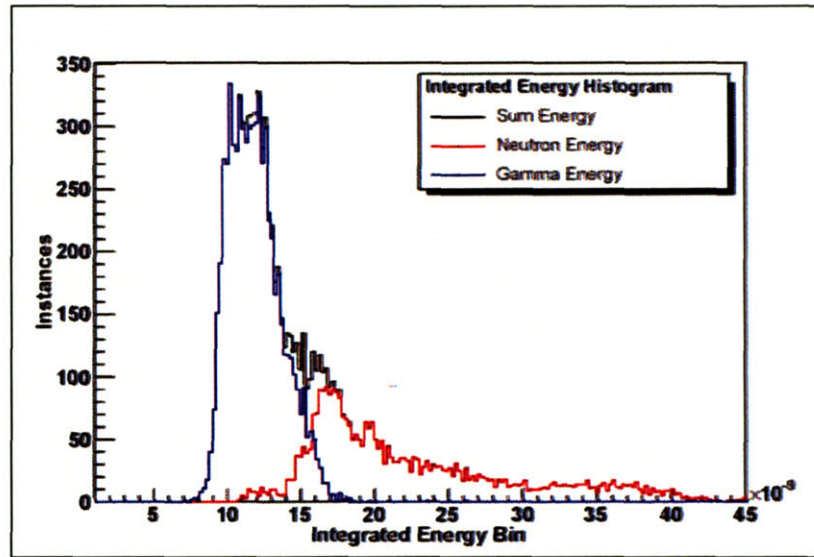
Figure 6.10: Neutron spectrum from D-D reaction at 0°
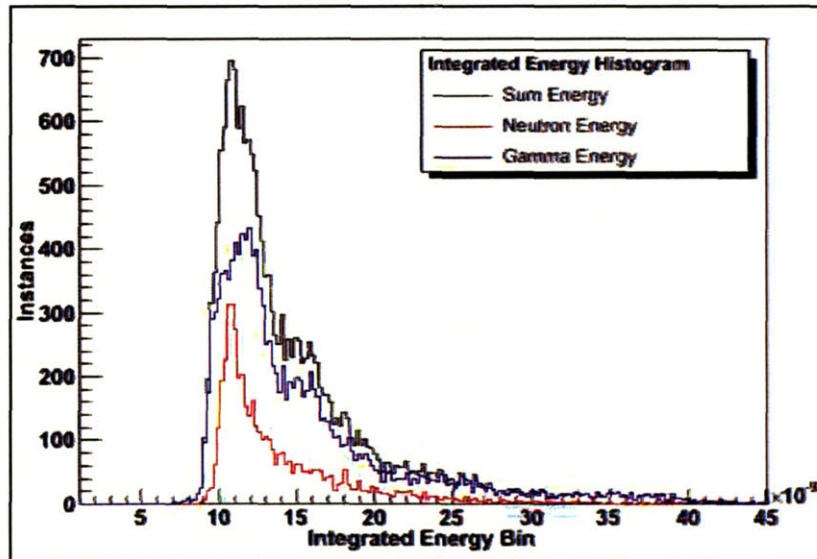
Figure 6.11: Neutron energy spectrum from D-D reaction at 48°

The second factor that likely affects the analysis of the attenuation is the image processing itself. As discussed previously, "dead" or "hot" pixels can result from cosmic rays, defects on the CCD chip, stray particles that interact with the silicon, and a variety of other factors. For the Grade 2 sensor of the Apogee camera, approximately 1-2% of the 6.3 million pixels are considered bad; that is, their values are more than three times

the standard deviation of the median of the surrounding pixels. When the camera is binned, these individual bad pixels also ruin the new "pixel" that they become a part of. When the camera is binned in an 8 x 8 format, resulting in a total of 98,000 pixels, up to 15% of those pixels are corrupted. These pixels are generally bad consistently, meaning that in every image taken, the same pixels are unusable. When the modified median filter is taken into account, the extremely low signal level results in an even larger number of pixels classified as defective due to the large variation in pixel values in a low-signal situation. The total number of modified pixels in many cases exceeded 30%, altogether too large a percentage to result in a realistic number for the attenuation. The value of the modified pixels drastically changed the overall value of the attenuation coefficients. In reality, what was measured was a false "average", rather than the true value of the attenuation.

The consequence of the combination of these two factors was the realization that the MIT LABA facility was not ideally suited to NRR, primarily because of the lack of sufficient collimation and shielding for off-energy neutrons. The decision was made to move the neutron detection system to the MIT Bates Accelerator lab to take advantage of the RFQ accelerator developed specifically for NRR. The Bates facility was designed for the sole purpose of NRR.

6.2   Experiments Conducted at MIT Bates Accelerator Lab

The MIT Bates Accelerator Laboratory is a large facility that previously has housed linear accelerators as part of the MIT Laboratory for Nuclear Science [62]. The system described in the following section is ideal for NRR. The same experiment with carbon was conducted using the RFQ accelerator with the realization that a failure using the RFQ system would indicate that NRR using imaging techniques such as have been described in this thesis is extremely difficult at best and not possible at worst.

160

6.2.1 RFQ Accelerator

The RFQ accelerator built for neutron radiography was manufactured by AccSys Technology, Inc., in Pleasanton, CA. This accelerator has several advantages over the LABA tandem linear accelerator. First, the RFQ is easier to operate than the LABA accelerator. The control software provides for loading sets of pre-determined parameters to return the accelerator to a particular operating state. The RF power supply and ion source can be started and left in stable operation without producing a beam. Beam production can then be rapidly started and stopped by turning the ion source extraction voltage on and off. A stable beam is established very rapidly under these conditions. Start-up is also much faster and more efficient, as a "night-shutdown" mode is incorporated to reduce time needed for start-up and shutdown. Second, as this accelerator installation was designed specifically for NRR, the shielding and layout of the facility was much more conducive to NRR and neutron detection than the MIT facility. Unlike the LABA accelerator, however, the energy is not tunable: the RFQ accelerator was designed to produce a beam of 3.0 MeV deuterons.

The RFQ built for NRR consists of a duoplasmatron ion source, a low-energy beam transport system which injects the ions into the RFQ resonating chamber, and a high-energy beam transport (HEBT) system which focuses the beam as it exits the accelerating chamber. The ion source is designed to provide a 10 – 15 mA d+ beam current. The efficiency of the ion source is greater than 80%.. A high-purity deuterium gas flow into the ion source provides the needed deuterium atoms; a plasma expansion cup ionizes the gas and injects a beam of 25 keV ionized deuterons into the low-energy beam transport system.

The low-energy beam transport system uses an Einzel lens to focus the d+ beam into the accelerating chamber. The accelerating chamber accelerates, bunches, and focuses the deuteron beam using an RF field applied to precisely machined metal vanes that run the length of the accelerating column. The machining of these vanes determines the final energy of the deuteron beam. An end-on view of the vane structure is shown in Figure 6.12. The electromagnetic field generated between opposite electrodes focuses the beam as it passes through the middle of the four electrodes; the undulations on the

161

vane produce the field that accelerates and bunches the beam into a series of high-energy pulses.
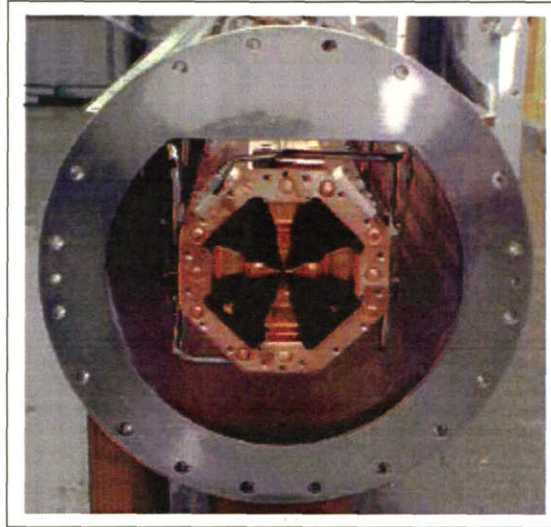
Figure 6.12: End-on view of RFQ accelerator electrodes [63]

As the deuteron beam exits the RF accelerating column, it enters the high-energy beam transport system. The HEBT is a series of three air-cooled electromagnets that further focus the beam onto the gas target. The HEBT system is responsible for focusing the beam into a beam spot approximately one centimeter in diameter, as shown in Figure 6.13. The HEBT system is terminated with a 2 ¾ in Conflat™ flange for attachment to the gas target. A summary of the operating parameters of the RFQ is shown in Table 6.3.

Table 6.3: RFQ operating specifications

Parameter	Value
Operating Frequency	425 MHz
Ion Injector Output Energy	25 keV
RF Output Energy	3.0 ± 0.1 MeV
Max. Output Current	10 mA
Beam Pulse Width	15 – 150 µsec
Beam Pulse Repetition Rate	80 – 800 Hz
Max. RF Duty Factor	1.2%

Other than the relative operation ease and the deuteron output energy of 3.0 MeV, the other difference between the RFQ accelerator and the LABA accelerator is that the deuteron beam from the RFQ is pulsed. This results in higher peak temperatures in the gas target windows, as the peak current in the pulse can be as much as 4 mA, even though the average current may only be on the order of 50 μA. In practice, both tungsten and molybdenum windows have been found to have adequate lifetimes at average currents in the 25-30 μA range. Further experimentation and development will be required to fully characterize the window lifetimes and to determine if higher currents can be used.
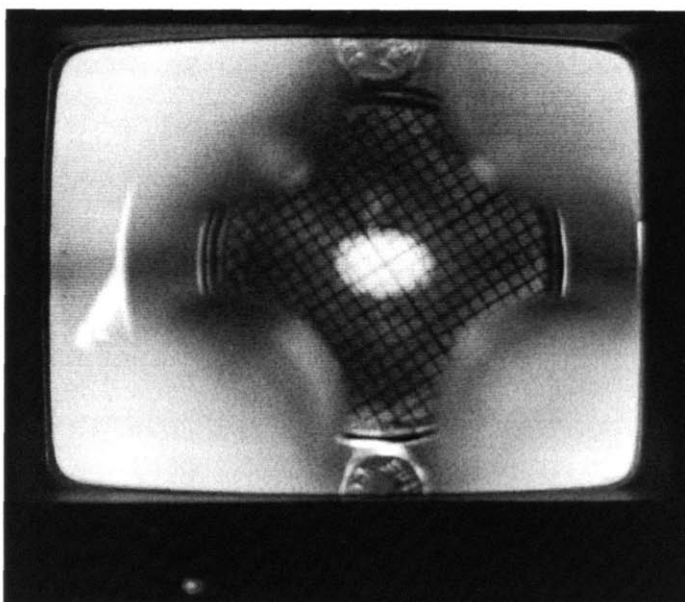
Figure 6.13: Deuteron beam spot at the output of the RFQ. The grid spacing is 1 mm; the quadrupole HEBT system is shown in the foreground.

6.2.1.1 Shielding

The RFQ accelerator has a custom-designed shielding system for the gas target and the detector to minimize the gamma flux and to reduce the number of neutrons that exit the gas target in an unwanted direction. In a laboratory setting, only one neutron energy is needed at a time to make an image. This results in all the neutrons produced at any other angle going unused at any given time. In a commercial setting, it is likely that

163

multiple objects could be imaged at the same time utilizing the entire neutron spectrum, but in the laboratory setting, these neutrons must be stopped before they have a chance to interact with various materials or cause undesired scattering in the detector. The gas target shielding is composed of one inch thick borated polyethylene sheets (5% boron by weight). The shielding is organized into three sections: a horizontal, 20 cm thick stack on the bottom of the target, a 30.5 cm thick vertical slice in the middle, and another horizontal stack, 25 cm thick on the top, as shown in Figure 6.14 below.

Figure 6.14: Borated polyethylene gas target shielding

The vertical middle layer is composed of a series of removable slices, corresponding to the desired angles from 0° to 120°. These slices can be removed individually, exposing only a thin slit 4° wide and 30° tall. Figure 6.15 shows a view looking down an opened slit towards the gas target. The slit can be repositioned without adjusting the top and bottom shielding, enabling fast transitions between desired neutron energy. In this way, fast neutrons from the gas target are only allowed to exit through the slit; any other neutrons are stopped within the borated polyethylene, reducing neutron contamination, activation of accelerator components, and the overall radiation field. As shown in Figure 6.14, a 2 cm thick piece of lead was placed directly over the slit to stop most low-energy photons and further minimize the gamma flux.
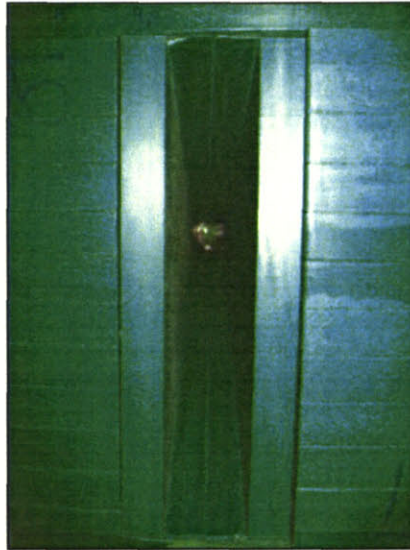
Figure 6.15: Close-up view of gas target shielding with slit removed

A second set of shielding materials is used to protect the camera from stray radiation and further collimate the neutron beam. A collimation system of thick concrete walls was installed at a distance of 1.83 m from the center of the gas target (the edge of the concrete can be seen as the white block on the right side of Figure 6.16). Two concrete walls, each 61 cm thick by 122 cm wide by 300 cm high were placed on either side of a 5 cm vertical gap. This gap corresponds to the position of the exit slit for the neutrons from the gas target. The gap delineates the edges of the neutron beam and allows only a 5 cm wide neutron beam of the desired energy to reach the detector, which is placed behind the concrete wall (see Figure 6.17). The concrete walls also shield the detector from stray gamma rays and any stray neutrons that are able to escape the gas target shielding. The only disadvantage of this collimation system is that images are limited to 5 cm wide (the width of the gap), but this can be overcome by taking a series of images of an object while stepping the object across the slit. The images can then be post-processed and combined into a full image. The result of the borated polyethylene shielding and the concrete collimation is a vast improvement in radiation levels and neutron beam contamination.

6.2.1.2 *Transport*

Unlike the MIT LABA facility which was fairly small, the facility housing the RFQ accelerator was large enough to allow for rotation of the entire accelerator rather than the object-detector system in order to utilize the variation in neutron energy from the gas target. The RFQ accelerator and gas target are mounted on a rotating platform that can be moved to the desired angle (see Figure 6.16 below). This greatly reduces the space needed for the entire NRR system and the reproducibility of the results, as the object and detector system can stay fixed which the accelerator rotates on a much tighter radius[xiv]. The rotation of the system is highly reproducible, resulting in positional variation of only hundredths of a degree.
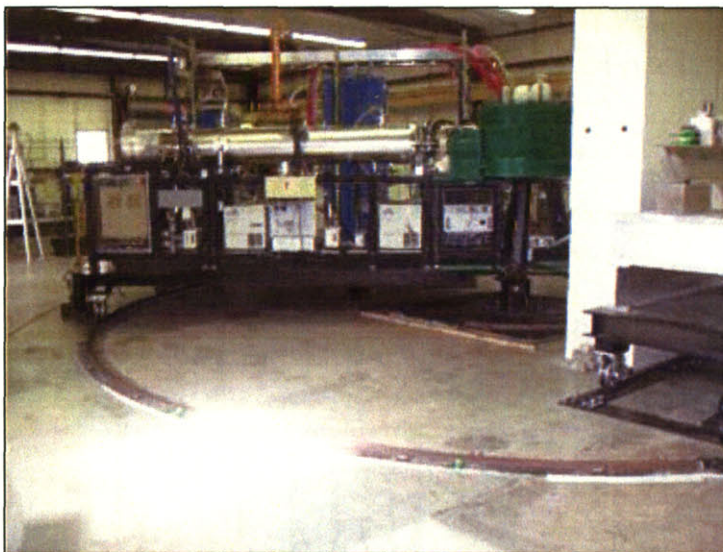
Figure 6.16: RFQ accelerator assembly and rotating platform

6.2.2 Experimental Setup

The experimental setup for the RFQ accelerator was similar to that of the tandem accelerator at MIT. The gas target described in Chapter 4 was used, with a 7 μm molybdenum foil front window and a thick tungsten beamstop, both supported by the

---

[xiv] In a commercial setting, the accelerator would stay fixed while the object and detector were moved around it.

small-holed strongbacks, while the target itself was filled with 4 atm of deuterium. Argon was again used to cool the target with a continuous 1.5 atm, 4 – 5 scfm gas flow. As discussed in the previous section, the RFQ accelerator produced 3 MeV deuterons, increasing the stress on the gas target. For this reason, the current was limited to 25 μA to avoid destroying the thin foil entrance window or the tungsten beam stop.

Neutron and gamma ray shielding was more extensive for the RFQ accelerator. Molded borated polyethylene surrounded the gas target on all sides, creating half a meter of neutron shielding. Only a very thin slit corresponding to the exact energy of the neutrons desired was left unshielded. Additional shielding was incorporated into the RFQ system to reduce the gamma ray flux and reduce the number of scattered neutrons that were able to reach the detector. A concrete collimator was constructed that restricted the neutron beam to only two inches wide. The concrete itself was 60 cm thick, ensuring that all neutrons would be stopped in the concrete except for those in the two-inch wide slit. Thus, the borated polyethylene reduced the number of neutrons and gamma rays leaving the gas target, while the additional concrete shielding provided further collimation. The combination of the two shielding systems guaranteed that the only neutrons reaching the detector were those of the desired energy.

The same CCD camera was used for the experiments using the RFQ accelerator as that described in Chapter 5. The CCD camera was again cooled to -25 °C and enclosed in the same light-tight box (see Figure 2.4). The camera was placed behind the two feet of concrete shielding, which had the added benefit of thoroughly shielding the camera from stray particles. The scintillator was located 2.45 meters from the neutron source. A 2 x 2 pixel bin was again used to reduce the statistical error caused by the low signal and subsequent despeckling and averaging. The despeckled images were subsequently binned by hand to 8 x 8 to increase the signal and provide better statistics.

The carbon block used for these experiments was a two inch thick piece of carbon with a measured density of 1.77 g/cm^3 and wide enough to cover the entire slit in the concrete. The geometry of this setup is as close to ideal as possible: the collimating behavior of the concrete shielding reduces the number of neutrons that scatter off the carbon but are still detected by the scintillator. A top-down view of the accelerator, shielding, and position of the carbon target and detector are shown in Figure 6.17. The

carbon block was 1.83 meters from the neutron source and the detector 0.62 meters from the carbon block, leading to a magnification of 0.88.
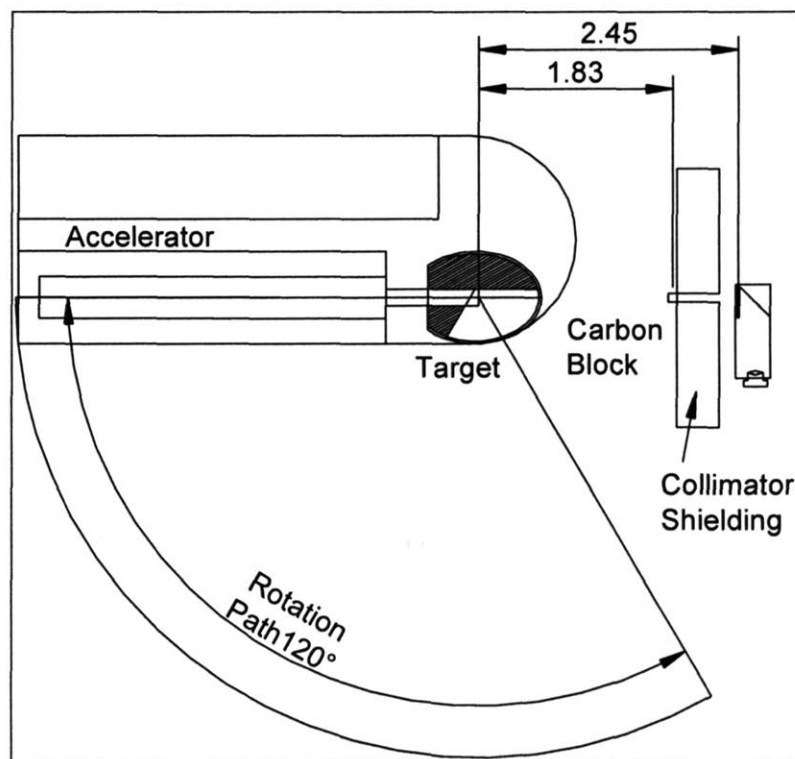
Figure 6.17: Shielding and detector arrangement for RFQ accelerator

6.2.3 Results from Carbon Attenuation Using RFQ Accelerator

The MIT Bates facility offered a significant advantage both in a reduction of neutron scattering and in gamma flux. The ratio of neutrons to gamma rays from the RFQ was estimated at 6:1, a huge improvement over the ratio observed in the LABA vault. This permitted the evaluation of the use of the plastic scintillator as well as the ZnS(Ag) screen. The greatest difference in carbon attenuation occurs at 15° and 75° (5.38 and 3.5 MeV). Two radiographs were taken at these two angles; one of an open beam and one of a carbon beam. A "dark" image was taken at each angle as well, and the images were despeckled. The dark image was subtracted from both the carbon and the open images, and each pixel in the carbon image was divided by the corresponding pixel

in the open beam image to evaluate the performance of each neutron detector at each angle.

6.2.3.1 ZnS(Ag) Screen

The ZnS(Ag) screen, while less efficient for neutron detection, has other properties that are useful for NRR; namely, the resolution is better and the light distribution within the scintillator smaller than that of the plastic scintillator. As previously mentioned, the trade-offs between efficiency, resolution, and gamma ray contamination must be balanced. Although the gamma flux from the RFQ was much lower than the gamma flux produced by the LABA accelerator, the positive attributes of the ZnS(Ag) screen, namely the resolution and light dispersion, led us to use this material for neutron detection for the RFQ trials as well.

An "open beam" image and an image of the carbon block were both taken using the ZnS(Ag) scintillator. The imaging time amounted to 60 minutes, but the final image was composed of six ten-minute images added together. Figure 6.18 shows the carbon attenuation at 15° and at 75° (I/I_0). Due to the reduction in neutron flux at high angles, the carbon attenuation at 75° is much noisier than the image at 15°.
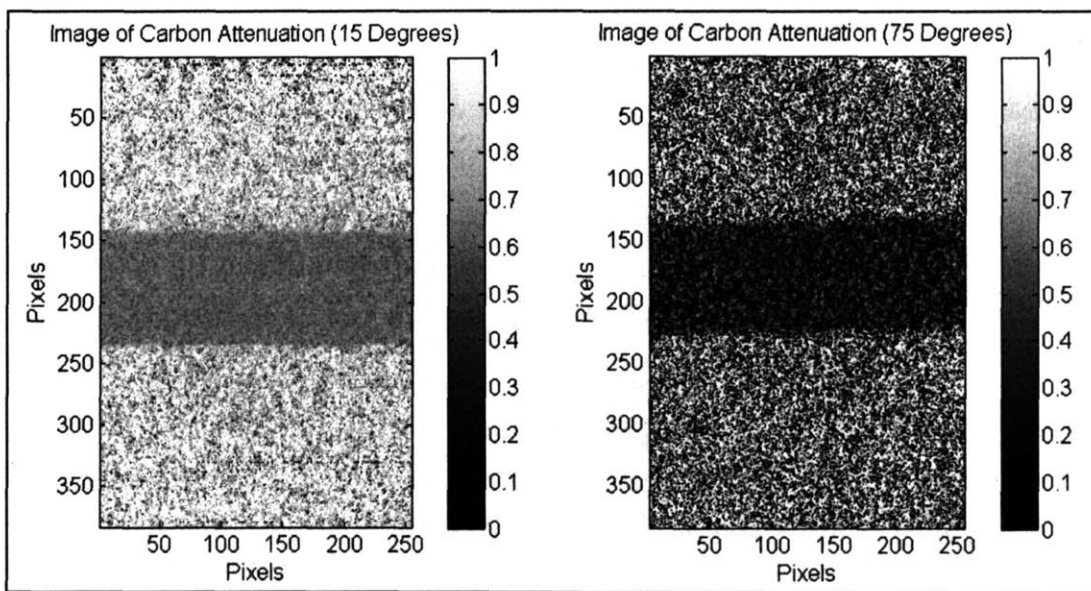
Figure 6.18: Carbon attenuation at 15° and 75° using ZnS(Ag) screen

The attenuation coefficient was again calculated using Eq. 2.1 and Eq. 2.2 by using an average value of a representative area of the image and compared to the theoretically expected value. The results are shown in Table 6.4.

Table 6.4: Carbon attenuation for 15° and 75°

Angle	Measured Value (cm^2/g)	Expected Value (cm^2/g)
15°	0.0536 ± 0.028	0.058
75°	0.1533 ± 0.245	0.119

The attenuation coefficients were calculated to be $0.0535 \pm 6.5 \times 10^{-4}$ cm^2/g and 0.1729 ± 0.11 cm^2/g at 15° and 75°, respectively, while the expected values are 0.058 cm^2/g and 0.119 cm^2/g.

Again, these results are unsatisfactory. At 15°, where the neutron flux, and thus the signal on the CCD chip, is largest, the experimental result is quite similar to the expected value. At 75°, however, where the neutron flux and resulting signal much lower, the error is significant. The lack of adequate signal, similar to the results obtained at MIT LABA, ruins any chance of determining accurate attenuation coefficients.

A comparison of the attenuation using the histogram method described in Section 6.1.4 was also used on the data obtained from the RFQ accelerator. Again, a histogram of the carbon attenuation values was made and the peak value and standard deviation from the mean (half the FWHM value) was determined. The results are shown in Figure 6.19 and Table 6.5 below.
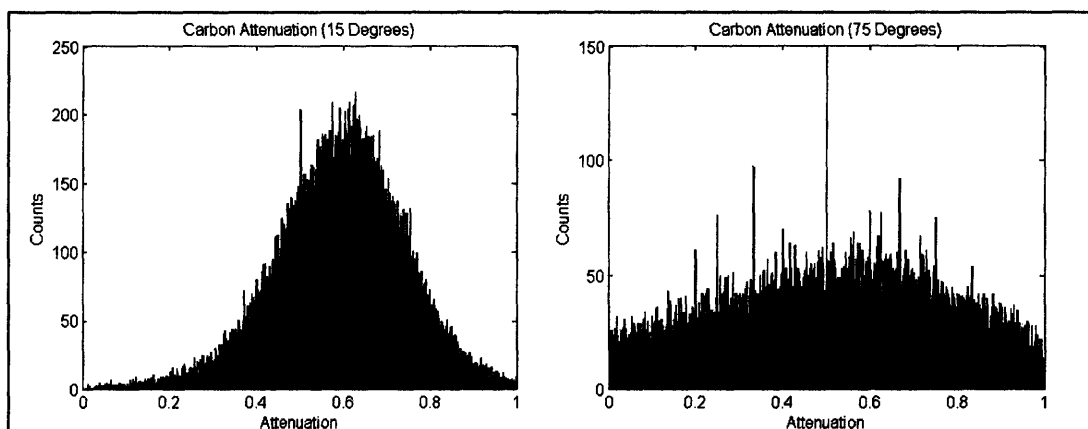
Figure 6.19: Histogram values of carbon attenuation at 15° (left) and 75° (right)

Table 6.5: Carbon attenuation values from histogram method

Angle	Carbon Attenuation (Measured)	Carbon Attenuation (Expected)
15°	0.6046 ± 0.142	0.600
75°	0.6416 ± 0.29	0.348

The values generated for the carbon attenuation from the histograms show no improvement over the image processing method. However, the histograms clearly indicate the lack of signal and the problems inherent to a low-light imaging system. The histogram on the right in Figure 6.19, 15°, has demonstrably better statistics and a clearly defined peak due to the higher neutron flux and increase in signal. The value of the attenuation at 15° also corresponds well to the expected attenuation value, albeit with large error, further indicating that an increase in signal may improve the values at higher angles with lower neutron.

6.2.3.2 Solid Plastic Scintillator

The low efficiency of the ZnS(Ag) screen coupled with the relatively high neutron to gamma ratio led to the use of solid plastic scintillator as a secondary means of detection. The material used was one inch thick EJ-200 plastic scintillator from Eljen Technology [64]. While not transparent to gamma rays, the fast neutron detection

171

efficiency of plastic scintillator is much higher than the detection efficiency of ZnS(Ag). While the detection of gamma rays is detrimental to accurate calculations of the attenuation coefficients, the increase in signal more than compensates for the negative effects of gamma rays.

The same experimental design as described in the preceding section was used, with the ZnS(Ag) screen replaced by the one-inch thick EJ-200 plastic scintillator. The increase in thickness of the scintillator with respect to the ZnS(Ag) has a small effect on the focus of the CCD camera, as the focal point of the camera is the center of the scintillator. Other than that small difference, the arrangement was the same: the camera was placed 2.5 meters from the neutron source behind the concrete shielding, while the carbon block was positioned covering the entire front of the slit. Given the higher efficiency of the plastic scintillator, 30 minute radiographs were taken, rather than 60 minutes, composed of six five-minute images added together. The imaging time was reduced from ten minutes to five minutes to reduce the temperature reached in the gas target and prolong its life.

The procedure for obtaining the carbon attenuation coefficients is the same as previously described. The images were despeckled according to the modified median filter. A "dark" image was subtracted from the carbon image and the open image, and each pixel in the carbon image was divided by the same pixel in the open beam image. The attenuation in a representative box was averaged and the carbon attenuation coefficients at 15° and 75° were calculated using Eq. 2.1 and Eq. 2.2. The attenuation is shown in Figure 6.20. The values of the carbon attenuation coefficients were calculated to be 0.064 ± 0.0012 cm^2/g and 0.100 ± 0.23 cm^2/g at 15° and 75°, respectively. Table 6.6 compares the expected value of the carbon attenuation with those measured from the experimental results for both the plastic and ZnS(Ag) screen.
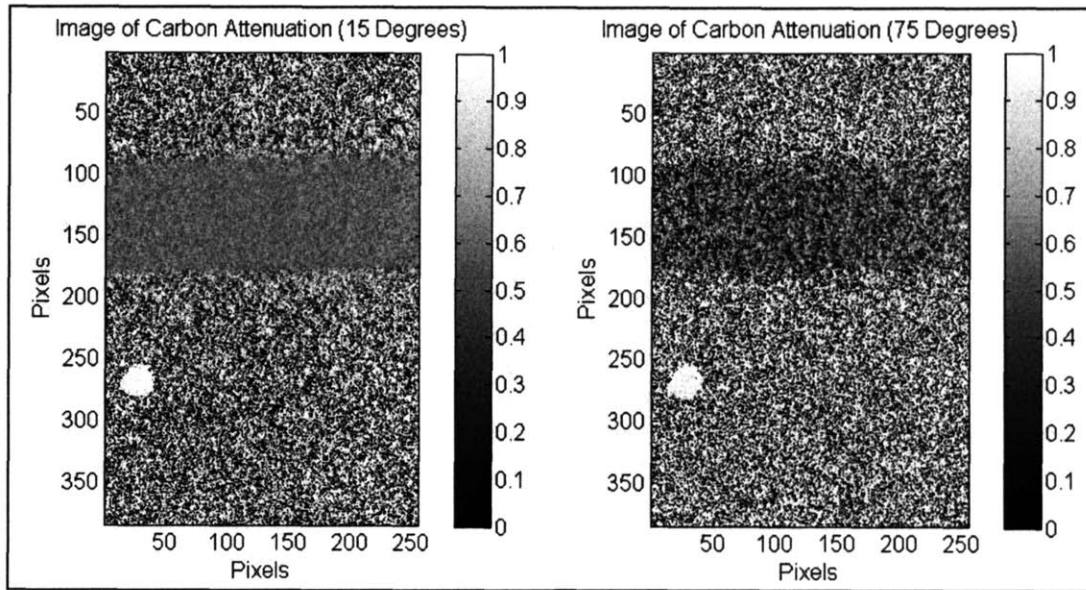
Figure 6.20: Carbon attenuation at 15° and 75° using solid plastic scintillator. The white circle on the left is an artifact from a light leak but has no effect on the value of the attenuation coefficient.

6.2.4   Analysis of Carbon Attenuation Using RFQ Accelerator

Results obtained from the use of the RFQ accelerator did not prove to be appreciably better than the results achieved using the MIT LABA accelerator. A summary of the values of the carbon attenuation (I/I_0) obtained using the ZnS(Ag) and plastic scintillator compared to those expected is shown in Table 6.6. The carbon attenuation (I/I_0) rather than the attenuation coefficients (μ) is shown to more accurately characterize the error in the measurements.

Table 6.6: Expected versus experimental carbon attenuation

Angle	Carbon Attenuation (Plastic Scintillator)	Carbon Attenuation (ZnS(Ag))	Carbon Attenuation (Theoretical Value)
15 degrees	0.57 ± 0.0060	0.62 ± 0.0036	0.600
75 degrees	0.41 ± 2.86	0.26 ± 0.37	0.348

173

The results from the RFQ accelerator, whether the neutron detector was ZnS(Ag) or the plastic scintillator, were not consistent with the expected attenuation coefficients, and the error is obviously too high for the data to be credible. As any problem that could be attributed to off-energy neutrons is removed by the extensive shielding and collimation of the neutron beam, the discrepancy between expected and measured attenuation cannot be attributed to detection of slow neutrons. Likewise, the gamma flux from the RFQ accelerator is much smaller than that in either the experiments performed at Ohio and described in Chapter 3 and those at MIT LABA described in the previous section. The use of gamma-blind ZnS(Ag) further reduces any harmful effects from gamma rays, but even those experiments using ZnS(Ag) did not produce an accurate measurement of the expected attenuation.

Binning in a 2 x 2 format on the CCD chip (compared to the 8 x 8 bins used for the LABA work) has its drawbacks as well as its benefits: while it increases the number of pixels that can be used (are not considered "dead"), it reduces the signal per "pixel" by a factor of 16. The very low signal level, especially noticeable at high angles (low neutron energies) is the most likely cause of the problems in carbon attenuation measurements. The lack of signal is the limiting factor in all the experiments undertaken.

6.3 Discussion of Experimental Results

The experimental results, both those at MIT LABA using the tandem accelerator and at MIT Bates using the RFQ accelerator are discouraging and precluded continuation of experimental work. We were unable to improve upon the results at Ohio; in fact, the results from experiments using the new gas target with fewer gamma rays actually significantly reduced the signal reaching the CCD camera. While this validates the reasoning put forth in Chapter 3, that gamma rays were the cause of the low and constant attenuation coefficients, the severe reduction in signal was devastating for NRR. Obviously, more signals or a more efficient type of neutron detection mechanism (or both) is required before any type of elemental discrimination can be conducted.

The results presented above do suggest some positive indications for NRR, however. First, the carbon attenuation at low angles with high neutron flux (i.e., 0° and 10° at MIT LABA and 15° using the RFQ) are very close to the theoretical values, demonstrating that when the neutron flux is high, resulting in more signal, the results are quite reasonable. Additionally, the two image processing techniques used in Section 6.1 give very similar values for the high-flux carbon attenuation. This similarity again illustrates that the image processing and resulting value of attenuation is highly dependent on signal.

Another important point to be made is the difference in imaging capability between the ZnS(Ag) screen and the plastic scintillator. A comparison of the images taken at 15° in Figure 6.18, carbon attenuation using the ZnS(Ag) screen, and in Figure 6.20, attenuation using the plastic scintillator, illustrates this point. Evident in Figure 6.20 is significantly more light spreading and a reduction in the sharp distinction between the slit and concrete, where no neutrons are detected. Figure 6.18, on the other hand, shows a clear delineation between the open slit and the concrete and considerably less light diffusion. Line-out plots drawn through the center of the images graphically represent this point in Figure 6.21. ZnS(Ag), with its higher resolution and lower light dispersal combined with its highly inefficient gamma detection, is the superior of the two neutron detection materials investigated here.
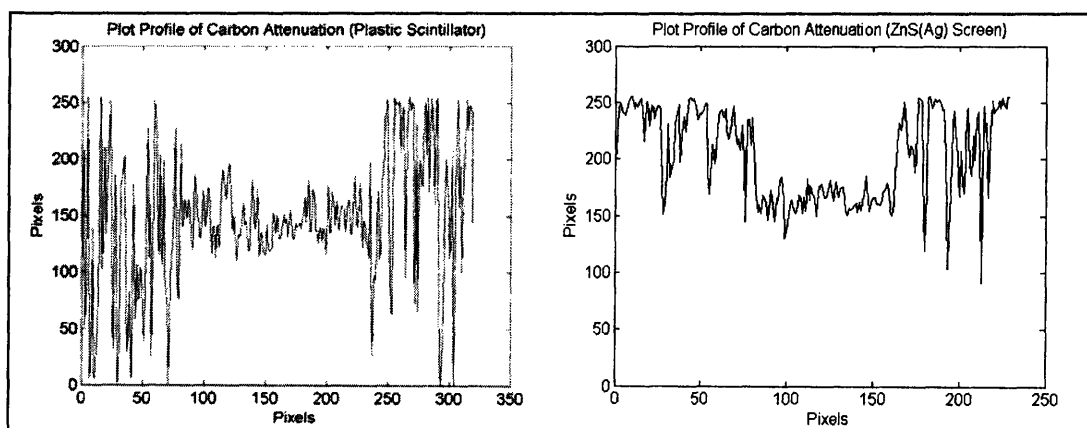

Figure 6.21: Line-out drawings of carbon attenuation for plastic scintillator (left) and ZnS(Ag) (right)

All told, these experiments indicate that NRR is still a method of explosives detection to be considered seriously. To create a workable system, however, a much higher neutron flux is required. This is not a simple task, but it is feasible through the use of windowless targets and high-current accelerators. More importantly, a more efficient neutron detection system is vital. The low detection efficiency of the ZnS(Ag) and plastic scintillator combined with the light loss inherent to lens-coupled CCD systems is overwhelming for a mechanism that requires relatively high signal-to-noise in order to be successful. Alternate means of neutron detection and image formation will be discussed in the final chapter of this thesis.

6.4 Chapter Summary

This chapter has described the experiments undertaken to prove the viability of multiple-element NRR. Two sets of experiments were performed: one set at the MIT LABA facility using the tandem accelerator and continuous neutron beam described in Section 4.1, and a set of experiments using the RFQ accelerator described in the beginning of this chapter. Both sets of experiments were designed to show the carbon attenuation as a function of neutron energy. At MIT LABA, a ZnS(Ag) scintillator was used to detect neutrons and produce light that was subsequently recorded by a CCD camera to determine the attenuation of the neutron beam through a 2.75 in (7 cm) thick carbon block at six different angles. Using an RFQ accelerator at a specially designed NRR facility, a ZnS(Ag) and solid plastic scintillator were individually used to measure the attenuation of a 2 in (5 cm) thick black of carbon at two neutron energies corresponding to the largest expected difference in neutron attenuation.

The determination of the carbon attenuation as a function of neutron energy is essential for the principle of multiple-element NRR. Carbon is the only calibration material that is readily available as a pure, solid single element, not a compound; if the attenuation coefficients at various angles cannot be determined for carbon, they cannot be accurately determined for any other element. Carbon also has the widest range of attenuation coefficients over the neutron energy range of interest. Accurate

representation of the attenuation of various elements at determined neutron energies is required for NRR.

Regrettably, the results are less than encouraging. The measured carbon attenuation coefficients are significantly different from the expected values, and perhaps more importantly, have such high inaccuracies that it is impossible to garner much useful information. Use of the plastic scintillator, which has a higher detection efficiency for fast neutrons than ZnS(Ag), did not improve the results. Further, different means of image processing had a noteworthy impact on the final values, suggesting that more signal in the final images would be necessary to overcome obstacles presented by the low signal-to-noise ratio. While these results are not as useful as hoped for at the beginning of this project, they do indicate that NRR as an explosives detection method still holds promise if the neutron detection system can be improved. Suggestions for improvement are discussed in the following chapter.

7   Conclusions and Future Work

This thesis has taken the first step towards experimentally proving the feasibility of an explosives detection system using neutron resonance radiography. Neutron resonance radiography, or NRR, is envisioned as a secondary explosives detection system for checked luggage at airports. Rather than replacing current x-ray systems, an NRR system is seen as a second-tier system to investigate those items flagged as suspicious by x-ray systems. In this way, NRR would reduce the number of hand-searches of luggage, reduce privacy concerns, and increase the safety of the screening personnel.

Neutron resonance radiography combines imaging techniques with the ability to determine elemental composition. Imaging using x-ray systems allows only for a relative density measurement; as many commonly packed items have quite similar density as explosive material, this technique results in a fairly large number of false alarms. By using NRR, the elemental components of the suspect items can be found and compared to the known elemental content of explosives. Most explosives have a much different elemental signature than innocuous materials, even though the predominant elements are still carbon, nitrogen, oxygen, and hydrogen. By identifying the elemental components of an object instead of simply the density, NRR has an increased chance of correctly identifying explosive material.

The method employed by NRR for elemental discrimination relies on the neutron cross-section, a property of the nucleus that determines the likelihood of neutron interaction. The neutron cross-section is unique to each element and the value varies with neutron energy. NRR exploits these variations by measuring the attenuation of a beam of neutrons corresponding to different values of the neutron cross-section. The neutron beam will be attenuated differing amounts based on the value of the neutron cross-section of the elements present in the object of interest. By measuring the total attenuation using neutrons of a number of different energies, a series of equations can be constructed using known values of attenuation for different elements. By solving this series of equations, the amount of each element present in the object can be found. The elements of primary interest are hydrogen, carbon, oxygen, and nitrogen. By determining

the elemental content, an elemental map of the object can be constructed, providing a spatial representation of the object together with its elemental constituents.

The equipment involved in NRR is fairly straightforward, although the individual components are quite complicated. NRR requires a neutron source, a neutron detector, and means of converting the detected neutrons into a digital image. The $D(d,n)^3He$ reaction has been identified as the most promising source of fast neutrons. A deuterium gas target, combined with an accelerator system to provide fast deuterons for neutron production, is the most uncomplicated means of employing the D-D reaction. Fast neutrons are generally detected by solid scintillating material: as neutrons interact with protons in the detector, energy is imparted to the material and light is emitted. For "direct imaging" NRR, this light is subsequently focused by a lens system onto a digital CCD camera and an image is created for analysis.

Theoretical studies have shown that NRR is quite promising as a means of detecting explosives and other contraband. This thesis has built upon the body of theoretical work and simulations to develop a basic prototype NRR system and determine the viability of NRR in a laboratory setting. Preliminary experiments indicated that gamma ray contamination of the final image led to severely detrimental effects on the calculated attenuation coefficients due to unwanted detection of gamma rays. This contamination led to inaccurate calculations of elemental content.

The majority of the work presented in this thesis moved forward from the preliminary experiments to develop a deuterium gas target that could provide a high neutron flux with a relatively low amount of gamma ray contamination. Measurements of the gamma flux from various metals due to deuteron interactions were made to determine the optimal material with which to construct the gas target. Tungsten and molybdenum proved to be the most favorable metals, both for their low gamma production and for their strength and ability to withstand high temperatures. A thin (5-7 μm) foil was used to separate the high vacuum of the accelerator beamline from the gas target cell, supported by a thick tungsten grid designed to alleviate the stress due to high heat and high pressure. By incorporating this "strongback" into the window design, the gas target could contain a higher pressure of deuterium and hold up to high (25 μA)

deuteron currents, increasing the neutron flux from the target. The gas target was designed to produce a neutron flux up to 6.6×10^7 neutrons/sr/μA/s at $0°$.

Two neutron detection systems were investigated in this thesis: a ZnS(Ag) screen and a solid plastic organic scintillator. These two materials both have properties that are advantageous for NRR: ZnS(Ag) is gamma-blind, while plastic scintillator has a higher detection efficiency for fast neutrons. Both these scintillators were used in experiments to determine the attenuation of neutrons due to carbon. The light produced from the scintillators was detected by a CCD camera made by Apogee Instruments.

The CCD camera was an off-the-shelf system with extremely low dark current (0.004 counts/pixel/sec at -25 °C) and the ability to bin the pixels on chip to allow investigation of the optimum pixel size – binned pixels accumulate the counts from a number of contiguous physical pixels without increasing the read noise. The system was cooled using a thermo-electric cooler to -25 °C, which provided sufficiently low dark current values without the complications and expense of a liquid nitrogen-cooled camera. While extremely important as the means of producing digital images, the lens-coupled CCD camera system is the major drawback of the NRR imaging system. The fraction of light that reaches the CCD chip through the lens is only on the order of $1.7 \times 10^{-3} - 1.7 \times 10^{-4}$, a tiny amount when coupled with the low detection efficiency of the neutron detectors. This ultimately proved to be the limiting factor for NRR.

To investigate the ability of the entire system to determine elemental content of objects, we first attempted to show that NRR would be able to produce accurate measurements of carbon attenuation. Using fast neutrons produced by the MIT Laboratory for Accelerator Beam Applications 4 MV tandem accelerator and the gamma-blind ZnS(Ag) screen, images of a carbon block taken with neutrons of energies 4.89, 4.74, 4.12, and 3.15 MeV were obtained. Unlike a deployable system in which the imaging time must be on the order of seconds, the images were taken for 30-60 minutes, depending on the neutron flux to generate sufficient signal. Still, the signal was so low that we were unable to make accurate measurements of the carbon attenuation due to the high error and variation in signal over the CCD chip. Further, given the low intensity of the images, different image processing techniques significantly affected the results.

The poor results from MIT LABA compelled us to move to a new facility to use an accelerator dedicated to the use of NRR. Using the same ZnS(Ag) screen, and a one-inch thick plastic scintillator from Eljen Technology, images of a carbon block were taken with 5.38 and 3.5 MeV neutrons and analyzed for attenuation. Again, imaging times ranged from 30-60 minutes. Once again, the neutron flux was too low and the detection system too inefficient to produce well-resolved, accurate measurements of the carbon attenuation. Given the failure to determine the carbon attenuation, it was futile to move on to determination of the attenuation of other materials, or to attempt to investigate the elemental properties of unknown objects.

While the experiments undertaken in this work proved to be a disappointment, they do shed light on techniques to improve NRR and enable its use. First, a more efficient means of neutron detection must be developed. There are a number of ways to accomplish this. Further reduction in gamma flux will allow the use of thicker, more efficient plastic scintillator as the neutron detector. Experimentation with a liquid scintillator is an even more promising avenue. Liquid scintillators have the ability to distinguish neutrons from gamma rays, as well as characterize the energy of the neutrons detected. By developing a liquid scintillator system that is position-sensitive, an imaging system could be created that could simultaneously increase detection efficiency and eliminate unwanted detections of gamma rays and off-energy or scattered neutrons. Liquid scintillator has its drawbacks, however. The liquid scintillator itself is corrosive and toxic, a drawback in a high-throughput environment that necessitates ease of use and safety for operators. However, if these complications can be overcome, liquid scintillator is good candidate for NRR.

A second means of neutron detection is to move from imaging using a CCD camera to position-sensitive photomultiplier tubes (PMT). Instead of imaging using a lens and tolerating the subsequent loss of signal, PMTs allow individual neutrons to be counted. The signal is thus much higher, and established techniques of pulse-height analysis would allow the discrimination between most gamma rays and neutrons. The number of counts in each PMT can then be mapped to construct an image of neutron counts. If the PMTs are small enough, the "pixels" created by this image would have a

resolution high enough to detect small objects. This method is currently being investigated for the screening of air cargo containers, where the resolution element size is less important than for luggage, with good success.

Finally, if one wishes to continue with a CCD-based, solid-scintillator system, a low-resolution, extremely low-noise camera with a Grade 1 sensor should be obtained. The elimination of as many defects on the CCD chip as possible is a requirement. This substantially increases the cost of the system, but could improve the detection capabilities to the extent that it may be worth it. Further, the neutron flux must be increased. While we attempted to develop a gas target able to withstand high currents and provide sufficient neutron flux, and did improve the neutron production relative to other windowed gas targets, windowless gas targets will probably provide a higher neutron flux than windowed targets if sufficiently intense accelerator beams are used. However, these targets are more difficult to maintain and operate than gas targets and may prove to be difficult to use in an airport environment. Intense neutron sources will be more difficult to shield, and there may be a limit to the utility of increasing neutron flux, particularly where the d-d reaction is used and a large fraction of the neutrons produced must be absorbed near the target.

Neutron resonance radiography still has the potential to be a useful explosives detection system, if obstacles unapparent in theoretical deliberations and simulations can be overcome. Of primary importance is the increase in signal and neutron detection efficiency. This thesis has taken an important experimental step towards developing a system designed to use NRR to detect explosives.

References

[1] Quillen, Chris, "Mass Casualty Bombings Chronology," *Studies in Conflict and Terrorism*, 25:293-302, 2002.

[2] White House Commission on Aviation Security and Terrorism, "Report of the President's Commission on Aviation Security and Terrorism", Washington, DC, May 15, 1990.

[3] White House Commission on Aviation Safety and Security, "Final Report to President Clinton", Washington, DC, February 12, 1997.
Available at http://www.fas.org/irp/threat/212fin~1.html, accessed 12 October, 2006.

[4] Gozani, Tsahi, "The role of neutron based inspection techniques in the post 9/11/01 era," *Nuclear Instruments and Methods in Physics Research B* 213 (2004) 460–463.

[5] Elias, Bartholomew, "Aviation Security: Issues Before Congress Since September 11, 2001," CRS Report for Congress RL31969, February 6, 2004. Available at http://hutchison.senate.gov/RL31969.pdf, accessed June 10, 2005.

[6] Jimmie C. Oxley, "The Chemistry of Explosives," in *Explosives Effects and Applications*, Jonas A. Zukas and William P. Walters, Eds. (New York: Springer-Verlag, 1998).

[7] Oxley, Jimmie C., "Explosives Detection: Potential Problems," *Proceedings of the SPIE*, vol. 2511, pg. 217.

[8] Gozani, Tsahi, "Principles of Nuclear-based Explosive Detection Systems," *Proceedings of the First International Symposium on Explosive Detection Technology*. Atlantic City, NJ, November, 1991, pg. 27.

[9] Krauss, R.A., "Signatures of Explosives by Elemental Composition Analysis". *Proceedings of the Second Explosives Detection Technology Symposium & Aviation Security Conference*, Atlantic City, NJ, 1996.

[10] Daniel McGrory, "Hamas make explosive used by Reid," *The Times (London)*, December 29, 2001, Overseas News.

[11] Mark Henderson, "Liquids make explosive mix," *The Times (London)*, August 11, 2006, Home News, pg. 9.

[12] Wolfe, Jeremy M., Horowitz, Todd S., Kenner, Naomi M., "Rare items often missed in visual searches," *Nature*, vol. 435, 26 May 2005, pg. 439.

[13] Roder, Fredrick L., "The Evolution of Computer Tomography (CT) as an Explosives Detection Modality," *Proceedings of the First International Symposium on Explosive Detection Technology*. Atlantic City, NJ, November, 1991, pg. 297.

[14] Krug, Kristoph D. and Stein, Jay A., "Advanced Dual Energy X-Ray for Explosives Detection," *Proceedings of the First International Symposium on Explosive Detection Technology*. Atlantic City, NJ, November, 1991, pg. 282.

[15] Myers, Lawrence J., "The dog-handler team as a detection system for explosives: A tail to be told," *The Aviation Security Problem and Related Technologies*, Wagih H. Makky, ed., 20 July, 1992, pg 93.

[16] Yinon, Jehuda, "Field detection and monitory of explosives," *Trends in Analytical Chemistry*, v. 21, 4, 2002.

[17] Steinfeld, Jeffery I. and Wormhoudt, Jody, "Explosives Detection: A Challenge for Physical Chemistry," *Annu. Rev. Phys. Chem.*, 1998, 49:203-32.

[18] Lee, W. C., Mahood, D. B., Ryge, P., Shea, P., and Gozani, T., "Thermal neutron analysis (TNA) explosive detection based on electronic neutron generators," *Nuclear Instruments and Methods in Physics Research B* 99 (1995) 739-742.

[19] Brown, Douglas R. and Gozani, Tsahi, "Thermal neutron analysis technology," *Proceedings of the SPIE*, v. 2936 pg. 85-94 (1997).

[20] Loveman, R., Bendahan, J., Gozani, T., and Stevenson, J., "Time of flight fast neutron radiography," *Nuclear Instruments and Methods in Physics Research B* 99 (1995) pg. 765-768.

[21] Womble, P. C., Schultz, F. J., Vourvopoulos, G., "Non-destructive characterization using pulsed fast-thermal neutrons," *Nuclear Instruments and Methods in Physics Research B* 99 (1995) pg. 757-760.

[22] Sawa, Zdzislaw P. and Gozani Tsahi, "PFNA Technique for the Detection of Explosives," *Proceedings of the First International Symposium on Explosive Detection Technology*. Atlantic City, NJ, November 1991, pg. 82.

[23] Vartsky, D., Engler, G., and Goldberg, M. B., "A method for detection of explosives based on nuclear resonance absorption of gamma rays in ^{14}N," *Nuclear Instruments and Methods in Physics Research A* v. 348 (1994) pg. 688-691.

[24] Sredniawski, Joseph J., Debiak, T. W., Kamikowski, E., Rathke J., Milton, B., Rogers, J., Schmor, P., Stanford, G., Brondo, J., "A Contraband Detection System Proof-Of-Principle Device Using Electrostatic Radiation," *Proceedings of the 18th International Linear Accelerators Conference*, 1996, pg. 444-446.

[25] Bertozzi, William, Poster: Material Identification and Object Imaging using Nuclear Resonance Fluorescence, Jul. 18, 2003, MIT, Dept. of Energy's Office of Nuclear Physics Workshop on the Role of the Nuclear Physics Research Community in Combating Terrorism.

[26] Yule, Thomas J., Micklich, Bradley J., Fink, Charles L., and Sagalovsky, Leonid, "Fast-neutron transmission spectroscopy for illicit substance detection," *Proceedings of the SPIE* v. 2867, pg. 239-242.

[27] Gongyin Chen, *Fast Neutron Resonance Radiography for Elemental Imaging: Theory and Applications*. Ph.D. Dissertation, Massachusetts Institute of Technology, 2001.

[28] Shi, Shuanghe, *An Accelerator-Based Neutron Imaging System and Its Application to Detection of Corrosion in Aircraft*. Ph.D. Dissertation, Massachusetts Institute of Technology, 1995.

[29] Guzek, Jacek, *Elemental Radiography Using Fast Neutron Beams*. Ph.D. Dissertation, University of the Witswatersrand, South Africa, 1999.

[30] Chen, Gongyin and Lanza, Richard C., "Fast Neutron Resonance Radiography: Theory and Applications," *IEEE Transactions on Nuclear Science*, Vol. 49, no. 4, August 2002.

[31] Cierjacks, S., ed. *Neutron Sources for Basic Physics and Applications* (Oxford, New York: Pergamon Press, 1983).

[32] Mario Conte and William W. Mackay, *Physics of Particle Accelerators*. (NJ: World Scientific Publishing Co., 1991).

[33] Hamm, Robert W., "The RFQ Linac: A High-Current Compact Ion Accelerator for Explosive Detection," *Proceedings of the First International Symposium on Explosive Detection Technology*. Atlantic City, NJ, November 1991, p. 175.

[34] Whittlestone, S., "Neutron distributions from the deuterium bombardment of a thick beryllium target," *J. Phys. D: Appl. Phys.*, Vol. 10, 1977.

[35] A description of kinematic relationships can be found in any standard physics or nuclear science textbook. For example, see Weston M. Stacey, *Nuclear Reactor Physics* (New York: John Wiley & Sons, Inc., 2001), Chapter 1.

[36] F. M. Bacon, R. J. Walko, D. F. Cowgill, and A. A. Riedel, "Intense neutron source development for use in cancer therapy," *IEEE Transactions on Nuclear Science*, 28(2):1902-1905, April 1981.

[37] F. M. Bacon and A. A. Riedel, "Intense neutron source target test facility: A 200 kV, 200 mA dc, deuterium ion accelerator," *IEEE Transactions on Nuclear Science*, 26(1):1505-1508, February 1979.

[38] Meadows, James W., Smith, Donald L., and Winkler, Gerhard, "A High-Current Deuterium Gas Target for Neutron Nuclear Data Research," *Nuclear Instruments and Methods* 176 (1980). pg. 439-442.

[39] Erik Iverson, *Windowless Gas Targets for Neutron Production*, PhD Thesis, Massachusetts Institute of Technology, 1997.

[40] Ady Hershcovitch, "A plasma window for transmission of particle beams and radiation from vacuum to atmosphere for various applications," *Physics of Plasmas*, vol. 5, no. 5, May 1998, pg. 2130.

[41] D. Salerno, B.T. Pinkoski, A. Hershcovitch, and E. Johnson, "Windowless targets for intense beams," *Nuclear Inst. and Methods in Physics Research A*, v. 469 (2001), pg. 13-20.

[42] See any nuclear physics reference text, such as Ronald Allen Knief, *Nuclear Engineering: Theory and Technology of Commercial Nuclear Power*, 2nd Ed. (New York: Taylor & Francis, 1992) for a discussion of neutron slowing down and scattering.

[43] Knoll, Glenn F., *Radiation Detection and Measurement*, 3rd Ed. (New York: John Wiley & Sons, Inc.,2000).

[44] T.K. Gaisser, T. Stanev, P.V. Sokolsky, and R.E. Streitmatter, "Cosmic Rays," in *Journal of Physics G: Nuclear and Particle Physics*, (CA: Regents of the University of California, 2006), pg 245.

[45] David Ingram, Devon Jacobs and Don Carter, Edwards Accelerator Laboratory, Ohio University, Machine report for SNEAP 2001, Lund, Sweden

[46] *BC-400, BC-404, BC-408, BC-412, BC-416: Premium Plastic Scintillators*, Bicron Data Sheet.

[47] *Uncovering Hidden Defects With Neutrons*, Science and Technology Review, Lawrence Livermore National Laboratory, UCRL-52000-01-05, May 25, 2001.

[48] Blackburn, Brandon W., *Characterization of a High-Current Tandem Accelerator and the Associated Development of a Water-Cooled Beryllium Target for the Production of Intense Neutron Beams*, S.M. Thesis, Massachusetts Institute of Technology, January 1997.

[49] David Peter Gierga, *Neutron Delivery for Boron Neutron Capture Synovectomy*, Ph.D. Thesis, Massachusetts Institute of Technology, 2001.

[50] Brandon Blackburn, *High-Power Target Development for Accelerator-Based Neutron Capture Therapy*, Ph.D. Thesis, Massachusetts Institute of Technology, 2002.

[51] Whitney Raas, Brandon Blackburn, Erin Boyd, James Hall, Gordon Kohse, Richard Lanza, Brian Rusnak, and John Watterson, "Design and Testing of a High-Pressure Gas Target for Neutron Resonance Radiography," *Proceedings of the 2005 IEEE Nuclear Science Symposium and Medical Imaging Conference*, Puerto Rico, 2005.

[52] Information on the freely available particle transport code is available at http://www.srim.org.

[53] J. Guzek, K. Richardson, C.B. Franklyn, A. Waites, W.R. McMurray, J.I.W. Watterson, U.A.S. Tapper, "Development of high-pressure deuterium gas targets for the generation of intense mono-energetic fast neutron beams," *Nuclear Instruments and Methods in Physics Research B*, v. 152 (1999) 515-526.

[54] Frank W. Schmidt, Robert E. Henderson, and Carl H. Wolgemuth, *Introduction to Thermal Sciences*, 2nd Ed. (New York: John Wiley & Sons, Inc., 1993), Chapter 6.

[55] Information on FLIR Systems™, Inc. infrared cameras can be found at http://www.flirthermography.com.

[56] Cross-section data found at http://wwwndc.tokai-sc.jaea.go.jp, accessed 15 July 2006.

[57] Tong Yu and John M. Boone, "Lens coupling efficiency: Derivation and Application Under Differing Geometrical Assumptions," *Medical Physics*, Vol. 24, No. 4, April 1997, pg. 564-570.

[58] Spectral response characteristics from Eastman Kodak Company, KAF-6303 Performance Characteristics Data Sheet, pg. 12.
Available at http://ccd.com/images/kaf-6303e.pdf, accessed 24 May 2006.

[59] Ben A. Arnold, "Physical Characteristics of Screen-Film Combinations," in *The Physics of Medical Imaging: Recording System Measurements and Techniques*, Arthur G. Haus, Ed. (New York: American Institute of Physics, Inc., 1979), pg. 39.

[60] Eljen Technology EJ-309 Data Sheet available online at http://www.eljentechnology.com/datasheets/EJ309%20data%20sheet.pdf, accessed 21 October 2006.

[61] Glenn F. Knoll, *Radiation Detection and Measurement*, 3rd Ed. (New York: John Wiley & Sons, Inc., 2000), pg. 231.

[62] Information on the Bates Accelerator Laboratory is available online at http://mitbates.lns.mit.edu

[63] LANSAR® Model DL-3 Deuteron Linac System S/N-001 System Operation and Maintenance Procedures (Vol. 1). Provided by AccSys Technology, Inc., November 2005.

[64] Eljen Technology EJ-200 Data Sheet available online at http://www.eljentechnology.com/datasheets/EJ200%20data%20sheet.pdf, accessed 21 October 2006.